Global Dynamic Fluid-Structure-Interaction Analysis for a Submerged Floating Tunnel

Weiyi Zhang

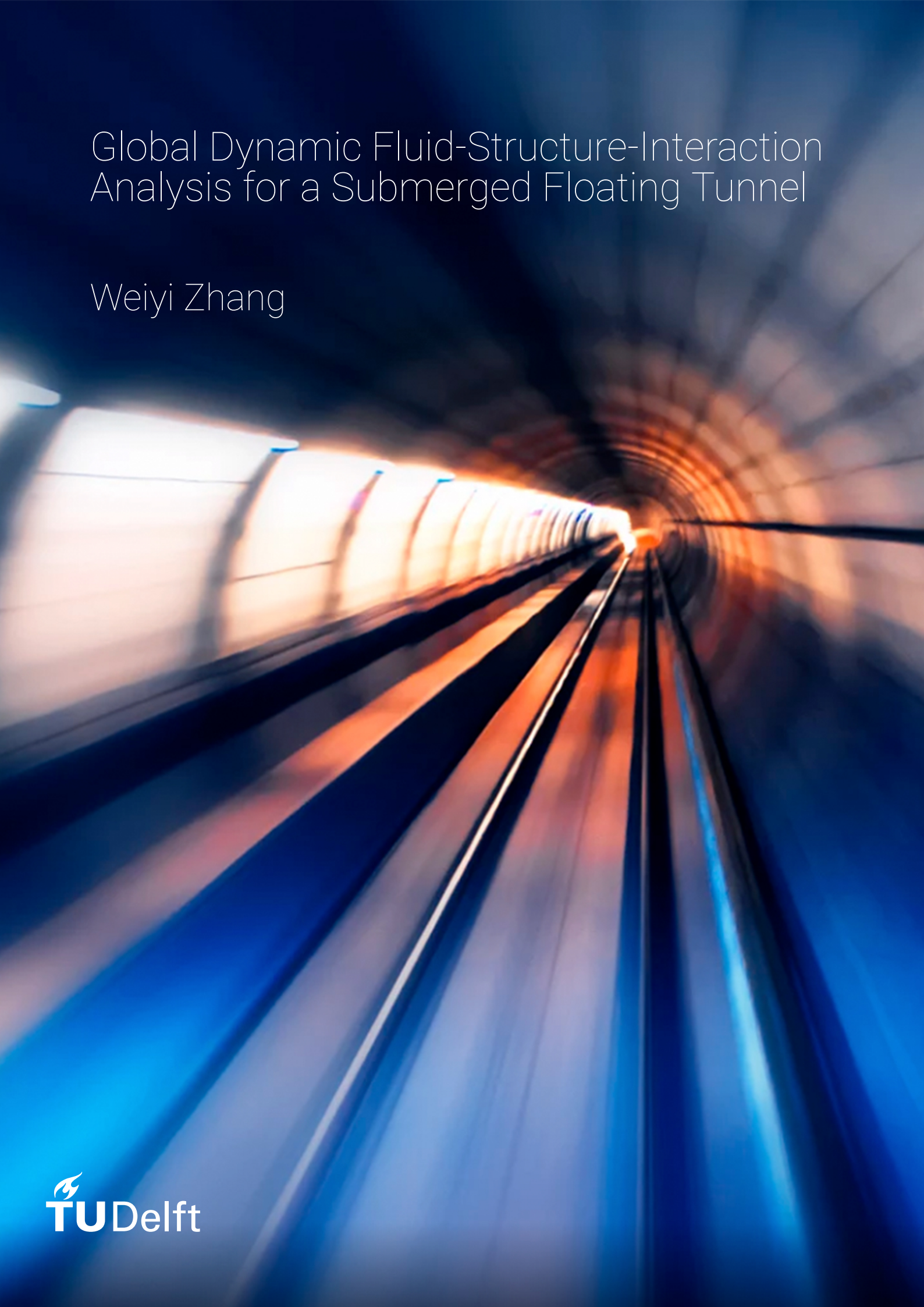

TU Delft

Global Dynamic Fluid-Structure-Interaction Analysis for a Submerged Floating Tunnel

by

Weiyi Zhang

to obtain the degree of Master of Science
in Civil Engineering - Structral Engineering
at the Delft University of Technology,

to be defended publicly on Monday September 30, 2019 at 9:30 AM.

Student number:	4717953	
Project duration:	December 2018 – September 2019	
Thesis committee:	Dr. ir. K.N. van Dalen (Chair)	Delft University of Technology
	Prof. dr. A.V. Metrikine	Delft University of Technology
	Dr. ir. D.J. Peters	Delft University of Technology
	Dr. ir. X. Chen	Royal HaskoningDHV

Cover photo by Evan Leeson.

An electronic version of this thesis is available at `http://repository.tudelft.nl/`.

Acknowledgements

This thesis is the final part of my master program in Structural Engineering at Delft University of Technology, which marks the end of two years of my life as a master student. These two years are full of memories of hard work, joyful moments, personal achievement and above all, the people who always on my side, accompanying me through the days of sunshine and also the nights of raining. I cannot imagine how I could go this far without their help.

First, I would like to express my gratitude towards my graduation committee. I would like to thank Karel van Dalen for chairing the committee. Your suggestion and guidance on how to solve my problems proved very inspiring. I can still remember how interesting it was attending your course on Dynamics and an Introduction to Continuum Mechanics at the first year of my master program. It is at that time, I decided to go for the Dynamics of Structures annotation to learn more about Structural Dynamics. Next, I want to thank Andrei Metrikine for your remarkable feedback through the meetings. They helped me find the right direction and saved a lot of time. Also, I would thank Dirk Jan Peters for sharing your expertise in both hydraulic and structural engineering. I enjoyed every meeting with you where you extended a broad view of practical and engineering thinking. Finally, I would like to give my thank to Xuexue Chen. Your detailed advice transferred big task into small pieces and make it much easier to complete. Each small coffee break discussing problem with you in the Rotterdam office inspired me a lot and really made my day.

Besides my committee members, I want to thank my colleagues at Royal HaskoningDHV, Ard Doorduyn and Marcel't Hart, who gives me engineering-oriented support. Furthermore, I would like to thank Yang Qu, a PhD at TUDelft, who supported me with the knowledge in vortex-induced vibration field.

I also want to thank my friends, my relatives especially my parents for their company and support during this two-year-journey, for the trips together around Europe and for the long distance video calls.

Last, I would like to thank my girlfriend, Shaoyun. I cherish each moment when I shared my new thoughts with you and when you calmed me down through my struggles. The dynamics with you is even more interesting and I will spend my whole life on it. Thank you for always being there for me!

Weiyi Zhang
Delft, September 2019

Abstract

This thesis aims to gain insight into the global dynamic fluid-structure interaction response of a submerged floating tunnel (SFT) under the wave and current loading to enhance the design. To this end, the tunnel tube is modelled as a Euler-Bernoulli beam deformed in three directions (horizontal displacement, vertical displacement, rotational angle), the discrete anchoring system as a continuous elastic foundation considering geometrical nonlinearity. Then, the Morison equation is used to model the combined current and wave loading and the oblique wave loading. A simplified wake oscillator and a non-simplified wake oscillator are used to model the vortex-induced vibration (VIV) under current loading. Subsequently, the modal superposition method and Runge-Kutta method are applied to obtain the response of the SFT in the time domain. The Fourier transform and the wavelet transform are applied to the time domain signal to perform a frequency domain analysis. Finally, a test on a scaled SFT model is used for a case study. A parametric study is carried out based on the results to study the influence of the geometrical and structural design parameters.

The results show that the motions in the horizontal direction and the rotational direction are significantly coupled together. Geometrical nonlinearity introduces the second-order effect to the system leading to a complicated vertical motion with a considerably larger displacement compared with the linear case. The amplitude of the VIV on the tunnel tube of the scaled model is very small based on the non-simplified wake oscillator. Moreover, it is found that, basically, increase of the BWR, increase of the stiffness in the cables, increase of the distribution of the net buoyancy in inclined cable, decrease of the tunnel length or decrease of the inclination of the inclined cables can reduce the maximum response of the SFT.

Based on the above findings, it is concluded that a global dynamic analysis is suggested when a SFT is expected to be subjected to oblique wave loadings. Geometrical nonlinearity is necessary to be considered for an accurate analysis especially for the response in the vertical direction. It is also necessary to be considered when the influence of the BWR is of interest. The VIV on the tunnel tube is negligible base on the scaled model.

Contents

List of Symbols

List of Latin Symbols

Symbol	Description	Unit
A	Cross-sectional area	[m^2]
BWR	Buoyancy weight ratio	[-]
C_a	Added mass coefficient	[-]
C_d	Drag coefficient	[-]
D	Diameter of the tunnel cross section	[m]
E	Young's modulus	[$N{\cdot}m^{-2}$]
E_c	Young's modulus of the concrete	[$N{\cdot}m^{-2}$]
E_i	Young's modulus of the inclined cables	[$N{\cdot}m^{-2}$]
E_v	Young's modulus of the vertical cables	[$N{\cdot}m^{-2}$]
EI_t	Bending stiffness of the SFT tube	[$N{\cdot}m^2$]
F_{ey}	External fluid force in horizontal direction	[N]
F_{ez}	External fluid force in vertical direction	[N]
Fn	Froude number	[-]
F_y	Restoring force in horizontal direction	[N]
F_z	Restoring force in vertical direction	[N]
F_φ	Restoring moment in rotational direction	[N·m]
F_{NB}	Net buoyancy force	[N]
F_{VD}	Vortex drag force	[N]
F_{VL}	Vortex lift force	[N]
F_{Vy}	In-line force	[N]
F_{Vz}	Cross-flow force	[N]
GI_p	Torsional stiffness of the SFT tube	[$N \cdot m \cdot rad^{-1}$]
H_w	Wave height	[m]
I_t	Second moment of area	[m^4]
I_p	Torsional constant	[m^4]
I	Polar moment of inertia	[m^4]
G	Shear modulus	[$N{\cdot}m^{-2}$]
L	Characteristic length to determine Froude number	[m]
St	Strouhal number	[-]
T	Kinetic energy	[$N \cdot m$]
T_i	Pretension force in the inclined cable	[N]
T_v	Pretension force in the vertical cable	[N]
T_w	Wave period	[s]
U	Flow velocity	[$m{\cdot}s^{-1}$]
V	Potential energy	[N·m]
V_c	Current speed	[$m{\cdot}s^{-1}$]
V_n	Reduced velocity	[$m{\cdot}s^{-1}$]
V_T	Surface current velocity due to tides	[$m{\cdot}s^{-1}$]
V_w	Surface current velocity due to wind	[$m{\cdot}s^{-1}$]
W_e	Work done by the external forces	[N·m]
$X(f)$	Frequency domain representation in Fourier transform	[-]
$X(\tau, f)$	Two-dimensional representation in short-time Fourier transform	[-]
$X(a, b)$	Two-dimensional representation in wavelet transform	[-]
a	Wave amplitude	[m]
c_y	Structural damping coefficient in horizontal motion	[$N \cdot s \cdot m^{-1}$]

Symbol	Description	Unit
c_z	Structural damping coefficient in vertical motion	$[\mathrm{N}\cdot\mathrm{s}\cdot\mathrm{m}^{-1}]$
c_φ	Structural damping coefficient in rotational motion	$[\mathrm{N}\cdot\mathrm{s}\cdot\mathrm{m}^{-1}]$
d	Water depth	[m]
d_i	Diameter of the inclined cables	[m]
d_t	Diameter of the tunnel cross section	[m]
d_v	Diameter of the vertical cables	[m]
f_s	Vortex shedding frequency	[Hz]
g	Gravitational acceleration	$[\mathrm{m}\cdot\mathrm{s}^{-2}]$
h_w	Water Depth of the basin	[m]
j	The imaginary unit	[-]
k	Wave number	$[\mathrm{m}^{-1}]$
k_i	Stiffness of the inclined cable	$[\mathrm{N}\cdot\mathrm{m}^{-1}]$
k_v	Stiffness of the vertical cable	$[\mathrm{N}\cdot\mathrm{m}^{-1}]$
l_b	Length of the basin	[m]
l_i	Length of the inclined cables	[m]
l_t	Length of the tunnel	[m]
l_v	Length of the vertical cables	[m]
m	The cylinder mass	[kg]
m_a	The added mass	[kg]
m_t	Mass of the tunnel per unit length	$[\mathrm{kg}\cdot\mathrm{m}^{-1}]$
q	The wake parameter	[-]
r_g	Radius of gyration of the tunnel cross section	[m]
s_i	Spacing of the inclined cables	[m]
s_v	Spacing of the vertical cables	[m]
u_w	Wave phase velocity	$[\mathrm{m}\cdot\mathrm{s}^{-1}]$
$\mathbf{u}$	Flow velocity	$[\mathrm{m}\cdot\mathrm{s}^{-1}]$
$\dot{\mathbf{u}}$	Flow acceleration	$[\mathrm{m}\cdot\mathrm{s}^{-2}]$
$\mathbf{v}$	Structure velocity	$[\mathrm{m}\cdot\mathrm{s}^{-1}]$
$\dot{\mathbf{v}}$	Structure acceleration	$[\mathrm{m}\cdot\mathrm{s}^{-2}]$
$x(t)$	Time domain signal	[-]
w_b	Width of the basin	[m]
$w(\tau)$	The window function	[-]
z	Height above the seabed	[m]

List of Greek Symbols

Symbol	Description	Unit
$\Psi(t)$	The mother wavelet	[-]
α_i	Angle of inclination	[degree]
α_w	Attack angle	[degree]
ε	A Nondimensional Tuning Parameter	[-]
ρ	Density of the water	$[\mathrm{kg}\cdot\mathrm{m}^{-3}]$
ρ_i	Density of the inclined cables	$[\mathrm{kg}\cdot\mathrm{m}^{-3}]$
ρ_t	Equivalent density of the tunnel	$[\mathrm{kg}\cdot\mathrm{m}^{-3}]$
ρ_v	Density of the vertical cables	$[\mathrm{kg}\cdot\mathrm{m}^{-3}]$
ω	Wave frequency	$[\mathrm{rad}\cdot s^{-1}]$
ω_s	The vortex shedding frequency	$[\mathrm{rad}\cdot\mathrm{s}^{-1}]$

List of abbreviations

Symbol	Description
BOEF	Beam on Elastic Foundation Model
BWR	Buoyancy Weight Ratio
DOF	Degree of freedom
FE	Finite Element
FSI	Fluid-Structure Interaction
LHS	Left Hand Side of the Equation
ODE	Ordinary Differential Equation
PDE	Partial Differential Equation
RHS	Right Hand Side of the Equation
SFT	Submerged floating tunnel
SFTB	Submerged floating tube bridge
VIV	Vortex-induced vibration

List of Figures

List of Tables

1 Introduction

How to cross a water area to reach the other shore is a never-ending pursuit of all human beings. Nowadays, this topic is still of vital importance especially in Civil Engineering, as it is proved by the numerous large infrastructures which have been built in the last few decades all over the world. For instance, the Akashi Kaikyō Bridge designed to connect Kobe and Honshu in the Akashi Strait (Japan, completed in 1998), the Channel Tunnel linking Folkestone, Kent, in England, with Coquelles, Pas-de-Calais, near Calais in northern France, beneath the English Channel at the Strait of Dover (Europe, completed in 1994) and the Hong Kong–Zhuhai–Macao Bridge (HZMB) connecting Hong Kong, Macau, and Zhuhai—three major cities on the Pearl River Delta (China, completed in 2018). These cases probably represent the most advanced examples of the structural solutions to link areas divided by the presence of waterways: Cable Supported Bridges (i.e. Suspension or Cable stayed Bridges), Underground Tunnels and Immersed Tunnels (Figure 1.1).

Although these solutions are traditionally and widely used, the complexity of their design issues increases as the distance and the depth of the water area to be covered grows up. Therefore, the crossing of long span and deep water area can be very difficult and sometimes impossible. Moreover, the traditional methods feature some disadvantages which are unreasonable and inefficient in some cases. For instance, Cable Supported Bridges starts becoming cost-prohibitive due to the design requirement of higher towers as the span extends; Underground Tunnels and Immersed Tunnels demand steeper access ramps as the water depth increases, which implies a noticeably larger energy consumption and travel time.

A revolutionary technical solution, which can get over the above mentioned disadvantages, is the Submerged Floating Tunnel (SFT), which is based on the idea of exploiting the load carrying capacity of water, due to the Archimedes buoyancy (Faggiano et al., 2005). In fact, SFT is conceived as a tubular structure to be placed at a prefixed depth in the water (Figure 1.1), anchored by a support system such as pontoons on the surface or by anchoring to the water bed, preventing it from floating to the surface or submerging, respectively. The tether systems play the role of constraining the tunnel, minimizing its displacements and stresses induced by the environmental loading, such as the hydrodynamic loading, seismic loading, etc.

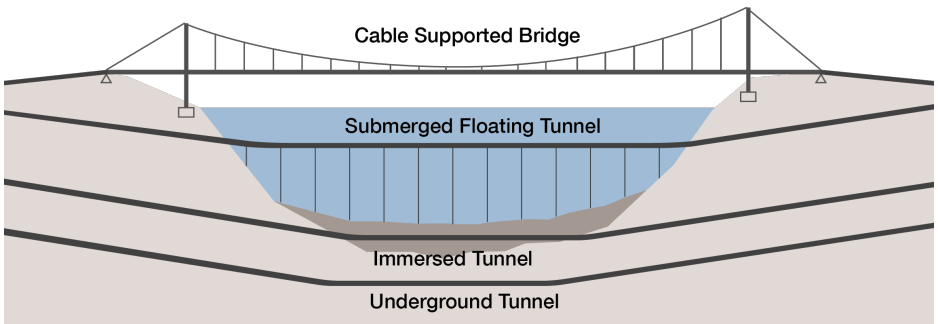

Figure 1.1: Waterway crossing methods

1.1. Problem statement

Submerged Floating Tunnels (SFT) can provide a more economical means of crossing a body of water than Cable Supported Bridges, Underground Tunnels and Immersed Tunnels, depending on the local sea and hydrographic conditions. However, no country has yet constructed a structure of this type, given that this concept has been in existence for a quarter of a century. Nowadays, Studies of SFTs are still being aggressively promoted in many countries, covering not only the aspects of design and construction but also the aspects of technical issues, psychological issues, and risk analysis. One of the most significant studies is the one on dynamics behaviour of SFT.

Research on the dynamic behaviour of SFT is generally performed in 2D with Finite Element (FE) software, such as ABAQUS, ANSYS or DIANA FEA, focusing mainly on one single detailed condition, such as Buoyancy-weight-ratio (BWR), hydrodynamics and anchoring systems. However, to the knowledge of the author, no references are available about the global (3D) dynamic behaviour of the SFT considering geometrical non-linear anchoring system. Furthermore, a FE model is usually not parametric. Many FE models with different geometries would be required to perform a parameter study. Therefore, it is desired to carry out a research into the 3D dynamic behaviour of a SFT considering longitudinal behaviour and geometrical nonlinearity, as well as provide a parametric model to investigate the influence of different parameters on the dynamic response of a SFT.

1.2. Research objective

The main goal of this research is to gain insight into the global dynamic fluid-structure interaction response of a submerged floating tunnel under the wave and current loading to enhance the design of a SFT. To this end, this research will provide several models to analyze the dynamic response of a scaled model of a submerged floating tunnel for various loading conditions. Furthermore, a parametric study will be performed to identify the possibility to keep the response within certain limits.

1.3. Research question

Two main research questions are formulated to meet the research objective:

1. *What is the global dynamic fluid-structure interaction response of a SFT under wave and current loading?*

2. *Which parameters can be used to reduce the dynamic response of a SFT?*

To be able to answer the main research questions, several sub-questions are formulated:

1. *How can the global dynamic fluid-structure interaction response of a SFT with discrete anchoring systems be modeled?*

2. *How does the stiffness of the anchoring system considering geometrical nonlinearity influence the results?*

3. *How does the global dynamic analysis influence the results?*

4. *How do the geometrical and structural design parameters influence the dynamic response of a SFT?*

1.4. Scope and Approach

The developed model will only describe a simplified schematization of the Submerged Floating Tunnel. The tunnel is considered as a Euler-Bernoulli beam. The discrete anchoring system is modelled as an equivalent continuous distributed spring include or exclude geometrical nonlinearity. In addition, several assumptions will be made concerning the physics of the loads to be able to use the superposition principle and potential flow theory. A modal domain approach will be used to obtain the dynamic response of a SFT. A frequency analysis of the obtained results will be carried out to comprehend the physical properties of the dynamic response. A case study with respect to a scaled physical model test will be performed and the results will be used for further validation.

1.5. Outline

The first part of the report presents a literature review where submerged floating tunnels are introduced and all required theory for model development is explained. The literature review is divided into three chapters. First, chapter 2 describes the developments regarding submerged floating tunnels to put this research into perspective. Chapter 3 explains the most important concepts of structural dynamics in terms of modal analysis and frequency domain analysis. Finally, chapter 4 introduces the hydrodynamics related to a SFT.

In the second part, the model development is addressed. First, the methods to derive a linear stiffness model and a nonlinear stiffness model for the anchoring system are developed in chapter 5. Subsequently, four different models are derived to perform global dynamic analysis regarding different assumptions and loading conditions in chapter 6.

The third part describes an application of the model. First, a test about a scaled physical model of SFT is introduced in chapter 7. Then, in chapter 8 the results of the dynamic response of this scaled model is presented and discussed using physical principles. Finally, a parametric study based on the results in chapter 8 is described in chapter 9.

Finally, the conclusion and recommendations are presented in part 4. The outline of this report is illustrated in Figure 1.2.

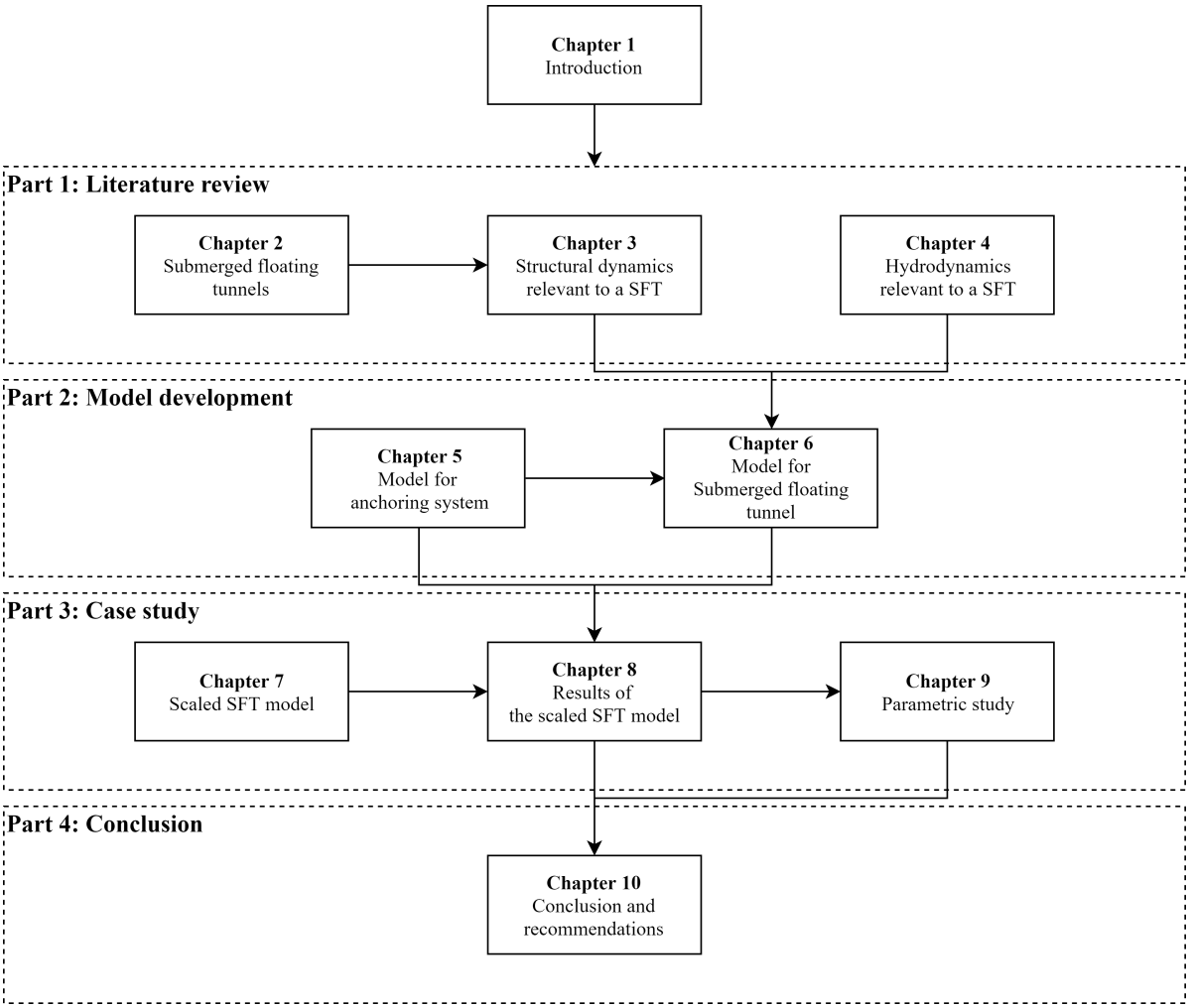

Figure 1.2: Outline of the report

I

Literature review

2

Submerged floating tunnels

This chapter describes the state-of-the-art developments regarding submerged floating tunnels to put this research into perspective. First, the concept of submerged floating tunnels is introduced in section 2.1. Subsequently, some structural features and loading conditions relevant to this research are addressed in the following sections.

2.1. Concept of submerged floating tunnels

A submerged floating tunnel (SFT), also known as submerged floating tube bridge (SFTB), suspended tunnel, or Archimedes bridge, essentially contains a tubular structure floating underwater. A certain range of water clearance is assured in order to avoid the impact of traffic and weather on the water surface and the consideration of the water pressure. The tunnel is fixed in a position through anchorage systems comprised of cables, rods or piles, either anchored to the seabed or pontoons at the surface, preventing it from floating or submerging, respectively. (Figure 2.1)

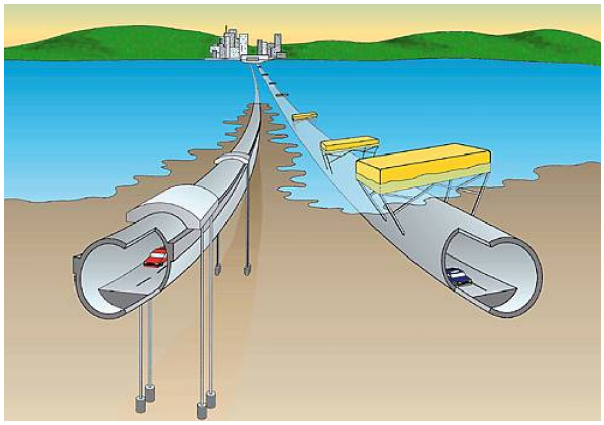

Figure 2.1: The SFT waterway crossing solution (Martire, 2010)

The concept of SFT was born in the early decades of 1900 in Norway, which is based on technology applied to floating bridges and offshore structures. Therefore, only the great improvements achieved in floating bridges and offshore technologies in the last thirty years allowed to solve the numerous problems that hampered the realization of this kind of structure, so that several preliminary designs and feasibility studies have been proposed in the last few years. Furthermore, since the construction of SFT is mostly similar to which of Immersed Tunnels, the large experience gained in the field of Immersed Tunnels can be capitalised for the development of SFT. These two waterway crossing methods are both modular structures. However, the dynamic behaviour of SFT is certainly more complex than the one of the Immersed Tunnel.

With respect to traditional strait crossing solutions, the SFT undoubtedly features several advantages under the structural, economic and environmental impact point of view. However, the actual construction of

a Submerged Floating Tunnel still appears nowadays as a real challenge, since it deals with a completely innovative structural solution and no SFT has been erected up to today. Consequently, no experimental data on its actual behaviour is available, which could fill the gap between the theoretical studies on SFT and its construction.

Based on the above considerations, it is apparent that the first necessary step for the actual development of Submerged Floating Tunnels, as a widespread technical solution for waterway crossings, is represented by the design and construction of a SFT prototype. A SFT prototype is very useful for collecting the experimental data needed to support the numerical and theoretical studies, and for the complete comprehension of the actual behaviour of this kind of structures. This important initial step is going to be undertaken in the near future since a Sino-Dutch joint group (CCCC SFT Technical Joint Research Team) has carried out the first 3D physical test of a SFT prototype in the World to be fabricated and erected in the Tianjin (People's Republic of China) in 2019.

2.2. Structural features of the tunnel

2.2.1. Materials

The materials to be used for a Submerged Floating Tunnel are selected according to the structural and functional performances such as the resistance to the environment condition, fabrication, assembly and maintenance issues, time needed for the supply, material and constructional cost, etc (FEHRL (Forum of European National Highway Research Laboratories), 1996). The structural solution can be optimized, considering the structural effectiveness, the constructability and the economical point of views. One of the most suitable solutions is a composite structure involving several materials with their defects neutralized and with their benefits exalted (Faggiano et al., 2005). The materials that could be used in the construction of the tunnel modules of a SFT are:

- Steel;
- Reinforced Concrete;
- Aluminum alloys;
- Rubber foam.

Ordinary steel types are very suitable for SFT applications, which features several qualities such as good mechanical properties, good resistance to fatigue and abrasion, good workability and weldability and a large strength-to-weight ratio. These features make it a very suitable material for offshore and SFT constructions. However, there are also some drawbacks of ordinary steel, like the low resistance to corrosion, the low performance of the welded connections with respect to fatigue due to the cyclic loads imposed by environmental loading conditions. In order to improve its performances in maritime applications, new types of steel have been introduced. One of the new steel types is named as Fatigue Crack Arrester (FCA), which guarantees a better resistance to the propagation of fatigue cracks, assuring also a strength slightly larger and a weldability equivalent to those of ordinary steel (Konda et al., 2003). Other new steel types, characterized by high strength and resilience, have been lately developed and produced in large scale for the purpose of wide applications in the offshore field (Nagai et al., 2003).

Concrete is also widely used in maritime applications. Besides the contribution to the structural strength and stiffness, concrete can also provide the weight needed to counteract the tunnel buoyancy in order to stabilize the structure. Other advantages offered by concrete are: good resistance to the corrosion in marine environment, to abrasion and to fire and high temperatures, low cost and possibility to be cast to realize complex shapes. Its main disadvantage is its considerably small resistance to tensile stresses, which can be improved by applying pre-compression to the concrete offshore structures.

Another class of materials used in offshore engineering is aluminium alloys, which offer a wide range of strength with a relatively low weight. It also has a high resistance to marine corrosion so that there is no need for protective coatings. However, aluminium alloys features poor resistance to fire. They are mainly applied in the emerged part of the offshore structures.

Finally, the last material worth to be mentioned is the rubber foam, which is originally used in the Naval Engineering to increase the buoyancy of vessels. Grantz (2003) has considered applying this material in SFTs to construct an external layer to protect the internal structure from corrosion and to increase the tunnel buoyancy.

2.2.2. Design requirement

Some design requirements must be checked to determine the structural and geometrical parameters of the cross-section of the SFT:

1. The internal diameter of the cross-section should be large enough to accommodate the transport infrastructures, lateral maintenance facilities and ventilation systems for the fire safety.

2. The main structural performances (stiffness, strength and ductility) must be guaranteed in both serviceability and ultimate limit states by selecting the suitable dimension of the tunnel cross-section. Additionally, waterproofing reliability of the tunnel needs to be designed carefully by setting up a waterproofing layer.

3. The buoyancy weight ratio (BWR), which is the ratio between upwards buoyancy force and the sum of the selfweight and live loads, needs to be designed larger than a minimum value, which guarantees that no slacking of the cables can be induced by the environmental loading conditions. Moreover, it must be taken into account that the external diameter of the cross-section defining both downwards and upwards forces, also influence the hydrodynamic actions, since the hydrodynamic forces are proportional to the diameter.

4. All the issues related to the fabrication and erection of the tunnel modules have to be considered in the design.

The third design requirement regarding the BWR is of particular importance and deserves a more detailed discussion. The BWR determined the required minimum pretension of the anchoring cables and at the same time it minimizes the permanent stress acting in the tunnel, anchoring system and foundations. Numerical studies confirmed that larger values of the BWR can improve significantly the structural performance of the SFTs when they are subjected to severe environmental loading scenarios. Brancaleoni et al. (1989) found that increasing the buoyancy ratio from 1.25 to 1.40 can lead to impressive improvements of the SFT response to extremely severe sea conditions.

2.2.3. Structural configurations

The structural configurations can be categorised according to their geometrical shape, mainly referring to the external shape of the SFT cross-section. The geometrical properties of the tunnel cross-section make a huge difference to the Fluid-Structure Interaction (FSI). The geometrical configuration of the SFT cross-section can be listed as the following types:

- Circular, as shown in Figure 2.2 (a);
- Polygonal, elongated in the horizontal direction, as shown in Figure 2.2 (b);
- Rectangular, with external keels providing a hydrodynamic shape, as shown in Figure 2.2 (c);
- Circular tubes connected by a frame substructure, as shown in Figure 2.2 (d).

A circular cross-section features a very rational structural behaviour with respect to the hydrostatic pressure (Brancaleoni et al., 1989; Grantz, 1997), since only compressive stresses and no bending are induced in the cross-section plane. Given that generally the outer ring shell of a circular SFT is made up of concrete, no bending means no longitudinal cracks, which results in a better performance on tunnel waterproofing. It may also be worth noting that thanks to the polar symmetry of a circular cross-section, the rotational force components can be negligible (Brancaleoni et al., 1989). However, such shape needs more complicated construction procedures than a rectangular cross-section (Grantz, 1997).

A polygonal cross-section, elongated in the horizontal direction, are suitable when large water motion due to currents and waves is expected in the horizontal direction. This shape might be complicated to fabricate. This drawback can be improved by adopting a rectangular cross-section.

Rectangular cross-section gives the most rational solution, as the construction procedures and the arrangement of the internal spaces are clear and simple. However, the water flow passing through a rectangular cross-section may induce turbulence, which increases the dynamic pressures on the structure. A set of lateral streamlined keel would solve this problem and improve the dynamic behaviour of the tunnel.

Finally, two or more circular tubes connected by a frame substructure would be another option. This shape is a combination of the circular cross-section and the polygonal cross-section. Therefore, both properties of circular cross-section and the polygonal cross-section can be expected in this shape.

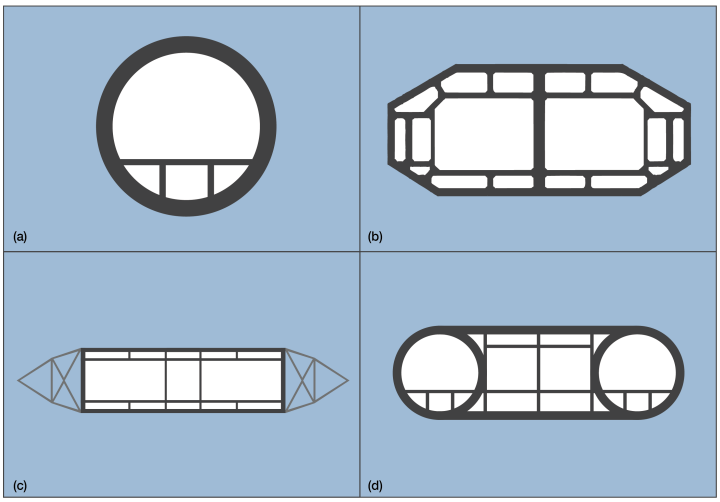

Figure 2.2: The cross-section shape: (a) Circular; (b) Polygonal; (c) Rectangular; (d) Circular tubes connected by a frame substructure.

2.3. Structural features of the anchoring system

2.3.1. Materials

The materials applied for the anchoring system of a SFT are chosen according to the main stress state of the anchoring member. The materials that could be used in the construction of the anchoring system of a SFT are:

- Steel;
- Synthetic fiber;
- Concrete.

The use of steel anchorages is common practice in Offshore Engineering. It can be used to realize both rigid members such as tension legs or tubular tethers, or flexible members such as mooring cables or taut wires.

Synthetic fiber ropes are made of innovative material which is developed in the last few years. This material features the properties of excellent strength-to-weight-ratio and higher stiffness compared to steel. In the nineties the American Petroleum Institute (API, 2002), the American Bureau of Shipping (ABS, 1999) and several private companies published guidelines providing indications regarding the mechanical properties of synthetic fibers and their performance as mooring lines for offshore production members. The material is physically nonlinear as their axial stiffness varies with time. Moreover, it is observed that their stiffness seems to be generally larger when subjected to dynamic loads (Flory et al., 2004). For the aforementioned reasons, it seems inappropriate to model their behaviour as elastic and it is recommended to consider different values for their axial stiffness, in particular with regard to its variation with the frequency of the applied dynamic loads (Barltrop, 1998).

Concrete is another suitable material when the residual buoyancy is negative. In this case, the anchoring system is made up of piers or columns where concrete features a compressive capacity.

2.3.2. Anchoring system configurations

The anchoring system of a Submerged Floating Tunnel are assembled to bear its permanent upwards residual buoyancy or downwards residual weight and to limit displacements and stresses of the tunnel within acceptable limits under environmental loading.

There are four typologies of the anchoring system:

- **Self-bearing:** In case both of residual buoyancy and residual weight are zero, the environmental conditions are favourable and the length of the crossing is relatively small, the designer may refer to a self-bearing crossing as shown in Figure 2.3 (a).
- **Piers:** This typology as shown in Figure 2.3 (b) is suitable for bearing both residual buoyancy and residual weight.
- **Tensioned members:** To bear the upwards residual buoyancy, the anchoring system is made of tension members, which can be cable or tethers as shown in Figure 2.3 (c).
- **Buoys:** To bear the downwards residual weight, the anchoring system is made of floating pontoons as shown in Figure 2.3 (d).

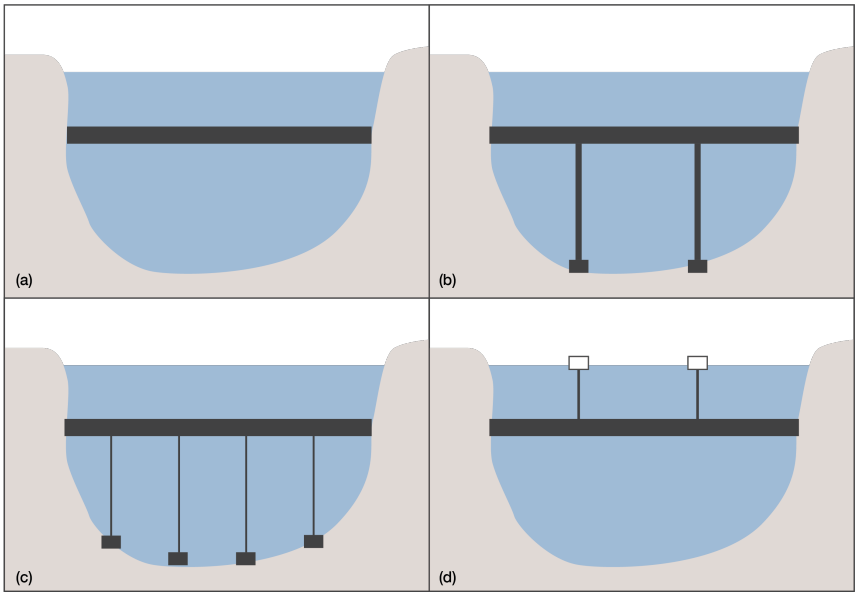

Figure 2.3: Anchoring system typologies: (a) Self-bearing; (b) Piers; (c) Tensioned memebers; (d) buoys. (FEHRL (Forum of European National Highway Research Laboratories), 1996)

The tunnel configuration with tension members is considered to be the most suitable solution choice in possible high horizontal loading conditions. The main advantage of this configuration is possibility to arrange the anchoring cables not only in the vertical direction but also be in the inclined direction with respect to the vertical axis in order to provide the required horizontal stiffness.

When using tension members as a configuration, the geometrical properties of the cables, such as the diameter of the cross-section of the cable and the inclination angles, are of vital importance to determine the stiffness of the system. Generally, the adopted configuration is repeated at a prescribed spacing in the axial direction to provide a uniform stiffness. However, in the cross-sectional plane, many choices are applied for the arrangement of the cables. Some of these are shown in Figure 2.4.

Physical predictions suggest that anchoring system made up of two vertical cables (as shown in Figure 2.4 (a)) configuration is effective only in the vertical direction, as it provides no support against lateral loads, thus being suitable only in a calm environment.

Arrangement with only two inclined cables (as shown in Figure 2.4 (b)) have been proposed too, but numerical analyses showed that this arrangement leads to high level of stresses in the cables and induces considerable rotational angle in the tunnel when it is subjected to horizontal actions.

The anchoring system made up of two vertical cables and two inclined cables (as shown in Figure 2.4 (c)), and the anchoring system made up of four inclined cables (as shown in Figure 2.4 (d)) are the most effective ones, as they support the tunnel vertically, horizontally and rotationally. It is confirmed by the experimental studies (Maeda et al., 1994), as they showed that four inclined cables per group guarantee the best SFT performances, especially in terms of horizontal displacement.

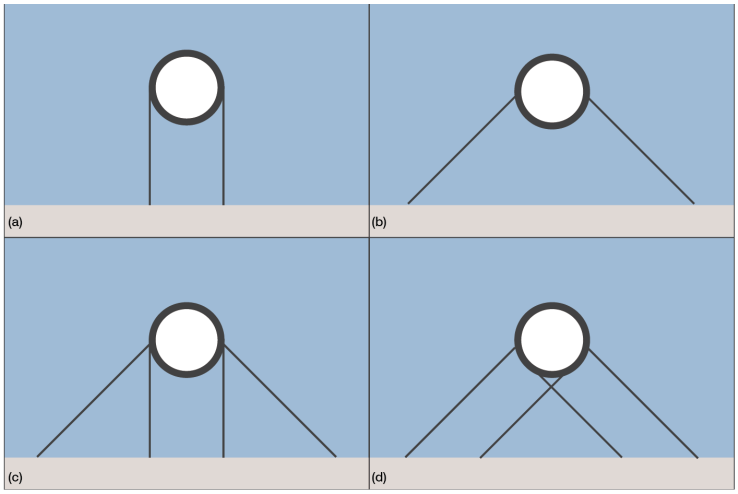

Figure 2.4: Arrangement of the cables in the cross-sectional plane:
(a) Two vertical cables; (b) Two inclined cables; (c) Two vertical cables and two inclined cables; (d) Four inclined cables.

It is worth to briefly discuss a phenomenon regarding second order effects. Normally, configuration of two vertical cables provided no support against lateral loads when the second order effect is excluded. When the second order effect is considered, a horizontal restoring force due to lateral displacements would arise in the anchoring system and is linearly proportional to the this lateral displacement. This phenomenon is often referred as the pendulum effect.

Another phenomenon worth to be mentioned is the so-called snapshot phenomenon, which is the result of the slackening of the cables due to environmental loadings. It refers to the action that the tensile force in the cables goes to zero and then instantaneously reaches a very large value (Kunisu et al., 1994). This phenomenon needs to be treated carefully as it may leads to failure of the cables.

2.4. Loading conditions

2.4.1. Permanent loads

The permanent loads acting on a SFT contains four components: the structural weight, the non-structural weight, the water buoyancy and the hydrostatic pressure. The algebraic sum of the structural and non-structural weight defines the residual buoyancy of the tunnel, which is a fundamental factor for the stability of the structure. The hydrostatic pressure has to be paid more attention, when a SFT is build in large water depths.

2.4.2. Functional loads

The function loads are related to the transportation within the SFT, which are passage of the vehicles and/or the pedestrians. Eurocode, EN 1991-3, often use statistical data to define the most unfavourable loading condition on the structure.

2.4.3. Environmental loads

For a SFT, the environmental loads are mainly related to the marine environment actions, such as the change in the tide levels, waves and currents, earthquakes and tsunamis. This research focuses on the loading of waves and currents. The literature review regarding these two loading conditions is presented as follows.

Waves

Water waves are characterized by an oscillating motion of the water particles and can be of two types:

- **Wind generated waves:** surface waves occurring on the free surface of waterways, due to the wind blowing over a vast enough stretch of fluid surface.
- **Internal waves:** water particles are kept in motion by the force of gravity acting on small differences in density. A density difference can exist between two fluids or between different parts of the same fluid because of a difference in temperature, salinity, or concentration of suspended sediment.

Although internal waves can be important and induce significant loads on marine structures, in most of the cases wave water motion is made of wind generated waves(Martire, 2010).

Several theories have been developed to describe the motion of water particles due to waves,can be distinguished the linear, nonlinear and other wave theories. They are generally based on the determination of the velocity potential satisfying the Laplace Equation with the assumption of an irrotational and incompressible fluid. A detailed overview of the wave theories available in literature is given in Sarpkaya and Isaacson (1981). The accuracy of the wave theories is in dependence of the wave parameters. In fact each wave theory are reliable in different fields of application as shown in Figure 2.5.

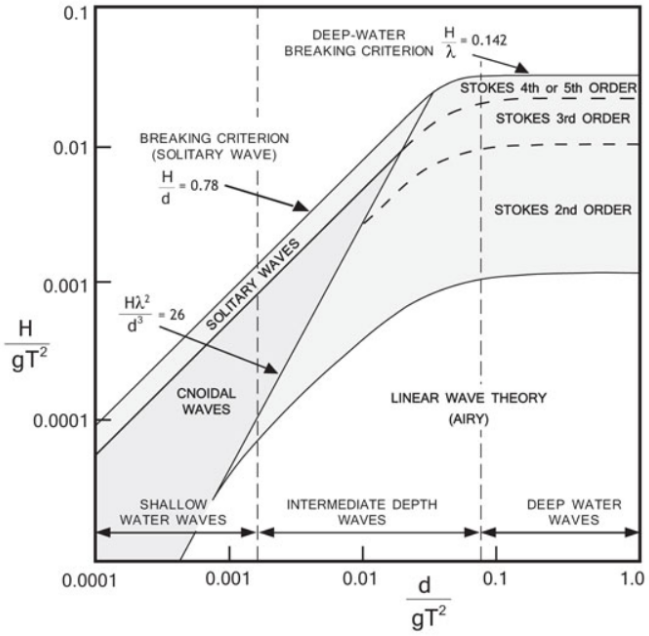

Figure 2.5: Applicability ranges of various waves, taken from Modeling Waves in FLOW-3D
H: wave height; T: wave period; g: gravitational acceleration

The simplest wave theory is the Airy linear (also called Sinusoidal) wave theory, which is based on the fundamental assumption that the wave height H_w is small, thus allowing to impose the free surface boundary condition at the still water surface height and to neglect higher order terms in the governing equations. Clearly, this wave theory can be assumed to be valid as a first approximation only when the wave height H_w is considerably smaller than both the wave length L_w and the seabed depth d.

The nonlinear wave theories with higher order are proposed to represent the complete solution of the governing equations of the water motion more precisely. The most common nonlinear wave theory is the Stokes wave theory, which introducing a perturbation procedure with successive approximations. This theory is considered to be valid when the wave height-to-length ratio is largely lower than one ($H_w/L_w \ll 1$) and when the wave length L_w is less than 8 times the water depth d (Peregrine, 1972; Laitone, 1962).

The low order Stokes wave theories are not suitable in shallow waters as many coefficients of the higher order terms become too large with respect to the lowest order terms. A more reliable nonlinear procedure to describe the wave properties is the so-called Cnoidal Wave Theory, which expresses the wave characteristics in terms of the Jacobian elliptic function. Clearly, this theory is used to describe surface gravity waves of fairly long wavelength, as compared to the water depth. A limiting case of Cnoidal wave is the Solitary wave, characterized by an infinite wave length.

Currents

Currents in waterways are usually classified into two types:

- **Wind generated currents:** generated by the wind blowing over the water surface;
- **Tides generated currents:** generated by the rise and fall of the water level due to tides.

Usually, current is modelled as a horizontal velocity distribution along the water depth. This distribution can be roughly assumed to be constant or, more generally, can be represented by as a polyline.

For some engineering structures in offshore oil engineering, the current velocity V_c can be calculated as the following (Fang and Duan, 2014):

$$V_c(z) = V_T \cdot \left(\frac{z}{d}\right)^{1/7} + V_w \cdot \left(\frac{z}{d}\right), \tag{2.1}$$

where:

d	=	Water depth	[m],
z	=	Height above the seabed	[m],
V_T	=	Surface current velocity due to tides	[m·s^{-1}],
V_w	=	Surface current velocity due to wind	[m·s^{-1}].

Thus the contribution due to wind generated currents is generally predominant.

2.4.4. Vortex shedding

Vortex shedding is an oscillating flow which takes place when a steady current passes a cylindrical body, due to the viscosity of the fluid. Generally, the vortex shedding is asymmetric, i.e. vortices are generated alternately on both sides of the downstream portion of the cylinder, giving rise to the dynamic pressure field exerted on the cylinder which varies with. The resultant of these time varying pressures is an oscillating force, which has a main component in the direction transversal to the flow propagation, named lift force, and a minor one in the direction of the flow, which is added to the steady value of the drag force and features a frequency being twice the one of the vortex shedding.

In 1878, Strouhal found a relationship between the frequency of the vortex shedding and the velocity of the incoming flow. In particular, he defined the following relationship:

$$St = \frac{f_s D}{U}, \tag{2.2}$$

where:

St	=	Strouhal number	[-],
f_s	=	Vortex shedding frequency	[Hz],
D	=	Diameter of the tunnel cross-section	[m],
U	=	Flow velocity	[m·s^{-1}].

The Strouhal number is found to be nearly constant, equal to 0.2 for smooth circular cylinders and to 0.25 for rough circular cylinders, in the Re range from 10^3 to 5×10^5, and for Re belonging to the post-supercritical flow regime is nearly constant and equal to 0.5 for smooth circular cylinders (Figure 2.6). For very large values of Re ($\geq 10^8$), which are generally of interest for SFT cases, only experimental data in wind tunnel test are available.

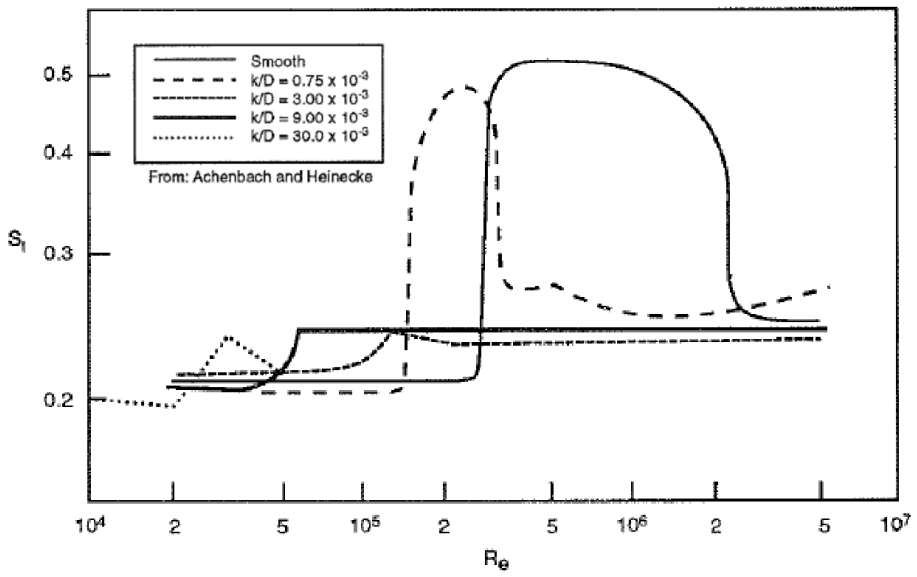

Figure 2.6: Variation of Strouhal number St with Reynolds number and surface roughness (Achenbach and Heinecke, 1981)

When the flow velocity is increased or decreased in such a manner that the vortex shedding frequency (f_s) approaches the natural frequency (f_n) of an elastic structure, so that

$$f_n \simeq f_s = \frac{StU}{D} \quad \text{or} \quad V_n = \frac{U}{f_n D} \simeq \frac{U}{f_s D} = \frac{1}{St} \simeq 5, \tag{2.3}$$

where:

V_n = Reduced velocity [m·s^{-1}],

the vortex shedding frequency suddenly locks onto the natural frequency (Blevins, 1977). The Strouhal law in Equation 2.2 is no longer valid. This effect is called lock-in or synchronization. The locked in resonant oscillations of the near wake input substantial energy to the structure and large-amplitude vibrations can result.

2.5. Conclusion

The following conclusion are drawn based upon this literature review:

- BWR is of particular importance in the design of the tunnel and deserves a detailed study.
- A circular cross-section of the structure features better performance in most cases.
- Anchoring system made up of four inclined cables are the most effective ones, as they support the tunnel vertically, horizontally and rotationally.
- The pendulum phenomenon and the snapshot phenomenon needs to be checked twice when design the anchoring system.
- The Airy Linear Wave Theory is valid only when the wave height H_w is considerably smaller than both the wave length L_w and the seabed depth d.
- The lock-on phenomenon occurs when the reduced velocity V_n is larger than 5.

3

Structural dynamics relevant to a SFT

The dynamic response of a structure such as a submerged floating tunnel is mainly covered in the field of structural dynamics. The first two section of this chapter introduces the derivation of the mode shapes regarding different boundary conditions. Subsequently, the methods of the modal analysis and the frequency domain analysis are briefly introduced.

3.1. Euler-Bernoulli beam model

The submerged floating tunnel is expected to deform horizontally and vertically and is therefore modeled with an Euler-Bernoulli beam model. An Euler-Bernoulli beam is modeled as a continuous system with an infinite number of spatial nodes for each DOF. Figure 3.1 shows a beam subjected to a vertical load resulting in transverse motion. This vertical load varies both in space and time.

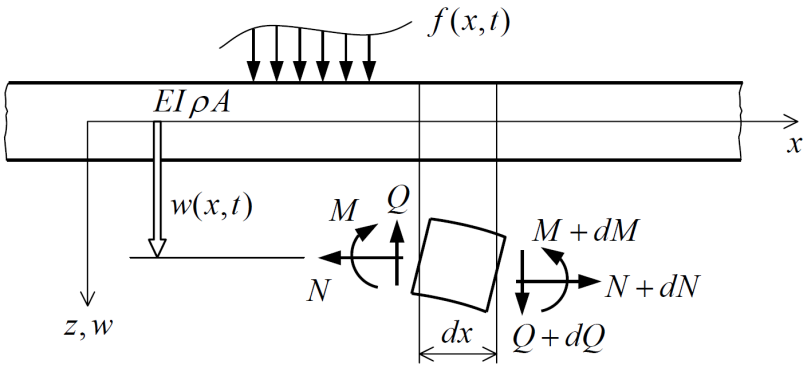

Figure 3.1: Sign convention of an Euler-Bernoulli beam (Spijkers et al., 2006)

3.1.1. Equations of motion

Euler-Bernoulli beam model states that the plane cross-section, which is initially perpendicular to the axis of the beam, remains plane and perpendicular to the neutral axis during vertical motion. According to this theory and applying Newton's second law the following relation holds:

$$EI\frac{\partial^4 w(x,t)}{\partial x^4} + \rho A\frac{\partial^2 w(x,t)}{\partial t^2} = f(x,t), \tag{3.1}$$

where:

E	=	Young's modulus	[N·m^{-2}],
I	=	Second moment of area	[m^4],
ρ	=	Density	[kg·m^{-3}],
A	=	Cross-sectional area	[m^2].

For convenience sake, using Newton's notation for differentiation of t (i.e. using dot mark) and Lagrange's notation for differentiation of x (i.e. using prime mark), the equation is rewritten as follows:

$$EIw''''(x,t) + \rho A\ddot{w}(x,t) = f(x,t). \tag{3.2}$$

Note that with this analysis the deformation due to the shear force and the influence of the rotational inertia are not taken into account, which is justified for slender beams and low natural frequency.

3.1.2. Eigenvalue problem

The free vibration represents the dynamic behaviour of the non-loaded bending beam; this vibration is described by means of the homogeneous partial differential equation:

$$EIw''''(x,t) + \rho A\ddot{w}(x,t) = 0. \tag{3.3}$$

The response can be written as the product of an unknown space function $w(x)$ and a harmonic time function $w(t) = \sin(\omega t + \phi)$ (separation of variables):

$$w(x,t) = w(x)\sin(\omega t + \phi). \tag{3.4}$$

Substitution of the synchronic harmonic motion in the partial differential equation provides an ordinary fourth-order differential equation with respect to the space function $w(x)$. This differential equation is also called the eigenvalue problem. The solution $w(x)$ of the eigenvalue problem is called the eigenfunction. When determining the eigenfunction it will be shown that the frequency ω can only adopt specific values. These frequencies are called natural frequencies. The eigenvalue problem is noted as follows:

$$w''''(x) - \beta^4 w(x) = 0, \tag{3.5}$$

where:

$$\beta^4 = \frac{\rho A\omega^2}{EI} \quad .$$

The solution of $w(x)$ consists of four contributions:

$$w(x) = C_1 e^{\beta x} + C_2 e^{-\beta x} + C_3 e^{\mathrm{i}\beta x} + C_4 e^{-\mathrm{i}\beta x}, \tag{3.6}$$

Rearrangement of these terms gives a real eigenfunction $w(x)$:

$$w(x) = A\cosh\beta x + B\sinh\beta x + C\cos\beta x + D\sin\beta x. \tag{3.7}$$

The values of the five constants A, B, C, D and β depend on how the beam is supported, i.e. depend on the applied boundary conditions. Normally, there are three kinds of boundary conditions for SFTs regarding to different shore connection, which are both end pinned, both end fixed and both end free.

	Deflection w	**Slope** w'	**Bending Moment** $-EIw''$	**Shear force** $-EIw'''$
Fixed	0	0	/	/
Pinned	0	/	0	/
Free	/	/	0	0

Table 3.1: Three kinds of boundary conditions

3.1.2.1. Both end pinned beam

The both end pinned beam is also called simply supported beam, of which the boundary conditions are very simple: the displacement and the bending moment for both ends are equal to zero. Substitution of the four mentioned boundary conditions into the expression for the eigenfunction $w(x)$, gives the following set of algebraic equations:

$$\begin{aligned}
w(0) = 0 \quad &\Longrightarrow \quad A + C = 0, \\
w''(0) = 0 \quad &\Longrightarrow \quad A - C = 0, \\
w(l) = 0 \quad &\Longrightarrow \quad A\cosh\beta l + B\sinh\beta l + C\cos\beta l + D\sin\beta l = 0, \\
w''(l) = 0 \quad &\Longrightarrow \quad A\beta^2\cosh\beta l + B\beta^2\sinh\beta l - C\beta^2\cos\beta l - D\beta^2\sin\beta l = 0.
\end{aligned}$$

Solving these algebraic equations yields the eigenfrequencies (natural frequencies) and the eigenfunctions (mode shapes):

$$\omega_n = \beta_n^2\sqrt{\frac{EI}{\rho A}} = n^2\left(\frac{\pi}{l}\right)^2\sqrt{\frac{EI}{\rho A}}, \tag{3.8}$$

$$w_n(x) = \hat{w}_n\sin(\beta_n x) = \hat{w}_n\sin(\frac{n\pi}{l}x) = \hat{w}_n\sin(2\pi\frac{x}{\lambda_n}), \tag{3.9}$$

where:

$$\begin{aligned}
\hat{w}_n \quad &= \quad 1, \text{ the amplitude of the mode shapes, normally is set to 1,} \\
\beta_n \quad &= \quad \frac{n\pi}{l}, \\
n \quad &= \quad 1,2,\ldots\infty, \\
\lambda_n \quad &= \quad \frac{2l}{n}, \text{ the wavelength of the } n^{th} \text{ eigenfunction.}
\end{aligned}$$

In Figure 3.2 the first three eigenfunctions are displayed, each with an amplitude of $\hat{w}_n$.

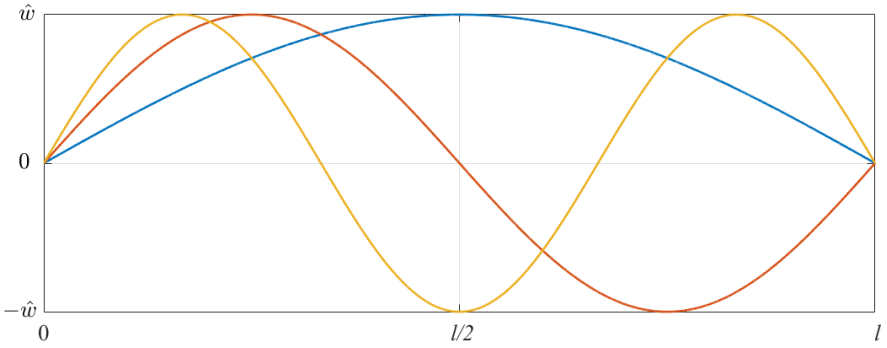

Figure 3.2: The first three eigenmodes of both end pinned beam

3.1.2.2. Both end fixed beam

The second case is the both end fixed beam: the displacement and the slope for both ends are equal to zero. Substitution of the four mentioned boundary conditions into the expression for the eigenfunction $w(x)$ gives:

$$\begin{aligned}
w(0) = 0 \quad &\Longrightarrow \quad A + C = 0, \\
w'(0) = 0 \quad &\Longrightarrow \quad B + D = 0, \\
w(l) = 0 \quad &\Longrightarrow \quad A\cosh\beta l + B\sinh\beta l + C\cos\beta l + D\sin\beta l = 0, \\
w'(l) = 0 \quad &\Longrightarrow \quad A\beta\sinh\beta l + B\beta\cosh\beta l - C\beta\sin\beta l + D\beta\cos\beta l = 0.
\end{aligned}$$

Solving these algebraic equations yields the eigenfrequencies (natural frequencies) and the eigenfunctions (mode shapes):

$$\omega_n = \beta_n^2 \sqrt{\frac{EI}{\rho A}} = \frac{(2n+1)^2}{4} \left(\frac{\pi}{l}\right)^2 \sqrt{\frac{EI}{\rho A}}, \tag{3.10}$$

$$w_n(x) = \hat{w}_n \left[\sin(\beta_n x) + \frac{\cos(\beta_n x)(\sinh(\beta_n l) - \sin(\beta_n l))}{\cos(\beta_n l) - \cosh(\beta_n l)} - \sinh(\beta_n x) - \frac{\cosh(\beta_n x)(\sinh(\beta_n l) - \sin(\beta_n l))}{\cos(\beta_n l) - \cosh(\beta_n l)} \right], \tag{3.11}$$

where:

$$\begin{aligned} \beta_n &= \frac{(2n+1)\pi}{2l}, \\ n &= 1, 2, \ldots \infty. \end{aligned}$$

In Figure 3.3 the first three eigenfunctions are displayed, each with an amplitude of $\hat{w}_n$.

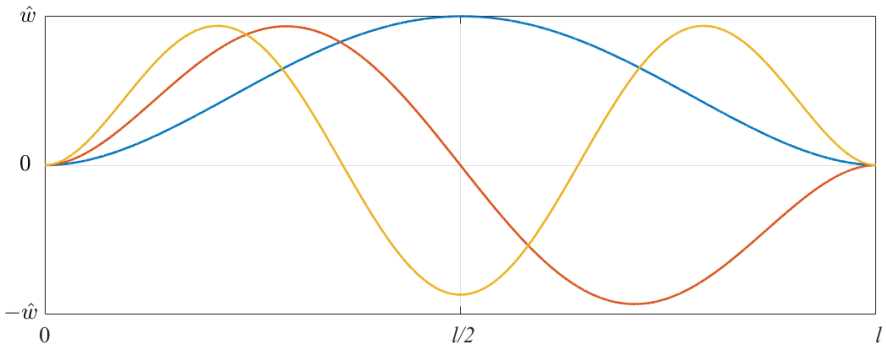

Figure 3.3: The first three eigenmodes of both end fixed beam

3.1.2.3. Both end free beam

The boundary conditions for the both end free beam is similar with the previous two cases: the bending moment and the shear force for both ends are equal to zero. Substitution of the four mentioned boundary conditions into the expression for the eigenfunction $w(x)$ gives:

$$\begin{aligned} w''(0) = 0 \quad &\Longrightarrow \quad A - C = 0, \\ w'''(0) = 0 \quad &\Longrightarrow \quad B - D = 0, \\ w''(l) = 0 \quad &\Longrightarrow \quad A\beta^2 \cosh\beta l + B\beta^2 \sinh\beta l - C\beta^2 \cos\beta l - D\beta^2 \sin\beta l = 0, \\ w'''(l) = 0 \quad &\Longrightarrow \quad A\beta^3 \sinh\beta l + B\beta^3 \cosh\beta l + C\beta^3 \sin\beta l - D\beta^3 \cos\beta l = 0. \end{aligned}$$

Solving these algebraic equations yields the eigenfrequencies (natural frequencies) and the eigenfunctions (mode shapes):

$$\omega_n = \beta_n^2 \sqrt{\frac{EI}{\rho A}} = \begin{cases} 0 & n = 1 \\ \dfrac{(2n-1)^2}{4} \left(\dfrac{\pi}{l}\right)^2 \sqrt{\dfrac{EI}{\rho A}} & n \geq 2 \end{cases}, \tag{3.12}$$

$$w_n(x) = \begin{cases} 1 & n = 1 \\ \hat{w}_n \left(\dfrac{2x}{l} - 1\right) & n = 2 \\ \hat{w}_n \left[\sinh(\beta_n x) - \dfrac{(\sinh(\beta_n l) - \sin(\beta_n l))\cosh(\beta_n x)}{-\cos(\beta_n l) + \cosh(\beta_n l)} + \sin(\beta_n x) - \dfrac{(\sinh(\beta_n l) - \sin(\beta_n l))\cos(\beta_n x)}{-\cos(\beta_n l) + \cosh(\beta_n l)} \right] & n \geq 3 \end{cases}, \tag{3.13}$$

where:

$$\begin{aligned} \beta_n &= \begin{cases} 0 & n = 1 \\ \dfrac{(2n-3)\pi}{2l} & n \geq 2 \end{cases}, \\ n &= 1, 2, \ldots \infty. \end{aligned}$$

In Figure 3.4 the first four eigenfunctions are displayed, each with an amplitude of $\hat{w}_n$. Note that the first mode of the both end free beam is actually a rigid body vibration, which implies the first mode can be treated as a mass-spring rigid body system when combined with a distributed spring.

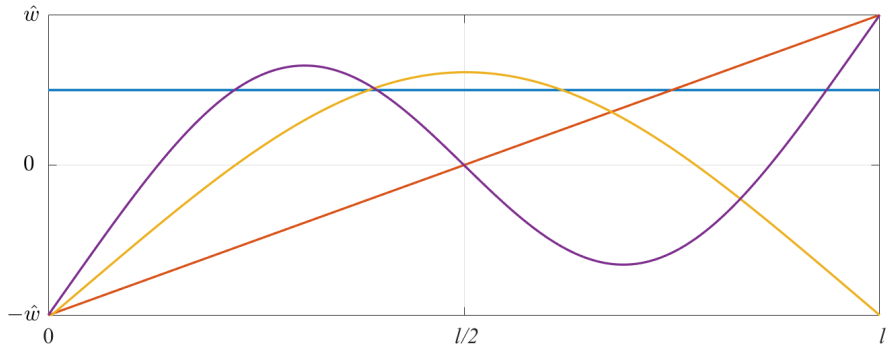

Figure 3.4: The first four eigenmodes of both end free beam

3.2. Torsion rod model

The rotation in the cross-section of the SFT is another relevant degree of freedom in the study. The rotation in the cross-section can be captured by a torsion rod model as shown in Figure 3.5.

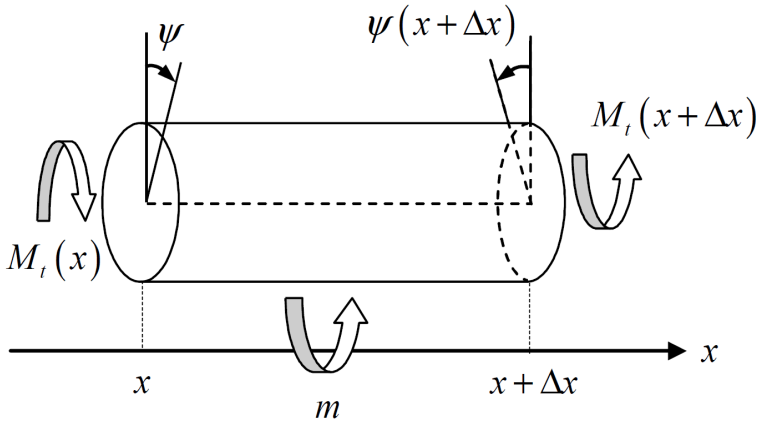

Figure 3.5: Sign convention of an torsion rod

3.2.1. Equations of motion

According to the sign convention in Figure 3.5 the following relation holds:

$$GI_p \frac{\partial^2 \Psi(x,t)}{\partial x^2} + \rho I \frac{\partial^2 \Psi(x,t)}{\partial t^2} = M_t(x,t), \tag{3.14}$$

where:

G	=	Shear modulus	[N·m^{-2}],
I_p	=	Torsional constant	[m^4],
ρ	=	Density	[kg·m^{-3}],
I	=	Polar moment of inertia	[m^4].

Note that the cross-section of a circular rod under torsion does not warp because of circular symmetry, which means $I_p = I = \frac{\pi d^4}{32}$. Similar with Equation 3.1, the equation can be rewrited as :

$$GI_p\Psi''(x,t) + \rho I\ddot{\Psi}(x,t) = M_t(x,t). \tag{3.15}$$

3.2.2. Eigenvalue problem

This partial differential equation can be solved by the separation of variables method as well, which yields:

$$\Psi''(x) + \beta^2\Psi(x) = 0, \tag{3.16}$$

where:

$$\beta^2 = \frac{\rho I\omega^2}{GI_p} \quad .$$

The solution $\Psi(x)$ consists of two contributions, which can be expected from the second-order differential equation:

$$\Psi(x) = C_1 e^{\mathrm{i}\beta x} + C_2 e^{-\mathrm{i}\beta x}. \tag{3.17}$$

By means of Euler's formula this can be written as a real function of the position variable x:

$$\Psi(x) = A\sin\beta x + B\cos\beta x. \tag{3.18}$$

The eigenfunction still contains three unknown constants: A, B and β. These are determined by the boundary conditions as shown in Table 3.2.

	Angle of rotation Ψ	**Torque** $GI_p\Psi'$
Fixed	0	/
Free	/	0

Table 3.2: Two kinds of boundary conditions

3.2.2.1. Both end fixed torsion rod

The rotational angle for both ends of the fixed torsion rod are equal to zero. Substitution of the two mentioned boundary conditions into the expression for the eigenfunction $\Psi(x)$:

$$\begin{aligned} \Psi(0) = 0 \quad &\Longrightarrow \quad B = 0, \\ \Psi(l) = 0 \quad &\Longrightarrow \quad A\sin\beta l + B\cos\beta l = 0. \end{aligned}$$

Solving these algebraic equations yields the eigenfrequencies (natural frequencies) and the eigenfunctions (mode shapes):

$$\omega_n = \beta_n\sqrt{\frac{GI_p}{\rho I}} = n\frac{\pi}{l}\sqrt{\frac{GI_p}{\rho I}}, \tag{3.19}$$

$$\Psi_n(x) = \hat{w}_n\sin(\beta_n x) = \hat{w}_n\sin(\frac{n\pi}{l}x), \tag{3.20}$$

where:

$$\begin{aligned} \beta_n &= \frac{n\pi}{l}, \\ n &= 1,2,\ldots\infty. \end{aligned}$$

In Figure 3.6 the first three eigenfunctions are displayed, each with an amplitude of $\hat{w}_n$.

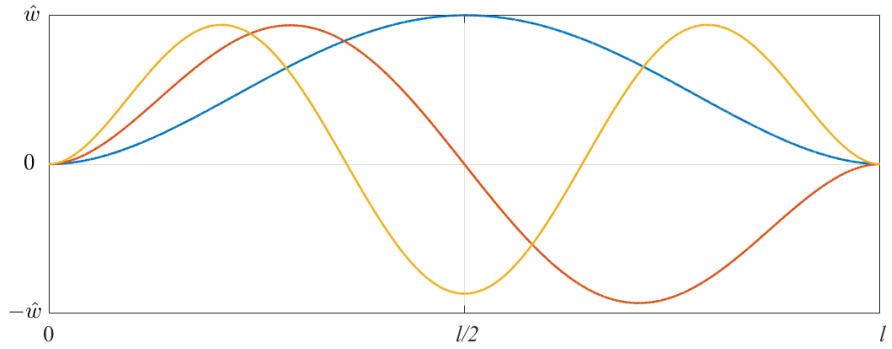

Figure 3.6: The first three eigenmodes of both end fixed torsion rod

3.2.2.2. Both end free torsion rod

Similar to the previous case, the torque for both ends of the free torsion rod are equal to zero. Substitution of the two mentioned boundary conditions into the expression for the eigenfunction $\Psi(x)$:

$$\begin{aligned} \Psi'(0) = 0 \quad &\Longrightarrow \quad A = 0, \\ \Psi'(l) = 0 \quad &\Longrightarrow \quad A\beta\cos\beta l - B\beta\sin\beta l = 0. \end{aligned}$$

Solving these algebraic equations yields the eigenfrequencies (natural frequencies) and the eigenfunctions (mode shapes):

$$\omega_n = \beta_n\sqrt{\frac{GI_p}{\rho I}} = n\frac{\pi}{l}\sqrt{\frac{GI_p}{\rho I}}, \tag{3.21}$$

$$\Psi_n(x) = \begin{cases} 1 & n = 1 \\ \hat{w}_n\cos(\beta_n x) & n \geq 2 \end{cases}, \tag{3.22}$$

where:

$$\begin{aligned} \beta_n &= \begin{cases} 0 & n = 1 \\ \dfrac{(n-1)\pi}{l} & n \geq 2 \end{cases}, \\ n &= 1,2,\ldots\infty. \end{aligned}$$

In Figure 3.7 the first four eigenfunctions are displayed, each with an amplitude of $\hat{w}_n$. The first mode of the both end free torsional rod is a rigid body vibration, which implies the first mode can be treated as a mass-spring rigid body system when combined with a distributed spring.

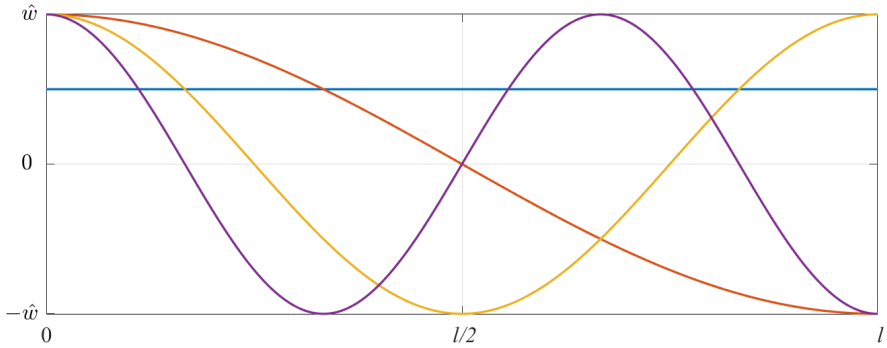

Figure 3.7: The first four eigenmodes of both end free torsion rod

3.3. Modal analysis

Analogue to the free vibration in the previous sections, the solutions for the forced vibration (the particular solution) are also assumed to be a summation of eigenfunctions, but in this case each eigenfunction is multiplied with an unknown time function:

$$w(x,t) = \sum_{i=1}^{n} w_i(x)\,u_i(t) = \sum_{i=1}^{n} w_i(x)\sin(\omega_i t + \phi_i). \tag{3.23}$$

Note that also here a summation of synchronised motions is assumed. This assumption is the essence of the so-called *Modal Analysis*. Translated in mathematical terminology, it is thus assumed that also in the case of forced vibration the response can be expanded in eigenfunctions each weighed with an unknown time function. Substitution of the assumed solution in Equation 3.3 (take both ends pinned Euler-Bernoulli beam model for example) results in the equations to which the unknown functions $u_i(t)$ have to comply:

$$EI\sum_{i=1}^{n} \beta_i^4\, w_i(x)\,u_i(t) + \rho A \sum_{i=1}^{n} w_i(x)\,\ddot{u}_i(t) = f(x,t). \tag{3.24}$$

By means of the orthogonality conditions:

$$\int_0^l w_n(x)\,w_m(x)\mathrm{d}x = 0 \qquad (n \neq m), \tag{3.25}$$

multiplying both side of the Equation 3.24 by another mode i.e. $w_m(x)$ and integrating over the length of the beam yields:

$$EI\beta_m^4 u_m(t)\int_0^l w_m^2(x)\mathrm{d}x + \rho A\ddot{u}_m(t)\int_0^l w_m^2(x)\mathrm{d}x = \int_0^l w_m(x)\,f(x,t)\mathrm{d}x. \tag{3.26}$$

Now the equation is a set of ordinary differential equations with respect to x, which can be solved for each mode by using MATLAB® ODE solver.

3.4. Frequency domain analysis

After solving the equation of forced vibration in MATLAB®, the response is obtained in time domain. To study the frequency components in this time signal, a frequency domain analysis is carried out. This analysis is executed with the help of a Fourier transform and a Wavelet transform. The Fourier transform gives the information on the frequency content but is not capable to show how these frequencies change over time. The Wavelet transform, however, provides the information on both the time location and frequency of a signal.

3.4.1. Fourier transform

The Fourier transform is a reversible, linear transform which converts a time-domain signal of infinite duration into a continuous spectrum composed of an infinite number of sinusoids. There are several common conventions for defining the Fourier transform of an integrable function. In Structural Engineering, it is normally defined as:

$$X(f) = \int_{-\infty}^{\infty} x(t)\,e^{-j2\pi f t}\,dt, \tag{3.27}$$

where:

$x(t)$	=	Time domain signal,
$X(f)$	=	Frequency domain representation,
j	=	The imaginary unit.

The solution to the equation of forced vibration contains the transient and forced parts. The forced part of the solution is often referred to as the *steady state* solution, since it is the solution which remains after the transient response has died out. In practice, only the steady state response is of interest, so the Fourier transform is normally applied to a steady state signal and does not give the access to the time information.

When the information on how the frequency content changes over time is needed, a short-time Fourier transform is applied. The function to be transformed is multiplied by a window function which is nonzero for only a short period of time. This divides the time signal into shorter segments of equal length and then computes the Fourier transform separately on each shorter segment. A short-time Fourier transform is defined as:

$$X(\tau, f) = \int_{-\infty}^{\infty} x(t)\, w(t-\tau) e^{-j2\pi f t}\, dt, \tag{3.28}$$

where:

$x(t)$	=	Time domain signal,
$X(\tau, f)$	=	Two-dimensional representation of the signal ,
$w(\tau)$	=	The window function,
j	=	The imaginary unit.

This reveals the Fourier spectrum on each short segment and therefore indicates how it changes over time. However, the resolution issues are arisen when applying a short-time Fourier transform. The width of the window function relates to how the signal is represented—it determines whether there is good frequency resolution (frequency components close together can be separated) or good time resolution (the time at which frequencies change). A wide window gives better frequency resolution but poor time resolution. A narrower window gives good time resolution but poor frequency resolution. A better approach is to apply the wavelet transform, which gives good time resolution for high-frequency events and good frequency resolution for low-frequency events.

3.4.2. Wavelet transform

The wavelet transform is similar to the short-time Fourier transform but applies a bigger time window to catch lower frequencies and a smaller window for higher frequencies. Generally, the wavelet transform is defined as:

$$X(a, b) = \frac{1}{\sqrt{a}} \int_{-\infty}^{\infty} x(t) \Psi\left(\frac{t-b}{a}\right) dt, \tag{3.29}$$

$x(t)$	=	Time domain signal,
$X(a, b)$	=	Two-dimensional representation of the signal,
$\Psi(t)$	=	The mother wavelet,
a	=	The scale, indicating the frequency information,
b	=	The translation, indicating the time information.

With additional special properties of the wavelets, the wavelet transform features good performance in both time and frequency resolutions. In MATLAB® wavelet transform is obtained using the analytic Morse wavelet. For a detailed explanation of the parameterization of Morse wavelets, refer to Olhede and Walden (2002).

3.5. Conclusion

The summary of the important findings in this chapter:

- Three boundary conditions in translational direction and two boundary conditions in rotational direction are derived, which can be used to simulate the boundary conditions of the SFT by combining them together.
- The modal analysis can be used to extract natural frequencies from the response of the tunnel.
- The frequency domain analysis can be used to investigate the frequency components of a time domain signal. The frequency components of the steady state of the response is of practical interest.
- The Fourier transform is applied when only the frequency content is of interest. If the change of the frequency content over time is needed, wavelet transform would be a better option.

4

Hydrodynamics relevant to a SFT

Wave and current loads are considered to be the governing dynamic load for a SFT in this research. To analyse the response of a SFT due to this hydrodynamic loading, it is important to comprehend the physics behind it. First, a general description of waves is presented in section 4.1 to explain the terminology. Subsequently, the methods to describes the hydrodynamic forces are explained in section 4.2.

4.1. Linear wave theory

As mentioned in chapter 2, linear wave theory for surface gravity waves is based on only two fundamental equations (a mass balance equation and a momentum balance equation) and some simple boundary conditions, describing certain kinematic and dynamic aspects of the waves. When these equations and boundary conditions are linearised, freely propagating, harmonics waves are solutions of these equations. The main requirement for the linear theory to apply is that the amplitudes of the waves are small, i.e. small compared with the wave length and small compared with the water depth (Holthuijsen, 2010), which is called the *small-amplitude approximation*.

A SFT is generally located in deep waters, such that the waves are not affected by the seabed. The water is only subjected to only one external load, gravity. The linear wave theory is, therefore, suitable to describe the harmonic waves in this case.

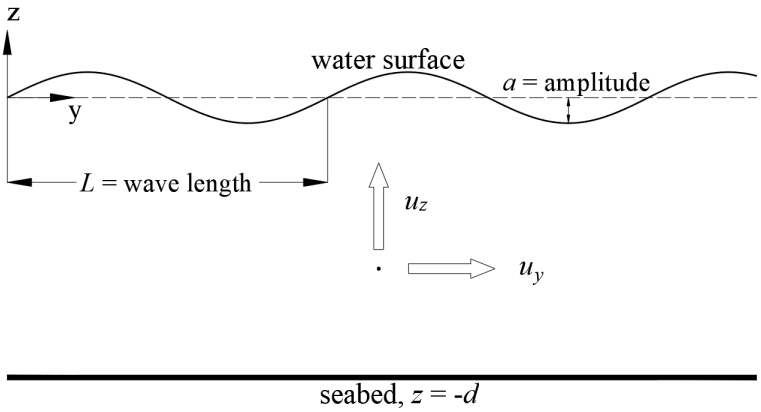

Figure 4.1: The particle velocities of waves

Based on linear wave theory, the particle velocities of the waves are given by:

$$\begin{cases} u_y(t) = \omega a \dfrac{\cosh(k(d+z))}{\sinh(kd)} \sin(\omega t) \\ u_z(t) = \omega a \dfrac{\sinh(k(d+z))}{\sinh(kd)} \cos(\omega t) \end{cases}, \tag{4.1}$$

where:

ω	=	Wave frequency	[rad $\cdot s^{-1}$],
a	=	Wave amplitude	[m],
k	=	Wave number	[m^{-1}],
d	=	Water depth	[m].

The direction of the velocities are shown in Figure 4.1. The amplitude is half of the wave height and the wave number k is determined by $\omega^2 = gk\tanh(kd)$.

4.2. Hydrodynamic forces

Now that the basics of the linear wave theory have been discussed in the previous section, the next step is to consider the hydrodynamic load. Two methods are explained below to describe the forces in in-line direction and the forces in cross-flow direction.

4.2.1. Morison equation

The Morison equation is a semi-empirical equation for the in-line force on a body in oscillatory flow. It is the sum of two force components: an inertia force in phase with the local flow acceleration and a drag force proportional to the (signed) square of the instantaneous flow velocity. The inertia force is of the functional form as found in potential flow theory, while the drag force has the form as found for a body placed in a steady flow. In the heuristic approach of Morison, O'Brien, Johnson and Schaaf these two force components, inertia and drag, are simply added to describe the in-line force in an oscillatory flow. The transverse force—perpendicular to the flow direction, due to vortex shedding—has to be addressed separately, which is discussed in the next section.

For a moving body in an oscillatory flow, the Morison equation gives the in-line force parallel to the flow direction:

$$\mathbf{F} = \rho V \dot{\mathbf{u}} + \rho C_a V(\dot{\mathbf{u}} - \dot{\mathbf{v}}) + \frac{1}{2}\rho C_d A(\mathbf{u} - \mathbf{v})|\mathbf{u} - \mathbf{v}|, \tag{4.2}$$

where:

$\mathbf{u}$	=	Flow velocity	[m $\cdot$ s^{-1}],
$\dot{\mathbf{u}}$	=	Flow acceleration	[m $\cdot$ s^{-2}],
$\mathbf{v}$	=	Structure velocity	[m $\cdot$ s^{-1}],
$\dot{\mathbf{v}}$	=	Structure acceleration	[m $\cdot$ s^{-2}],
ρ	=	Water density	[kg $\cdot$ m^{-3}],
V	=	Volume of the body	[m^3],
A	=	Cross-sectional area	[m^2],
C_a	=	Added mass coefficient	[-],
C_d	=	Drag coefficient	[-].

The first two terms denote the inertia force, which is the sum of the Froude–Krylov force and the hydrodynamic mass force. The third term denotes the drag force according to the drag equation.

The added mass coefficient and the drag coefficient are two empirical hydrodynamic coefficients, which are determined from experimental data. As shown by dimensional analysis and in experiments by Sarpkaya, these coefficients depend in general on the Keulegan–Carpenter number, Reynolds number and surface roughness(Sarpkaya, 1976).

The Morison equation has three limitations. The first limitation is that the flow acceleration should be approximately uniform at the location of the body. For instance, the diameter of a cylinder in surface gravity waves should be much smaller than the wavelength. If the diameter of the body is not small compared to the wavelength, diffraction effects have to be taken into account (Patel and Witz, 2013). Second, it is assumed that the asymptotic forms, the inertia and drag force contributions, valid for very small and very large Keulegan–Carpenter numbers respectively, can just be added to describe the force fluctuations at intermediate Keulegan–Carpenter numbers (Sarpkaya, 2010). Third, when extended to orbital flow which is a case of non uni-directional flow, for instance, encountered by a horizontal cylinder under waves, the Morison equation does not give a good representation of the forces as a function of time(Chaplin, 1984).

4.2.2. Wake oscillator

Another situation of the hydrodynamic loading is the cross-flow vortex loading. Vortex induced vibration is a result of this loading. Two semi-empirical models are often used to analyze VIV, which is the force-decomposition model and the wake oscillator model. For a review on VIV modeling see (Gabbai and Benaroya, 2005). In this report, the wake oscillator model is used because this model finds the frequency and amplitude of the cylinder motion and the cross-flow fluid force on its own accord. This makes it possible to capture multi-mode VIV of long flexible cylinders.

Wake oscillator models couple the equations of structural motion with a nonlinear oscillator equation that describes the cross-flow fluid force. In most cases, an equation of the Van der Pol or Rayleigh type is used, as these equations predict a limit cycle in the phase space (Ogink and Metrikine, 2010). To fully describe the motions of a moving body under vortex loading some definitions are needed. The sign convention of a loading system is shown in Figure 4.2. The wake oscillator model for this system is defined as:

$$\begin{cases} (m+m_a)\ddot{y} + c_y\dot{y} + k_y y = \frac{1}{2}\rho D L u_y^2 C_{Vy}(\dot{y},\dot{z},q) \\ (m+m_a)\ddot{z} + c_z\dot{z} + k_z z = \frac{1}{2}\rho D L u_y^2 C_{Vz}(\dot{y},\dot{z},q) \\ \ddot{q} + \varepsilon\omega_s(q^2-1)\dot{q} + \omega_s^2 q = \frac{A}{D}\ddot{z} \end{cases} , \tag{4.3}$$

where:

m	=	The cylinder mass	[kg],
m_a	=	$C_a\pi\rho D^2 L/4$, the added mass	[kg],
q	=	The wake parameter	[-],
ε	=	A nondimensional tuning parameter	[-],
ω_s	=	The vortex shedding frequency	[rad$\cdot$ s^{-1}].

The incoming flow is in-line with y-direction. Therefore, y-direction is the in-line direction and z-direction is the cross-flow direction. The cylinder itself is moving with velocity $\dot{y}$ and $\dot{z}$. The relative velocity is then calculated as $u_r = \sqrt{u_{y,r}^2 + u_{z,r}^2} = \sqrt{(u_y - \dot{y})^2 + \dot{z}^2}$. The angle between u_y and u_r is defined as β.

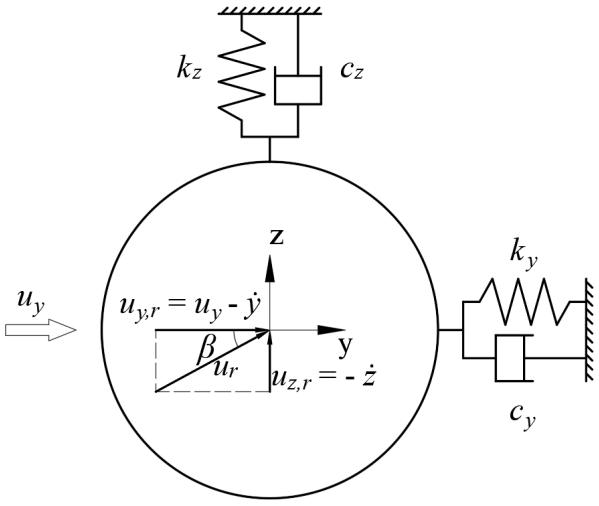

Figure 4.2: cross-section of a cylinder on visco-elastic supports (velocity)

Given the flow velocities, the fluid forces acting on the system can be defined. Figure 4.3 shows the decomposition of the vortex fluid force in drag , lift horizontal and vertical direction. The vortex drag force F_{VD} is inline with the relative velocity and the vortex lift force F_{VL} is perpendicular to the relative velocity. Then the in-line force F_{Vy} and the cross-flow force F_{Vz} are composed of a drag term and a lift term:

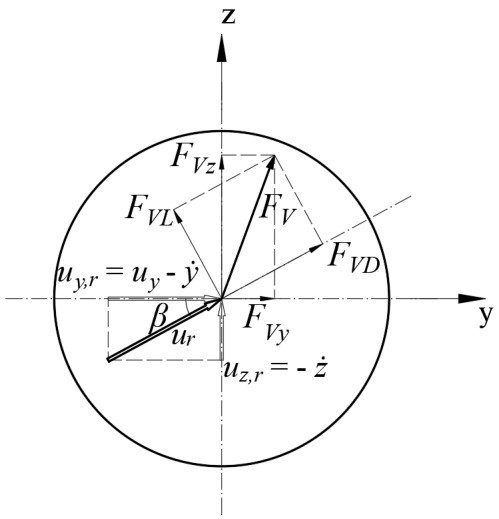

Figure 4.3: cross-section of a cylinder on visco-elastic supports (forces)

$$\begin{cases} F_{Vy} = F_{VD}\cos\beta - F_{VL}\sin\beta \\ F_{Vz} = F_{VD}\sin\beta + F_{VL}\cos\beta \end{cases}. \tag{4.4}$$

Expressing the forces in the form with force coefficients results in the flowing equations:

$$\begin{cases} \frac{1}{2}\rho D L u_y^2 C_{Vy} = \left(C_{VD}\cos\beta - C_{VL}\sin\beta\right)\frac{1}{2}\rho D L u_r^2 \\ \frac{1}{2}\rho D L u_y^2 C_{Vz} = \left(C_{VD}\sin\beta + C_{VL}\cos\beta\right)\frac{1}{2}\rho D L u_r^2 \end{cases}. \tag{4.5}$$

After simplification of the equations, the in-line and cross-flow force coefficients are expressed as:

$$\begin{cases} C_{Vy} = \left(C_{VD}\cos\beta - C_{VL}\sin\beta\right)\frac{u_r^2}{u_y^2} \\ C_{Vz} = \left(C_{VD}\sin\beta + C_{VL}\cos\beta\right)\frac{u_r^2}{u_y^2} \end{cases}. \tag{4.6}$$

As shown in Figure 4.3, β is the angle between the direction of flow velocity and the direction of the relative velocity, which is given by:

$$\begin{aligned} \sin\beta &= \frac{u_{z,r}}{u_r} = \frac{-\dot{z}}{\sqrt{(u_y-\dot{y})^2+\dot{z}^2}}, \\ \cos\beta &= \frac{u_{y,r}}{u_r} = \frac{u_y-\dot{y}}{\sqrt{(u_y-\dot{y})^2+\dot{z}^2}}. \end{aligned} \tag{4.7}$$

By assuming that the cylinder velocity is considerably smaller than the flow velocity and that therefore the angle β is considerably smaller than 1, Equation 4.7 is then simplified as $\sin\beta \approx \beta \approx \frac{-\dot{z}}{u_y-\dot{y}}$ and $\cos\beta \approx 1$. Hence:

$$\begin{cases} C_{Vy} = C_{VD} + C_{VL}\frac{\dot{z}}{u_y-\dot{y}} \\ C_{Vz} = -C_{VD}\frac{\dot{z}}{u_y-\dot{y}} + C_{VL} \end{cases}. \tag{4.8}$$

According to Ogink and Metrikine (2010), the drag component of the vortex force is constant and that the lift component of the vortex force is linearly related to the wake variable q. This means that C_{VD} should be equal to the constant in-line force coefficient measured for a stationary cylinder and that C_{VL} should be equal to the oscillating cross- flow coefficient measured for a stationary cylinder:

$$C_{VD} = C_{D0}, \quad C_{VL} = \frac{1}{2} C_{L0} q. \tag{4.9}$$

After performing the necessary substitutions into Equation 4.3, the wake oscillator model is finally given in nonlinear form by:

$$\begin{cases} (m+m_a)\ddot{y} + c_y\dot{y} + k_y y = \frac{1}{2}\rho D L u_y^2 \left(C_{D0}(u_y - \dot{y}) + \frac{1}{2} C_{L0} q \dot{z} \right) \frac{\sqrt{(u_y-\dot{y})^2 + \dot{z}^2}}{u_y^2} \\ (m+m_a)\ddot{z} + c_z\dot{z} + k_z z = \frac{1}{2}\rho D L u_y^2 \left(-C_{D0}\dot{z} + \frac{1}{2} C_{L0} q (u_y - \dot{y}) \right) \frac{\sqrt{(u_y-\dot{y})^2 + \dot{z}^2}}{u_y^2} \\ \ddot{q} + \varepsilon\omega_s(q^2-1)\dot{q} + \omega_s^2 q = \frac{A}{D}\ddot{z} \end{cases}, \tag{4.10}$$

and after simplification by:

$$\begin{cases} (m+m_a)\ddot{y} + c_y\dot{y} + k_y y = \frac{1}{2}\rho D L u_y^2 (C_{D0} + \frac{1}{2} C_{L0} q \frac{\dot{z}}{u_y - \dot{y}}) \\ (m+m_a)\ddot{z} + c_z\dot{z} + k_z z = \frac{1}{2}\rho D L u_y^2 (-C_{D0} \frac{\dot{z}}{u_y - \dot{y}} + \frac{1}{2} C_{L0} q) \\ \ddot{q} + \varepsilon\omega_s(q^2-1)\dot{q} + \omega_s^2 q = \frac{A}{D}\ddot{z} \end{cases}. \tag{4.11}$$

4.3. Conclusion

These conclusions contribute to the development of the submerged floating tunnel model:

- The Morison equation can be used to study the load case of combined wave and current loading and the load case of oblique wave loading.
- When the current speed is considerably large and the vortex shedding is expected, the wake oscillator model can be used to investigate the response due to VIV considering the cross-flow forces.

II

Model development

5

Model for anchoring system

This chapter describes the approach which is used to model the anchoring system of the SFT. Two different kinds of assumptions are discussed: geometrically linear stiffness and geometrically nonlinear stiffness. Subsequently, the assumptions which are made to model the anchoring system are discussed in section 5.2.

5.1. Model set-up

Two different models are developed: a linear stiffness model and a nonlinear stiffness model. Both models are developed in MATLAB as functions giving output of reaction force in horizontal , vertical and rotational degrees of freedom. The function can be schematized with the following diagram:

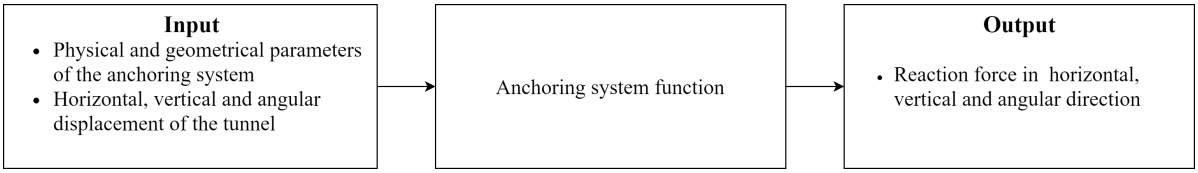

Figure 5.1: Flow scheme of the anchoring system function

Figure 5.1 shows that the physical and the geometrical parameters of the anchoring systems (listed in Table 7.4) and the displacement in three direction of the tunnel (i.e. Δy, Δz and $\Delta\varphi$) are required as input of for the function. The reaction forces in three directions (i.e. F_y, F_z and F_φ) can then be determined.

5.1.1. Linear stiffness model

For the linear case, the displacements in three degrees of freedom are independent of each other. Applying the displacement method, the restoring forces can be obtained. For that purpose, the structure is drawn in three positions as shown in Figure 5.2, Figure 5.3 and Figure 5.4. In these figures, one degree of freedom is assumed to be positive in turns with the two others held fixed, which means they are supposed to be zero.

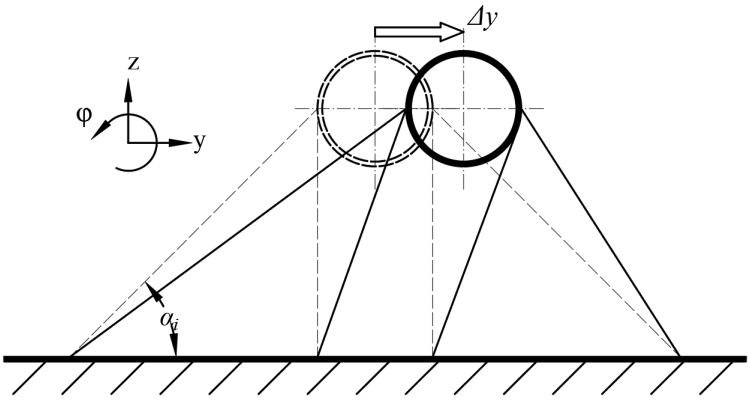

Figure 5.2: Action of the horizontal degree of freedom

In Figure 5.2, the tunnel cross section moves horizontally with a displacement of Δy, which is considered small so that the contribution of the vertical line to the horizontal restoring force and the change of the angle of inclination can be ignored. The restoring forces are defined as the generalized forces in the usual manner, i.e. F_{zy} is the force in the z-direction which results from a displacement in the y-direction and $F_{\varphi z}$ is the moment in the φ-direction which results from a displacement in the z-direction. The positive directions of the restoring forces are defined as the opposite of the displacement. Therefore, the following relations hold:

$$
\begin{aligned}
F_{yy} &= T_i + k_i \Delta y \cos^2 \alpha_i - (T_i - k_i \Delta y \cos^2 \alpha_i) = 2k_i \cos^2 \alpha_i \Delta y, && (\leftarrow) \\
F_{zy} &= T_i + k_i \Delta y \cos \alpha_i \sin \alpha_i + T_i + k_i \Delta y \cos \alpha_i \sin \alpha_i + 2T_v - F_{NB} = 0, && (\downarrow) \\
F_{\varphi y} &= -(T_i + k_i \Delta y \cos \alpha_i \sin \alpha_i)\frac{d_t}{2} + (T_i - k_i \Delta y \cos \alpha_i \sin \alpha_i)\frac{d_t}{2} = -k_i d_t \cos \alpha_i \sin \alpha_i \Delta y, && (\circlearrowleft)
\end{aligned}
\tag{5.1}
$$

where:

α_i	=	Angle of inclination	[degree],
T_i	=	Pretension force in the inclined cable	[N],
T_v	=	Pretension force in the vertical cable	[N],
F_{NB}	=	Net buoyancy force	[N],
k_i	=	Stiffness in the inclined cable	[N · m^{-1}],
d_t	=	Diameter of the tunnel cross section	[m].

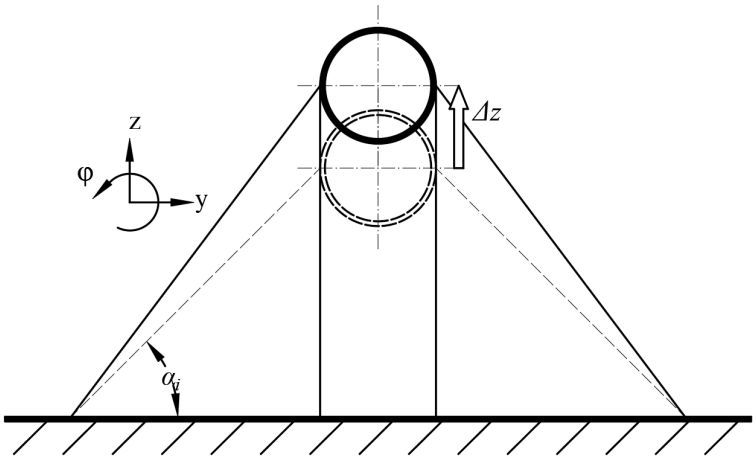

Figure 5.3: Action of the vertical degree of freedom

In Figure 5.3, the tunnel cross section moves vertically with a displacement of Δz. The displacement is symmetric so it makes no contribution to the horizontal and rotational reaction force. Therefore, the following relations hold:

$$\begin{aligned} F_{yz} &= 0, \\ F_{zz} &= (2k_i \sin^2 \alpha_i + 2k_v)\Delta_z, \quad (\downarrow) \\ F_{\varphi z} &= 0, \end{aligned} \tag{5.2}$$

where:

α_i	=	Angle of inclination	[degree],
k_i	=	Stiffness in the inclined cable	$[\mathrm{N} \cdot \mathrm{m}^{-1}]$.

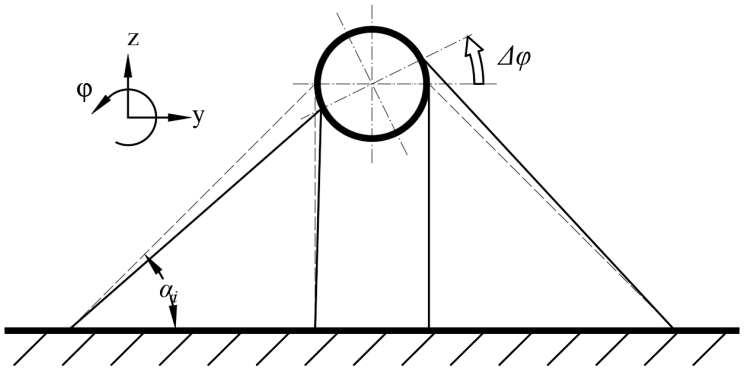

Figure 5.4: Action of the rotational degree of freedom

Similar with the previous cases, the rotation $\Delta\varphi$ in the tunnel cross section is considered small in Figure 5.4. Neglecting the contribution of the vertical line to the horizontal restoring force and the change of the angle of inclination, the following relations hold:

$$\begin{aligned} F_{y\varphi} &= (T_i - k_i \sin\Delta\varphi \frac{d_t}{2} \sin\alpha_i)\cos\alpha_i - (T_i + k_i \sin\Delta\varphi \frac{d_t}{2} \sin\alpha_i)\cos\alpha_i = -k_i d_t \sin\alpha_i \cos\alpha_i \Delta\varphi, \quad (\leftarrow) \\ F_{z\varphi} &= 0, \\ F_{\varphi\varphi} &= -(T_i - k_i \sin\Delta\varphi \frac{d_t}{2} \sin\alpha_i)\sin\alpha_i \frac{d_t}{2} + (T_i + k_i \sin\Delta\varphi \frac{d_t}{2} \sin\alpha_i)\sin\alpha_i \frac{d_t}{2} - (T_v - k_v \sin\Delta\varphi \frac{d_t}{2})\frac{d_t}{2} + (T_v + k_v \sin\Delta\varphi \frac{d_t}{2})\frac{d_t}{2} \\ &= (k_i \sin^2 \alpha_i + k_v)\frac{d_t^2}{2}\Delta\varphi, \quad (\circlearrowleft) \end{aligned} \tag{5.3}$$

where:

α_i	=	Angle of inclination	[degree],
T_i	=	Pretension force in the inclined cable	[N],
T_v	=	Pretension force in the vertical cable	[N],
k_i	=	Stiffness in the inclined cable	$[\mathrm{N} \cdot \mathrm{m}^{-1}]$,
k_v	=	Stiffness in the vertical cable	$[\mathrm{N} \cdot \mathrm{m}^{-1}]$,
d_t	=	Diameter of the tunnel cross section	[m].

Summation of the Equation 5.1, Equation 5.2 and Equation 5.3 yields the total reaction force dependent on the three degrees of freedom:

$$
\begin{aligned}
F_y &= 2k_i \cos^2\alpha_i \Delta y - k_i d_t \sin\alpha_i \cos\alpha_i \Delta\varphi, && (\leftarrow)\\
F_z &= (2k_i \sin^2\alpha_i + 2k_v)\Delta_z, && (\downarrow)\\
F_\varphi &= -k_i d_t \cos\alpha_i \sin\alpha_i \Delta y + (k_i \sin^2\alpha_i + k_v)\frac{d_t^2}{2}\Delta\varphi. && (\circlearrowleft)
\end{aligned}
\tag{5.4}
$$

In matrix form the equations above can be written as:

$$
\mathbf{F} = \begin{bmatrix} 2k_i\cos^2\alpha_i & 0 & -k_i d_t \sin\alpha_i\cos\alpha_i \\ 0 & 2k_i\sin^2\alpha_i + 2k_v & 0 \\ -k_i d_t \cos\alpha_i \sin\alpha_i & 0 & (k_i\sin^2\alpha_i + k_v)\frac{d_t^2}{2} \end{bmatrix} \begin{bmatrix} \Delta y \\ \Delta z \\ \Delta\varphi \end{bmatrix} = \mathbf{K}\cdot\Delta. \tag{5.5}
$$

5.1.2. Nonlinear stiffness model

In the previous linear stiffness case, the derivation of the stiffness matrix is quite straightforward. However, the pretension force is not included in the equations, which means this model can not study the influence of the buoyancy weight ratio (BWR). To solve this problem, a nonlinear stiffness model is developed with the assumption that the change in the angle of inclination is not negligible. The three degrees of freedom are therefore fully coupled with each other. The structure is drawn in the position as shown in Figure 5.5 to solve all three reaction forces together.

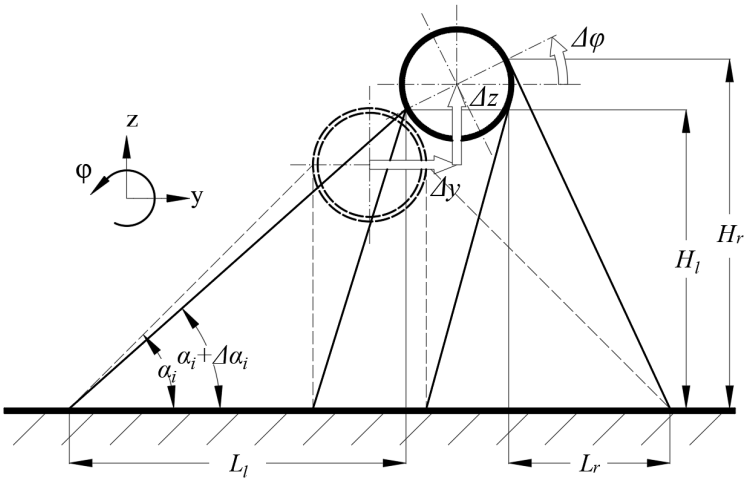

Figure 5.5: Action of the three degrees of freedom

The dimension of L_l, L_r, H_l and H_r in Figure 5.5 is derived as:

$$
\begin{aligned}
L_l &= L_i + \Delta y + \frac{d_t}{2}(1-\cos\Delta\varphi),\\
L_r &= L_i - \Delta y + \frac{d_t}{2}(1-\cos\Delta\varphi),\\
H_l &= h_t + \Delta z - \frac{d_t}{2}\sin\Delta\varphi,\\
H_r &= h_t + \Delta z + \frac{d_t}{2}\sin\Delta\varphi.
\end{aligned}
\tag{5.6}
$$

The length of the deformed cables is determined as:

$$
\begin{aligned}
l_{il} &= \sqrt{L_l^2 + H_l^2}, \\
l_{ir} &= \sqrt{L_r^2 + H_r^2}, \\
l_{vl} &= \sqrt{(L_l - L_i)^2 + H_l^2}, \\
l_{vr} &= \sqrt{(L_r - L_i)^2 + H_r^2}.
\end{aligned} \tag{5.7}
$$

The tension force in the cables is then defined as:

$$
\begin{aligned}
T_{il} &= T_i + k_i(l_{il} - l_i), \\
T_{ir} &= T_i + k_i(l_{ir} - l_i), \\
T_{vl} &= T_v + k_v(l_{vl} - l_v), \\
T_{vr} &= T_v + k_v(l_{vr} - l_v).
\end{aligned} \tag{5.8}
$$

Finally, the reaction force in three degrees of freedom is derived as:

$$
\begin{aligned}
F_y &= T_{il}\frac{L_l}{l_{il}} - T_{ir}\frac{L_r}{l_{ir}} + T_{vl}\frac{L_l - L_i}{l_{vl}} + T_{vr}\frac{L_i - L_r}{l_{vr}}, && (\leftarrow) \\
F_z &= T_{il}\frac{H_l}{l_{il}} + T_{ir}\frac{H_r}{l_{ir}} + T_{vl}\frac{H_l}{l_{vl}} + T_{vr}\frac{H_r}{l_{vr}} - F_{NB}, && (\downarrow) \\
F_\varphi &= \left(T_{il}\frac{L_l}{l_{il}} + T_{ir}\frac{L_r}{l_{ir}} + T_{vl}\frac{L_l - L_i}{l_{vl}} - T_{vr}\frac{L_i - L_r}{l_{vr}}\right)\frac{d_t}{2}\sin\Delta\varphi + \left(-T_{il}\frac{H_l}{l_{il}} + T_{ir}\frac{H_r}{l_{ir}} - T_{vl}\frac{H_l}{l_{vl}} + T_{vr}\frac{H_r}{l_{vr}}\right)\frac{d_t}{2}\cos\Delta\varphi. && (\circlearrowleft)
\end{aligned} \tag{5.9}
$$

It is worth noting that in this nonlinear stiffness model all three degrees of freedom are nonlinearly coupled with each other, so no stiffness matrix can be extracted from the above equations. The behaviour of the linear and nonlinear stiffness model is briefly presented in Appendix A, where it is shown that the main difference between a linear stiffness model and a nonlinear stiffness model lies in the influence of the horizontal displacement on the vertical restoring force.

5.2. Assumptions of the model for anchoring system

Several assumptions are made to model the stiffness of the anchoring system. The validity of these assumptions must be checked in order for the model to be consistent with itself.

Self weight of the cable

The shape of the cable is assumed to be a straight line from the foundation at the bottom to the joint at the top, by ignoring the self weight of the cables. Therefore, there is no sagging in the cable and the direction of the restoring force is considered to be the same with the direction of the cable.

Small angles of rotation

The absolute value of the rotational angle is assumed to be small in the linear stiffness model, whereas nonlinear stiffness model does not have this assumption.

No slackening

It is assumed that no slackening of the anchoring system can be induced by the wave and current loading. This means that compressive stresses can be developed in the cables when the strains are negative values.

Linear elasticity

The material of the anchoring system is assumed to be linear elastic. Only two material parameters need to be experimentally determined: the Young's modulus and the Poisson's ratio. The physical nonlinearity of the anchoring system is therefore not included in this model.

6

Model for submerged floating tunnel

This chapter describes the simplification of the submerged floating tunnel in order to analyze the global dynamic behavior. The tunnel tube is treated as a beam on elastic foundation with deformations in three directions(horizontal, vertical and rotational directions). The governing equations of the tube are derived based on the Hamilton principle considering the non-linear hydraulic excitation as discussed in section 6.1. The assumptions made for modelling the submerged floating tunnel are then discussed in section 6.2.

6.1. Model set-up

This research focuses on the global dynamic response of a SFT, so the influence of discretion of the anchoring system on the dynamic behaviour of the SFT is neglected. The discrete elastic supports are simplified as an equivalent continuous elastic foundation and the tube of the SFT is considered as a beam on elastic foundation model (BOEF) as shown in Figure 6.1.

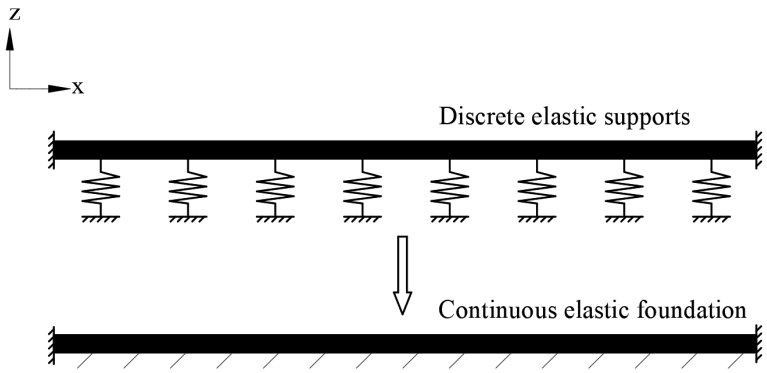

Figure 6.1: Simplification of the SFT tube (front view)

The flow scheme of the submerged floating tunnel model is shown in Figure 6.2. It requires the tunnel parameters, the anchoring system parameters and the loading parameters as input. After performing corresponding substitution of these parameters, the BOEF model and the stiffness model give the structural information and the wave and current model gives the loading information. The governing equations are derived by combining the structural information and the loading information, which are on the left hand side of the equation (LHS) and the right hand side of the equation (RHS), respectively. The governing equations are a set of partial differential equations (PDEs) with respect to space and time. These PDEs can be converted to a set of ordinary differential equations (ODEs) by performing the modal analysis. This set of ODEs can be solved by applying the MATLAB® function ode45 which is based on an explicit Runge-Kutta formula (Dormand and Prince, 1980; Shampine and Reichelt, 1997). The output of the model contains the natural frequencies, the mode shapes, and the time history of the responses.

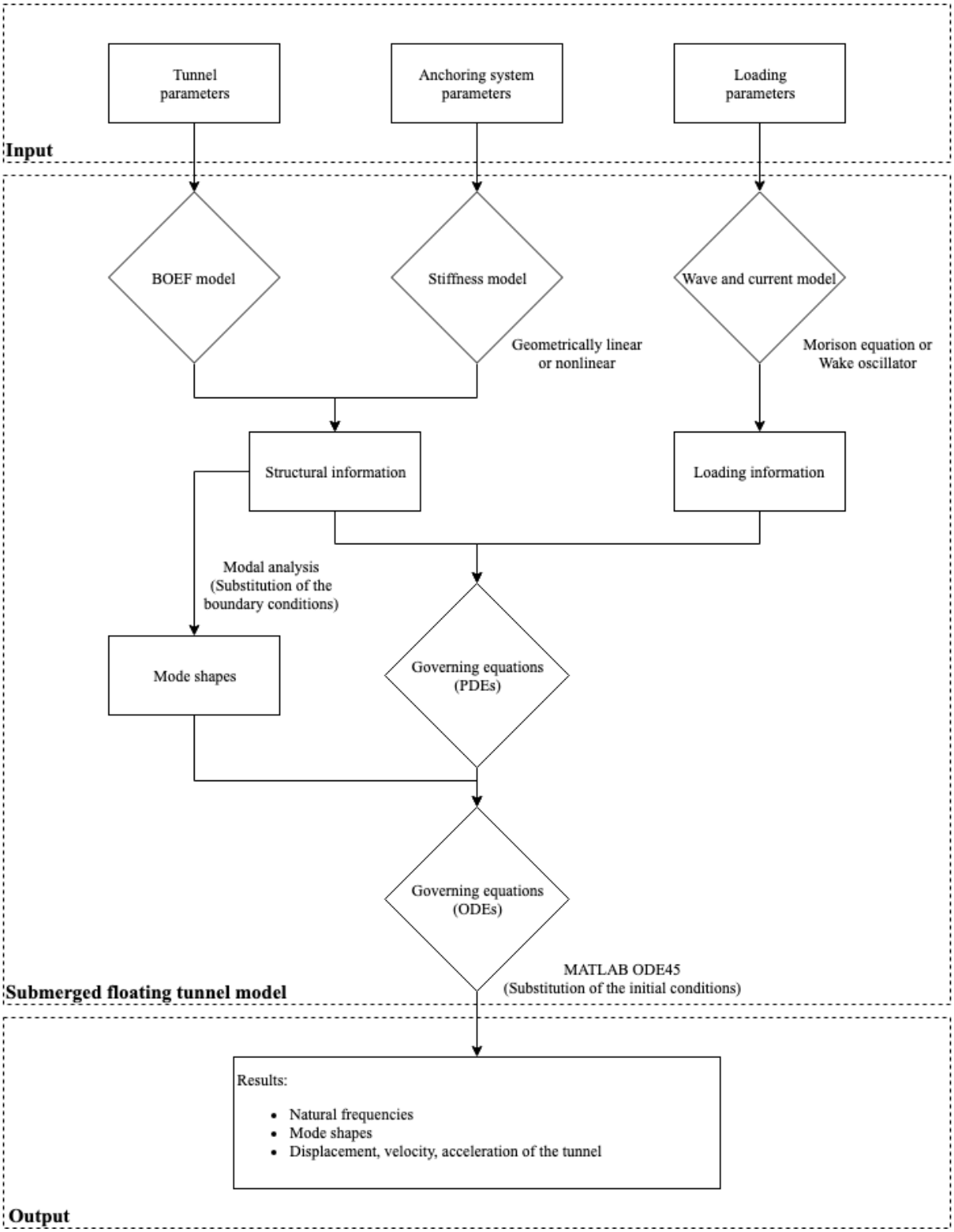

Figure 6.2: Set-up of the submerged floating tunnel model

6.1.1. Governing equations

The governing equations of a submerged floating tunnel are derived based on the Hamilton principle, which states the equations of motion of a physical system is determined by a definite integral involving the kinetic energy, potential energy and the work done by external forces as:

$$\int_{t_1}^{t_2} (\delta W_e + \delta T - \delta V)\, dt = 0, \tag{6.1}$$

where:

W_e	=	Work done by the external forces	[N · m],
T	=	Kinetic energy	[N · m],
V	=	Potential energy	[N · m].

The notation δ indicates a variation in the system, i.e. an imaginary change of configuration that satisfies the system constraints.

The total kinetic energy of the beam can be written as:

$$T = \int_0^L \left(\frac{1}{2} m_t \dot{y}^2 + \frac{1}{2} m_t \dot{z}^2 + \frac{1}{2} m_t r_g^2 \dot{\varphi}^2 \right) dx, \tag{6.2}$$

where:

m_t	=	Mass of the tunnel per unit length	[kg · m^{-1}],
r_g	=	Radius of gyration of the tunnel cross section	[m].

The equation is composed of three motion components, horizontal movement in y direction, vertical movement in z direction and rotational movement in φ direction. The sign convention is the same with the one stated in the previous chapter.

The total potential energy is given by the summation of the strain energy due to the bending and torsional deformation of the tube and the elastic potential energy of the anchoring system, with the latter expressed in the form of the work done by the restoring forces:

$$V = \int_0^L \left(\frac{1}{2} EI_t y''^2 + \frac{1}{2} EI_t z''^2 + \frac{1}{2} GI_p \varphi'^2 \right) dx + \int_0^L \left(\int_0^y F_y dy + \int_0^z F_z dz + \int_0^\varphi F_\varphi d\varphi \right) dx, \tag{6.3}$$

where:

EI_t	=	Bending stiffness of the SFT tube	[N·m^2],
GI_p	=	Torsional stiffness of the SFT tube	[N · m ·rad^{-1}],
F_y	=	Restoring force in horizontal direction	[N],
F_z	=	Restoring force in vertical direction	[N],
F_φ	=	Restoring moment in rotational direction	[N·m].

External force work includes the work done by the external fluid force and the structure damping force due to viscous damping:

$$W_e = \int_0^L \left(-c_y \dot{y} y - c_z \dot{z} z - c_\varphi \dot{\varphi} + F_{ey} y + F_{ez} z \right) dx, \tag{6.4}$$

where:

c_y	=	Structural damping coefficient in horizontal motion	[N · s· m^{-1}],
c_z	=	Structural damping coefficient in vertical motion	[N · s· m^{-1}],
c_φ	=	Structural damping coefficient in rotational motion	[N · s· m^{-1}],
F_{ey}	=	External fluid force in horizontal direction	[N],
F_{ez}	=	External fluid force in vertical direction	[N].

The governing equations of motion can be obtained by substituting Equation 6.2, Equation 6.3 and Equation 6.4 into Equation 6.1 as shown in Equation 6.5:

$$\begin{cases} EI_t y'''' + m_t \ddot{y} + c_y \dot{y} + F_y = F_{ey} \\ EI_t z'''' + m_t \ddot{z} + c_z \dot{z} + F_z = F_{ez} \\ GI_p \varphi'' + I_0 \ddot{\varphi} + c_\varphi \dot{\varphi} + F_\varphi = 0 \end{cases}, \tag{6.5}$$

In fact, Equation 6.5 represents several governing equations with different stiffness models and different hydraulic loading conditions, i.e. different restoring forces (F_y, F_z and F_φ) and different external hydraulic forces (F_{ey} and F_{ez}). After performing the necessary substitutions, the governing equations regarding to different scenarios are finally given as:

- **Model A:** linear stiffness model and Morison equation:

$$\begin{cases} EI_t y'''' + (m_t + m_a)\ddot{y} + c_y \dot{y} + k_{yy} y + k_{y\varphi} \varphi = \frac{1}{2}\rho_w D C_d (u_y - \dot{y}) \sqrt{(u_y - \dot{y})^2 + (u_z - \dot{z})^2} + (C_a + 1)\frac{\pi}{4}\rho_w D^2 \dot{u}_y \\ EI_t z'''' + (m_t + m_a)\ddot{z} + c_z \dot{z} + k_{zz} z = \frac{1}{2}\rho_w D C_d (u_z - \dot{z}) \sqrt{(u_y - \dot{y})^2 + (u_z - \dot{z})^2} + (C_a + 1)\frac{\pi}{4}\rho_w D^2 \dot{u}_z \\ GI_p \varphi'' + I_0 \ddot{\varphi} + c_\varphi \dot{\varphi} + k_{\varphi y} y + k_{\varphi\varphi} \varphi = 0 \end{cases}, \tag{6.6}$$

- **Model B:** nonlinear stiffness model and Morison equation:

$$\begin{cases} EI_t y'''' + (m_t + m_a)\ddot{y} + c_y \dot{y} + F_y(y,z,\varphi) = \frac{1}{2}\rho_w D C_d (u_y - \dot{y}) \sqrt{(u_y - \dot{y})^2 + (u_z - \dot{z})^2} + (C_a + 1)\frac{\pi}{4}\rho_w D^2 \dot{u}_y \\ EI_t z'''' + (m_t + m_a)\ddot{z} + c_z \dot{z} + F_z(y,z,\varphi) = \frac{1}{2}\rho_w D C_d (u_z - \dot{z}) \sqrt{(u_y - \dot{y})^2 + (u_z - \dot{z})^2} + (C_a + 1)\frac{\pi}{4}\rho_w D^2 \dot{u}_z \\ GI_p \varphi'' + I_0 \ddot{\varphi} + c_\varphi \dot{\varphi} + F_\varphi(y,z,\varphi) = 0 \end{cases}, \tag{6.7}$$

- **Model C:** nonlinear stiffness model and simplified wake oscillator model:

$$\begin{cases} EI_t y'''' + (m_t + m_a)\ddot{y} + c_y \dot{y} + F_y(y,z,\varphi) = \frac{1}{2}\rho D L u_y^2 (C_d + \frac{1}{2} C_l q \frac{\dot{z}}{u_y - \dot{y}}) \\ EI_t z'''' + (m_t + m_a)\ddot{z} + c_z \dot{z} + F_z(y,z,\varphi) = \frac{1}{2}\rho D L u_y^2 (-C_d \frac{\dot{z}}{u_y - \dot{y}} + \frac{1}{2} C_l q) \\ GI_p \varphi'' + I_0 \ddot{\varphi} + c_\varphi \dot{\varphi} + F_\varphi(y,z,\varphi) = 0 \\ \ddot{q} + \epsilon \omega_s (q^2 - 1)\dot{q} + \omega_s^2 q = \frac{A}{D}\ddot{z} \end{cases}, \tag{6.8}$$

- **Model D:** nonlinear stiffness model and non-simplified wake oscillator model:

$$\begin{cases} EI_t y'''' + (m_t + m_a)\ddot{y} + c_y\dot{y} + F_y(y,z,\varphi) = \dfrac{1}{2}\rho D L u_y^2 \left(C_{D0}(u_y - \dot{y}) + \dfrac{1}{2} C_{L0} q \dot{z} \right) \dfrac{\sqrt{(u_y - \dot{y})^2 + \dot{z}^2}}{u_y^2} \\ EI_t z'''' + (m_t + m_a)\ddot{z} + c_z\dot{z} + F_z(y,z,\varphi) = \dfrac{1}{2}\rho D L u_y^2 \left(-C_{D0}\dot{z} + \dfrac{1}{2} C_{L0} q (u_y - \dot{y}) \right) \dfrac{\sqrt{(u_y - \dot{y})^2 + \dot{z}^2}}{u_y^2} \\ GI_p\varphi'' + I_0\ddot{\varphi} + c_\varphi\dot{\varphi} + F_\varphi(y,z,\varphi) = 0 \\ \ddot{q} + \epsilon\omega_s(q^2 - 1)\dot{q} + \omega_s^2 q = \dfrac{A}{D}\ddot{z} \end{cases} . \tag{6.9}$$

These four sets of governing equations are very important in this research and is denoted as **Model A**, **Model B**, **Model C** and **Model D** hereinafter. The left hand sides of the equations (LHS) reveal the information of the structure while the right hand sides (RHS) of the equations imply the loading condition. The difference between **Model A** and **Model B** is at the LHS, where the stiffness is derived based on different assumptions. The difference between **Model C** and **Model D** is at the RHS, where the complicacy of the wake oscillator is different.

6.2. Assumptions of the model for submerged floating tunnel

Next to the assumptions made to model the anchoring system, several assumptions have been made in order to model the SFT. The validity of these assumptions must be checked in order for the model to be consistent with itself.

Euler-Bernoulli beam

The SFT is modeled with Euler-Bernoulli beam, which means that shear deformations are neglected in this model. Furthermore, the longitudinal behaviour of the tunnel is not included.

Connections

The connections between the anchoring cables and the tunnel are modeled with a hinge joint. The translational connection is assumed to be rigid and the rotational connection is assumed to be free.

Cross-section

The cross section of the tunnel is assumed to be uniform in axial direction. The hollow cross section of the tunnel is considered as an equivalent solid cross section with the same physical and geometrical properties.

Structural damping

The structural damping due to viscous damping is assumed to be considerably small compared with the hydrodynamic damping and is neglected for further calculation.

Small structure velocity

In **Model C**, it is assumed that velocity of the structure should be considerably small compared with the current velocity.

III

Case study

7

Scaled SFT model

This chapter describes a test of a scaled SFT model hold by TIWTE (Tianjin Research Institute For Water Transport Engineering) in Tianjin, China. This test will be used as a case study in this research. The Physical and geometrical parameters of the scaled SFT model are described in section 7.2 and the load cases are introduced in section 7.3

7.1. Test Overview

In 2018, the 20th annual meeting of CAST (China Association for Science and Technology) listed submerged floating tunnel engineering technology as one of the 60 major scientific and engineering problems in 12 fields. In February 2018, after the handover of the Hong Kong-Zhuhai-Macao Bridge Island Tunnel Project, the China Communications Construction Company Limited SFT Technical Joint Research Team was established. Leading by the Island and tunnel project general management office of China Communications Construction Company Limited (CCCC), Tunnel Engineering Consultants & Delft University of Technology (TEC & TU Delft), Tianjin Research Institute for Water Transport Engineering, M.O.T.(TIWTE), China Communications Highway Planning and Design Institute Co., Ltd. (HPDI), China Communications Third Navigation Engineering Co., Ltd. (THEC), China Communications Fourth Habour Engineering Investigation and Design Institute Co., Ltd. (FHDI) participated in and signed a cooperation agreement to formally and systematically carry out research on SFT technology.

In 2019, a test aiming to observe the dynamic behaviour of the SFT system under current and waves is carried out in Tianjin by TIWTE. The emphasis of this test is not getting parameters for design but studying how the dynamic response of a SFT is influenced by different geometrical and structural design parameters, such as BWR, stiffness of the anchoring system, boundary conditions of the SFT, etc.

7.2. Physical and geometrical parameters

The physical model of the test is scaled by a factor of $\lambda = 1/50$. The Froude number Fn is used to scale the parameters of the fluid to ensure the gravity forces are correctly scaled:

$$Fn = \frac{U}{\sqrt{gL}}, \tag{7.1}$$

where:

U	=	Flow velocity	[m·s^{-1}],
g	=	Gravitational acceleration	[m·s^{-2}],
L	=	Characteristic length	[m].

Given that surface waves are gravity-driven, equility in Fn ensures that wave resistance and other wave forces are also correctly scaled. The Froude scaling is shown in Table 7.1. The subscripts M and F are for Model scale and Full scale, respectively.

Physical Parameter	Relation	Unit
Length	$l_M = \lambda l_F$	[m]
Time	$t_M = \sqrt{\lambda}\, t_F$	[s]
Structural mass	$m_M = \lambda^3 \frac{\rho_M}{\rho_F} m_F$	[kg]
Velocity	$v_M = \sqrt{\lambda}\, v_F$	[m·s^{-1}]
Acceleration	$a_M = a_F$	[m·s^{-2}]
Force	$F_M = \lambda^3 \frac{\rho_M}{\rho_F} F_F$	[N]
Moment	$M_M = \lambda^4 \frac{\rho_M}{\rho_F} M_F$	[N · m]

Table 7.1: Froude scaling

7.2.1. Basin

The scaled SFT model is placed in a 30m × 50m basin to simulate the ocean environment with no boundaries, so the size of the basin is not scaled from a full scale value. The physical and geometrical parameters of the basin is listed in Table 7.2. The length and the width of the full scale water area are not related to the model scale ones and are denoted by the slash symbol.

Item	Symbol	Full scale value	Model scale value	Unit
Length	l_b	/	50	[m]
Width	w_b	/	30	[m]
Water Depth	h_w	90	1.8	[m]
Water Density	ρ_w	1000	1000	[kg·m^{-3}]
Gravitational acceleration	g	9.83	9.83	[m·s^{-2}]

Table 7.2: Physical and geometrical parameters of the basin

7.2.2. Tunnel

The full scale structure is a single deck concrete tunnel with two-lane road. The tunnel is 1200m long with a outer diameter of 12.50m and a inner diameter of 10.50m. Neglecting the contribution of the interior wall and the pavement layer to the bending stiffness, the tunnel cross-section can be simplified as a circular hollow section as shown in Figure 7.1.

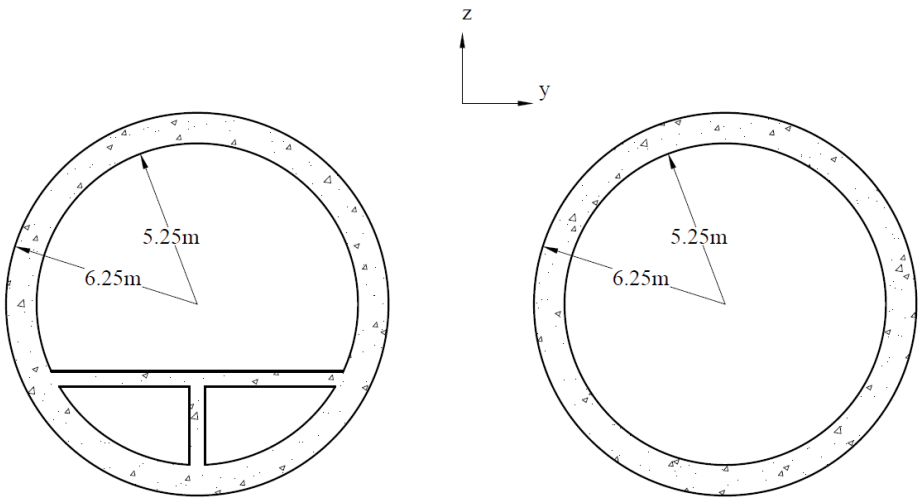

Figure 7.1: Simplification of the tunnel cross-section

The full scale tunnel is simulated by a steel bar surrounded by buoyancy foam with discrete mass rings as shown in Figure 7.2. The steel bar and the buoyancy foam (Figure 7.2, section A-A) provide the corresponding

bending stiffness and buoyant force, respectively. The discrete mass rings (Figure 7.2, section B-B) are applied to obtain the corresponding mass, which is determined by the buoyancy weight ratio.

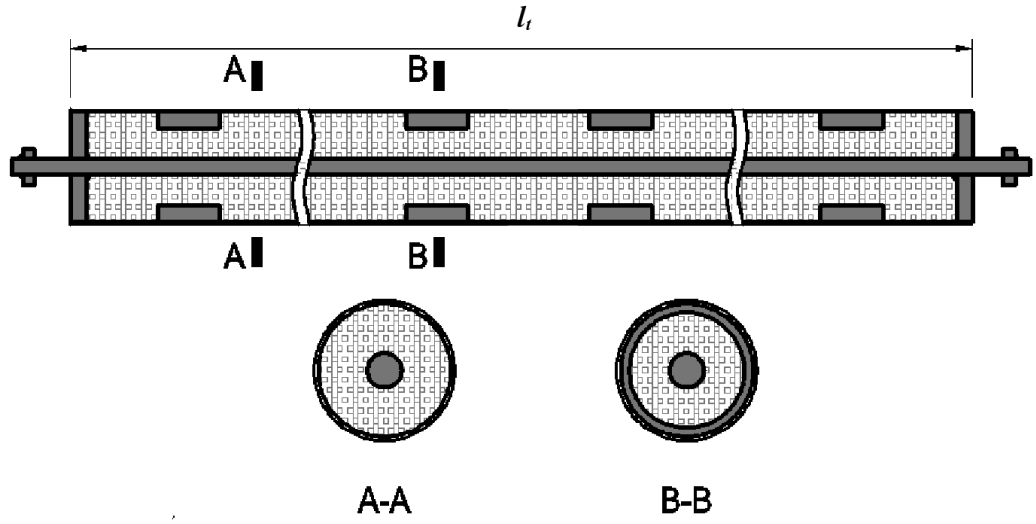

Figure 7.2: The composition of the scaled tunnel model

The physical and geometrical parameters of the tunnel are listed in Table 7.3. Note that there is no value for the Young's modulus and the second moment of area of the tunnel for the scaled model since they are included in the bending stiffness.

Item	Symbol	Full scale value	Model scale value	Unit
Length	l_t	1200	24	[m]
Diameter	d_t	12.5	0.25	[m]
Equivalent density	ρ_t	162.97	852.56	[kg·m^{-3}]
Mass per unit length	m_t	20000	41.85	[kg·m^{-1}]
Buoyancy weight ratio	BWR	1.19	1.19	[1]
Young's modulus	E_c	3.60×10^{10}	/	[N·m^{-2}]
Second moment of area	I_t	683.30	/	[m^4]
Bending stiffness	EI_t	2.22×10^{13}	71200	[N·m^2]

Table 7.3: Physical and geometrical parameters of the tunnel cross-section

7.2.3. Anchoring system

The configuration of the anchoring system is shown in Figure 7.3 and Figure 7.4.

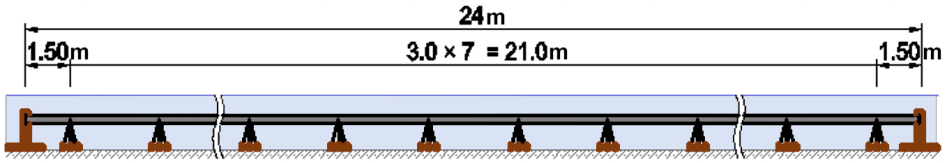

Figure 7.3: Front view of the anchoring system configuration

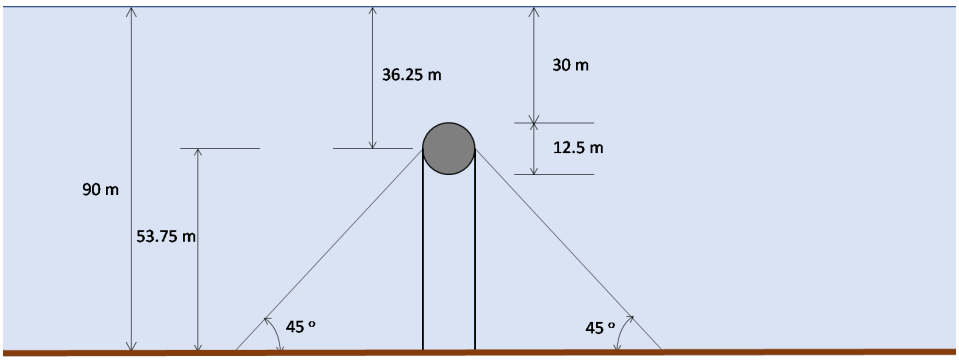

(a) Side view of the full scale structure

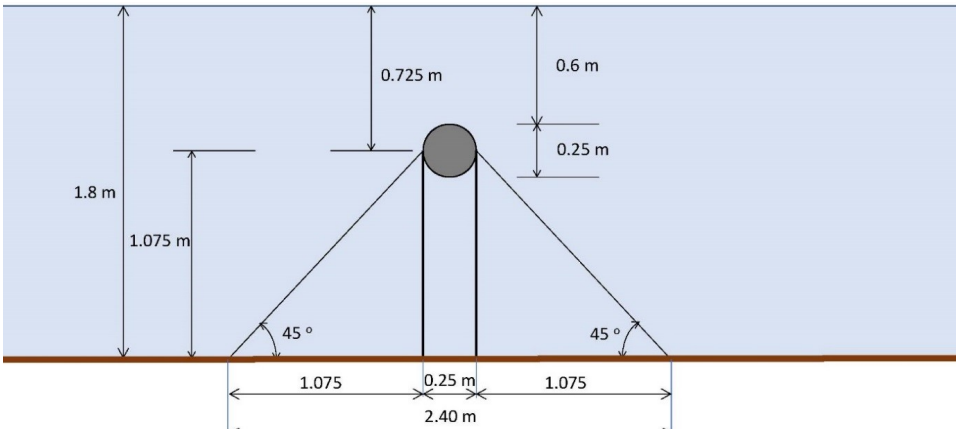

(b) Side view of the scaled model

Figure 7.4: Side view of the anchoring system configuration

The physical and geometrical parameters of the anchoring system are listed in Table 7.4. The vertical cables and the inclined cables have the same diameter of 0.008 m in model scale, while the material of the vertical cables are stiffer than the inclined cables.

	Item	Symbol	Full scale value	Model scale value	Unit
Vertical cables	Length	l_v	53.75	1.075	[m]
	Diameter	d_v	0.4	0.008	[m]
	Young's Modulus	E_v	2.00×10^{11}	2.00×10^{11}	[N·m^{-2}]
	Axial stiffness	k_v	4.68×10^{8}	9.35×10^{6}	[N · m^{-1}]
	Density	ρ_v	7850	7850	[kg·m^{-3}]
	Spacing	s_v	150	3	[m]
Inclined cables	Inclined angle	α_i	45	45	[degree]
	Length	l_i	76	1.52	[m]
	Diameter	d_i	0.4	0.008	[m]
	Young's Modulus	E_i	3.21×10^{8}	3.21×10^{8}	[N·m^{-2}]
	Axial stiffness	k_i	5.30×10^{5}	1.06×10^{4}	[N · m^{-1}]
	Density	ρ_i	7850	7850	[kg·m^{-3}]
	Spacing	s_i	150	3	[m]

Table 7.4: Physical and geometrical parameters of the anchoring system

7.3. Load cases

This test focuses on the dynamic behavior of the SFT under different load cases, i.e. different combined wave and current loads with different attack angles. Three groups of these load cases are considered in this report, regarding to combined wave and current loading cases, oblique wave loading cases and vortex induced vibration cases.

The first group contains three load cases with different wave heights and current speeds. For comparison, the first two groups share the same wave input and the last two groups share the same current input. The most severe case is the third one where both wave and current inputs are the largest value. Moreover, the load direction is perpendicular to the tunnel axis and all the other load inputs are the same. These load cases are shown in Table 7.5.

	Item	Symbol	Full scale value	Model value	Unit
Load case 1.1	Wave height	H_w	5	0.1	[m]
	Wave period	T_w	14.2	2	[s]
	Current speed	V_c	0.71	0.1	[m· s^{-1}]
	Attack angle	α_w	90	90	[degree]
Load case 1.2	Wave height	H_w	5	0.1	[m]
	Wave period	T_w	14.2	2	[s]
	Current speed	V_c	1.41	0.2	[m· s^{-1}]
	Attack angle	α_w	90	90	[degree]
Load case 1.3	Wave height	H_w	10	0.2	[m]
	Wave period	T_w	14.2	2	[s]
	Current speed	V_c	1.41	0.2	[m· s^{-1}]
	Attack angle	α_w	90	90	[degree]

Table 7.5: Information about load group 1

The second group is about the oblique wave, which means the wave load is applied at different attack angles. The attack angle is defined as the angle between the tunnel axis and the flow line as shown in Figure 7.5. Three attack angle is considered, i.e. 90°, 60° and 45°. Among these cases, the wave height and the wave period are set unchanged which is 0.1m and 2s, respectively, whereas the current speed is set to 0.

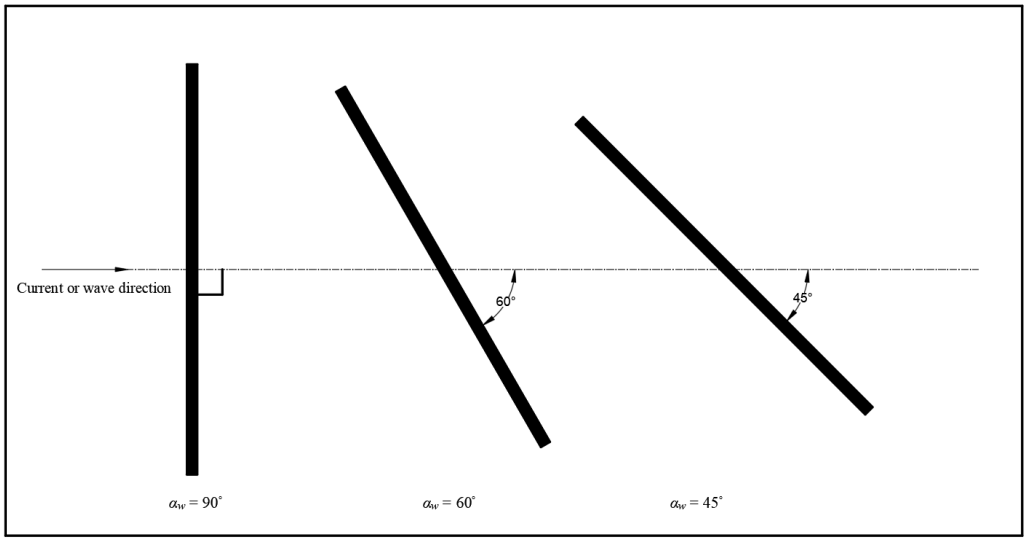

Figure 7.5: Attack angle of 90°, 60° and 45°

To capture the wave propagating along the tunnel from bow to stern when the loading direction is not perpendicular to the tunnel, Equation 4.1 is modified with a Heaviside function denoted by H as:

$$\begin{cases} u_y(x,t) = \omega a \dfrac{\cosh(k(d+z))}{\sinh(kd)} \sin(\omega(t - \dfrac{x\cos\alpha_w}{u_w})) \cdot H(t - \dfrac{x\cos\alpha_w}{u_w}) \cdot \sin\alpha_w \\ u_z(x,t) = \omega a \dfrac{\sinh(k(d+z))}{\sinh(kd)} \cos(\omega(t - \dfrac{x\cos\alpha_w}{u_w})) \cdot H(t - \dfrac{x\cos\alpha_w}{u_w}) \end{cases}, \tag{7.2}$$

where:

ω	=	Wave frequency	[rad $\cdot s^{-1}$],
a	=	Wave amplitude	[m],
k	=	Wave number	[m^{-1}],
d	=	Water depth	[m],
α_w	=	Attack angle	[degree],
u_w	=	Wave phase velocity	[m$\cdot$ s^{-1}].

Therefore, u_y and u_z are functions of both x and t. When the attack angle $\alpha_w = 90°$, the equation is the same with Equation 4.1. The information about load group 2 are shown in Table 7.6.

	Item	Symbol	Full scale value	Model value	Unit
Load case 2.1	Wave height	H_w	5	0.1	[m]
	Wave period	T_w	14.2	2	[s]
	Current speed	V_c	0	0	[m$\cdot$ s^{-1}]
	Attack angle	α_w	90	90	[degree]
Load case 2.2	Wave height	H_w	5	0.1	[m]
	Wave period	T_w	14.2	2	[s]
	Current speed	V_c	0	0	[m$\cdot$ s^{-1}]
	Attack angle	α_w	60	60	[degree]
Load case 2.3	Wave height	H_w	5	0.1	[m]
	Wave period	T_w	14.2	2	[s]
	Current speed	V_c	0	0	[m$\cdot$ s^{-1}]
	Attack angle	α_w	45	45	[degree]

Table 7.6: Information about load group 2

The third group focuses on the vortex induced vibration. Only current loading is considered is this group. The current is speed is set to to $V_c = 1.5\text{m}\cdot\text{s}^{-1}$ for load case 3.1 and $V_c = 1.0\text{m}\cdot\text{s}^{-1}$ for load case 3.2. The The information about load group 3 are shown in Table 7.7.

	Item	Symbol	Full scale value	Model value	Unit
Load case 3.1	Wave height	H_w	0	0	[m]
	Wave period	T_w	/	/	[s]
	Current speed	V_c	10.6	1.5	[m$\cdot$ s^{-1}]
	Attack angle	α_w	90	90	[degree]
Load case 3.2	Wave height	H_w	0	0	[m]
	Wave period	T_w	/	/	[s]
	Current speed	V_c	7.1	1.0	[m$\cdot$ s^{-1}]
	Attack angle	α_w	90	90	[degree]

Table 7.7: Information about load group 3

8

Results of the scaled SFT model

This chapter presents and explains the results of the scaled SFT model based on **Model A**, **Model B**, **Model C** and **Model D**. First, a frequency extraction based on **Model A** is discussed to understand the system behaviour in further analysis. Second, the results of the scaled SFT model based on **Model A** and **Model B**, regarding the first two load groups are discussed. Subsequently, discussions in terms of the effect of the geometrical nonlinearity and the effect of the global analysis is presented in section 8.4 and section 8.5. Third, the results of the scaled SFT model based on **Model C** and **Model D**, regarding the third load group is addressed. Finally, the assumptions made to model the scaled SFT model are discussed to check the consistency of the model. All the values of the results can be scaled to the full scale value by means of the Froude scaling shown in Table 7.1. The knowledge obtained in this chapter is applied in the parametric study presented in the next chapter.

Although the results in this chapter are given by global analysis, the results at midspan plotted in 2D is chosen to be discussed for a clear interpretation of the structural behaviour. To have a global view of these results, refer to Appendix B.

8.1. Frequency extraction

The natural frequencies of the system are very essential for understanding the system behaviour, so a frequency extraction was first carried out for further analysis. They were extracted from the response of the initial-value problem of the governing equations of free vibration based on the linear stiffness assumption as:

$$\begin{cases} EI_t y'''' + (m_t + m_a)\ddot{y} + k_{yy}y + k_{y\varphi}\varphi = \dfrac{1}{2}\rho_w D C_d \dot{y}\sqrt{\dot{y}^2 + \dot{z}^2} \\ EI_t z'''' + (m_t + m_a)\ddot{z} + k_{zz}z = \dfrac{1}{2}\rho_w D C_d \dot{z}\sqrt{\dot{y}^2 + \dot{z}^2} \\ GI_p \varphi'' + I_0\ddot{\varphi} + k_{\varphi y}y + k_{\varphi\varphi}\varphi = 0 \end{cases} . \tag{8.1}$$

In fact, this equation is **Model A** (Equation 6.6) in free vibration with substitution of $u_y = 0$, $u_z = 0$, $\dot{u}_y = 0$ and $\dot{u}_z = 0$. The structural damping is ignored compared with the relatively large hydrodynamic damping. The motions in y-direction and φ-direction are coupled together by the stiffness, so the same frequencies for both y-direction and φ-direction are expected. On the contrary, motion in z-direction has its own set of natural frequencies.

Equation 8.1 were solved numerically by using MATLAB® ode45. The natural frequencies were then revealed by performing the Fourier transform to the solution. The natural frequencies of the first ten modes in y-direction and φ-direction and the first ten modes in z-direction are shown in Table 8.1. For comparison, analytical solutions for natural frequencies in y-direction ($\omega_{n,y}$) and natural frequencies in z-direction ($\omega_{n,y}$) were also calculated by:

$$\omega_{n,y} = \sqrt{\frac{EI_t\beta_n^4 + k_{yy}}{m_t + m_a}}, \quad \omega_{n,z} = \sqrt{\frac{EI_t\beta_n^4 + k_{zz}}{m_t + m_a}}, \tag{8.2}$$

where:

$$\beta_n = \frac{n\pi}{l_t} \quad [\mathrm{m}^{-1}],$$
$$l_t = \text{Length of the tunnel} \quad [\mathrm{m}].$$

The added fluid mass is included in the analytical solutions but the nonlinear hydrodynamic damping and the coupling between motions in y-direction and φ-direction are left out.

Mode number	Natural frequency [Hz] (y-direction and φ-direction)		Natural frequency [Hz] (z-direction)	
	Numerical solution	Analytical solution	Numerical solution	Analytical solution
1	1.1188	1.6155	41.8197	72.4387
2	1.1386	1.6425	41.8296	72.4393
3	1.2178	1.7546	41.8297	72.4419
4	1.6435	2.0260	41.8395	72.4490
5	2.1880	2.5035	41.8692	72.4640
6	2.9801	3.1938	41.9187	72.4911
7	3.9008	4.0838	41.9880	72.5357
8	5.0295	5.1587	42.1068	72.6042
9	6.2769	6.4079	42.2850	72.7036
10	7.7224	7.8242	42.5226	72.8421

Table 8.1: Natural frequencies extracted from the linear stiffness model

It can be observed that the first three natural frequencies are very close to each other. This is due to the fact that the stiffness is considerably large and dominants the natural frequencies, so that the changing of mode shape does not influence much on the result. This can be seen in the analytical solution of the natural frequencies as shown in Equation 8.2. In addition, the analytical solutions are relatively larger than the numerical solutions, because the hydrodynamic damping is not included in the analytical solutions. The influence of the hydrodynamic damping becomes smaller as the mode number increases, as the curves of both solutions approach to each other as shown in Figure 8.1.

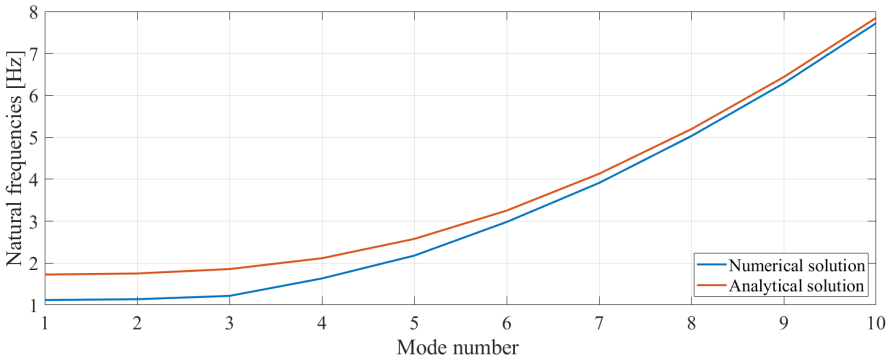

Figure 8.1: Comparison of natural frequencies in y-direction and φ-direction between numerical solutions and analytical solutions

8.2. Combined wave and current loading of the SFT

As it has presented in chapter 7, the first group of the load cases focus on the combined wave and current loading. For comparison,the first two load cases share the same wave input and the last two load cases share the same current input. To understand the influence of both linear and nonlinear stiffness assumptions, **Model A** (Equation 6.6) and **Model B** (Equation 6.7) were applied to solve the displacement in three directions at midspan of the tunnel. The structural damping was not included, given that this study focuses on the influence of the hydraulic damping and the structural damping is considerably small.

8.2.1. Load case 1.1

For load cases 1.1, the loading input wave height, wave period and current speed is set as $H_w = 0.1\text{m}$, $T_w = 2\text{s}$ and $V_c = 0.1\text{m}\cdot\text{s}^{-1}$, respectively. Generally, the displacement in y-direction and φ-direction based on linear and nonlinear stiffness assumption has very similar path as shown in Figure 8.2 and Figure 8.4. However, when it comes to z-direction in Figure 8.3, the displacements have significant difference, which adds evidence to the fact that with the nonlinear stiffness assumption the motions in three directions are all coupled together. The large downward displacement based on the nonlinear stiffness assumption can be addressed to the pendulum effect (described in section 2.3): horizontal displacements are so large that second order effects become relevant and a down-pulling mechanism takes place. This phenomenon can also be observed in other load cases as long as the geometrical nonlinearity is considered.

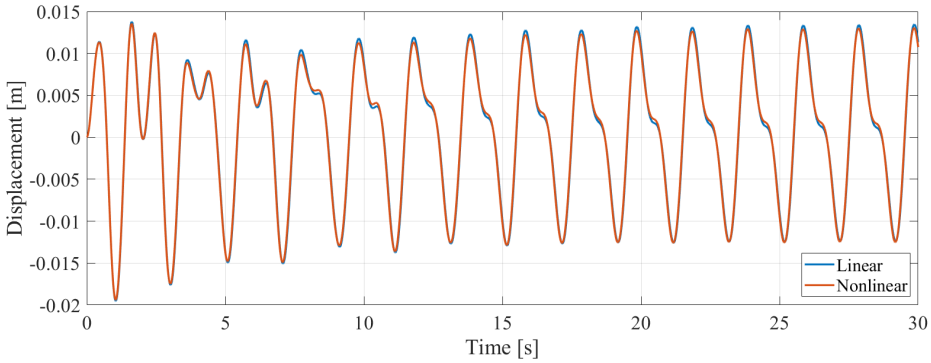

Figure 8.2: Displacement in y direction at midspan (Load case 1.1)

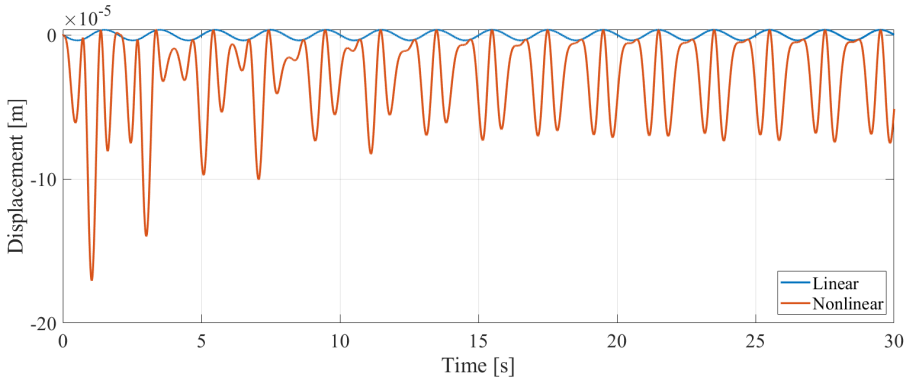

Figure 8.3: Displacement in z direction at midspan (Load case 1.1)

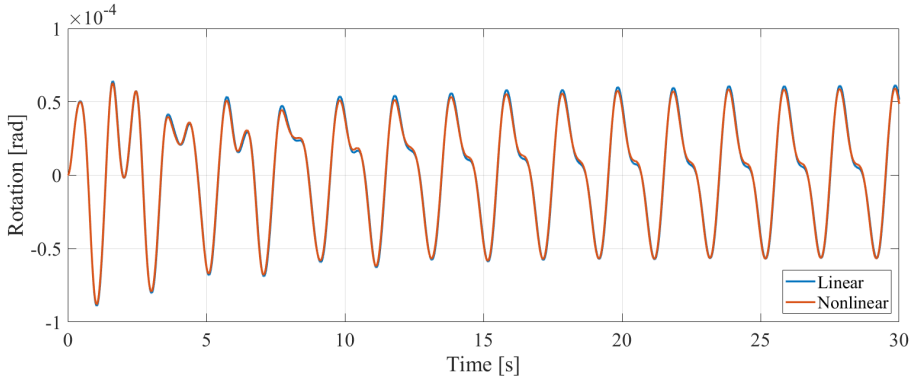

Figure 8.4: Rotation in φ direction at midspan (Load case 1.1)

8.2.2. Load case 1.2

For load cases 1.2, all the loading input except the current speed remains the same. The current speed is increased to $0.2\text{m}\cdot\text{s}^{-1}$, which gives $H_w = 0.1\text{m}$, $T_w = 2\text{s}$ and $V_c = 0.2\text{m}\cdot\text{s}^{-1}$. The increasing of the current speed does not make a huge influence on the amplitude of the response. However, the shape of the signal at steady state becomes more sinusoidal as shown in Figure 8.6. As the increase of the current speed, the combined wave and current loading becomes more static. Therefore, the relatively high frequency components are suppressed.

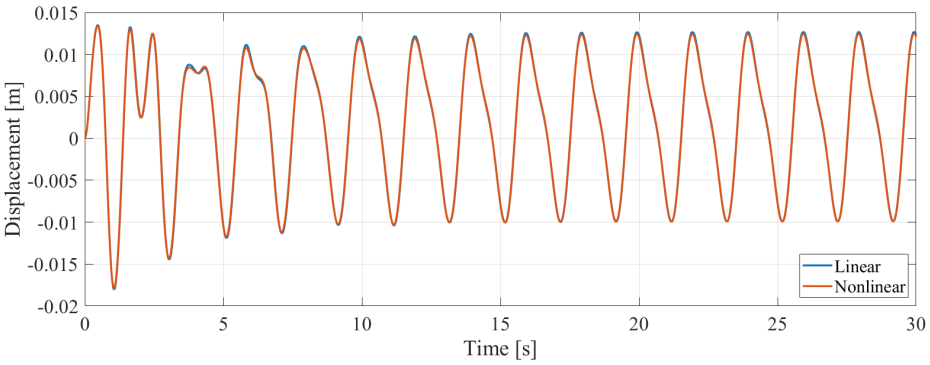

Figure 8.5: Displacement in y direction at midspan (Load case 1.2)

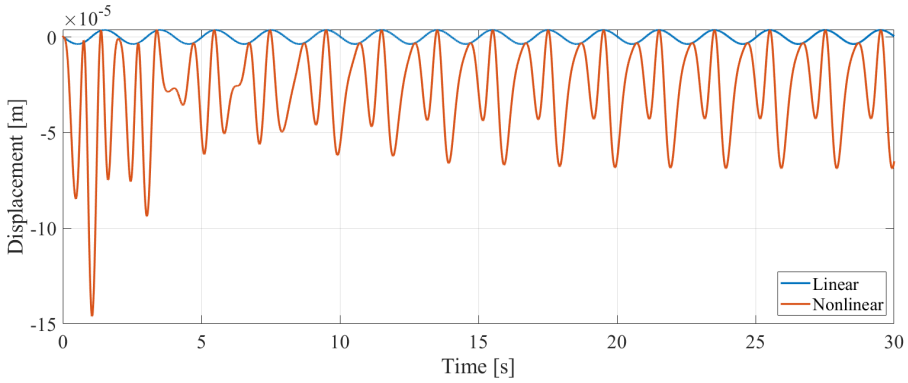

Figure 8.6: Displacement in z direction at midspan (Load case 1.2)

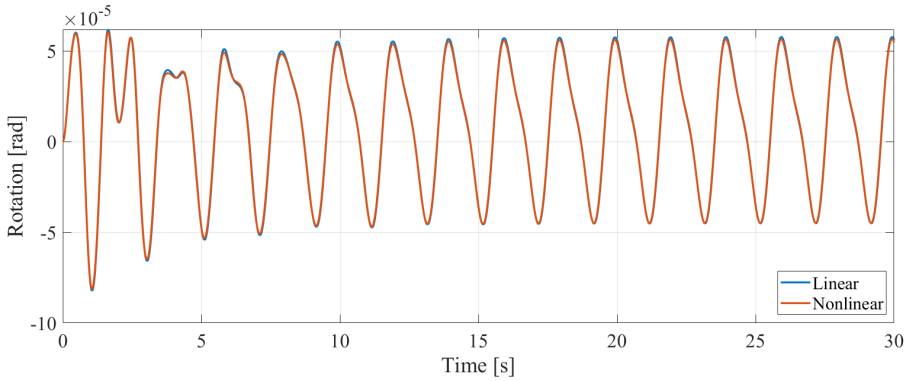

Figure 8.7: Rotation in φ direction at midspan (Load case 1.2)

8.2.3. Load case 1.3

The loading input is set as $H_w = 0.2\text{m}$, $T_w = 2\text{s}$ and $V_c = 0.2\text{m}\cdot\text{s}^{-1}$ for load case 3.3 which is the most severe scenario among the group. The increasing of the wave height considerably increase the displacement. The maximum of the displacement at steady state in y-direction increases from 0.012 m to 0.025 m compared to the load case 2.2 implying a linear response considering that the forces are doubled. It is even more severe in z-direction that the maximum of the displacement increases from 5×10^{-5} m to 30×10^{-5} m, which implies a nonlinear response.

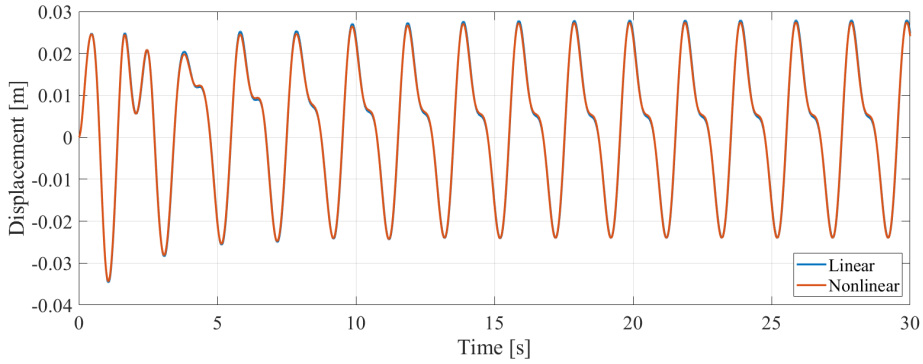

Figure 8.8: Displacement in y direction at midspan (Load case 1.3)

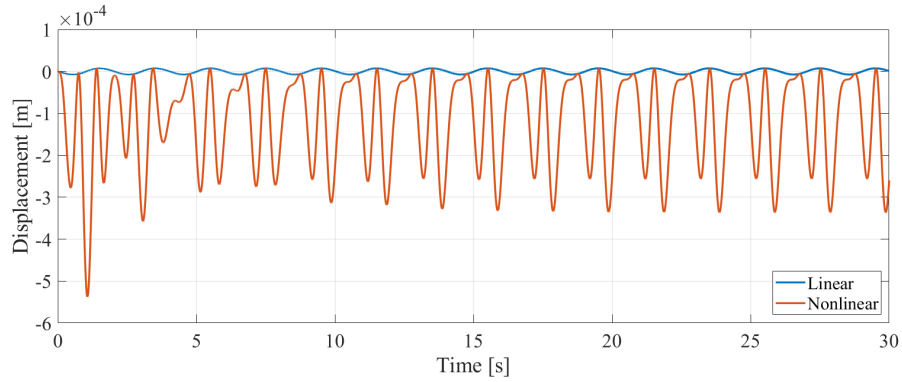

Figure 8.9: Displacement in z direction at midspan (Load case 1.3)

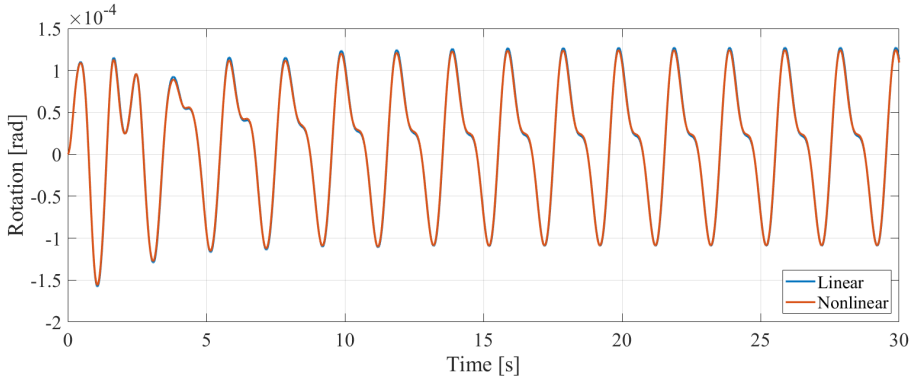

Figure 8.10: Rotation in φ direction at midspan (Load case 1.3)

8.2.4. Discussion about Combined wave and current loading

The results of the displacement based on **Model B** (Equation 6.7) of load group 1 are plotted together as shown in Figure 8.11, Figure 8.12 and Figure 8.13. To study the frequency content in the steady state, the Fourier transform is applied for the segments of the time signals from 15 s to 30 s.

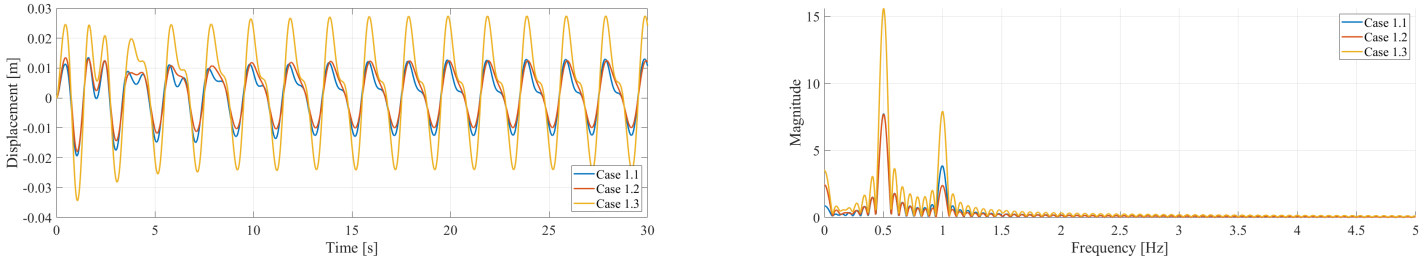

(a) Time domain (b) Frequency domain

Figure 8.11: Displacement in y direction at midspan (Load group 1)

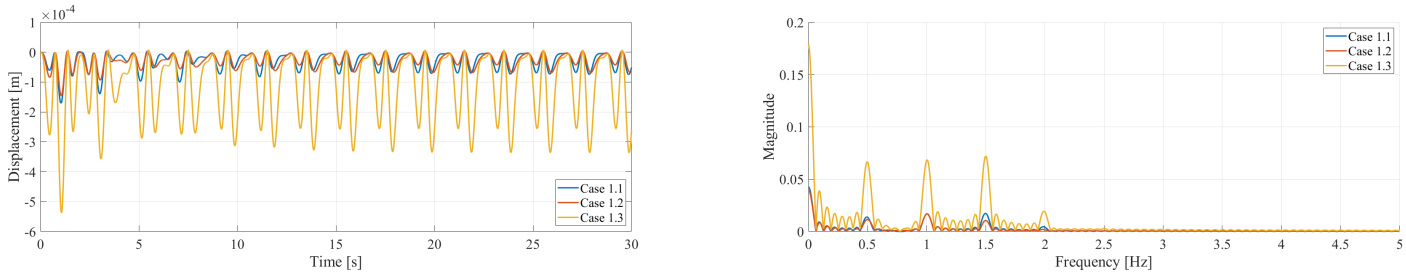

(a) Time domain (b) Frequency domain

Figure 8.12: Displacement in z direction at midspan (Load group 1)

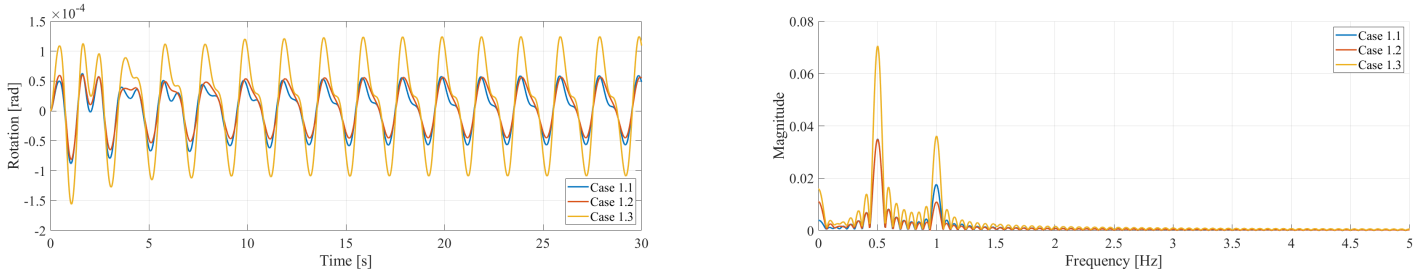

(a) Time domain (b) Frequency domain

Figure 8.13: Rotation in φ direction at midspan (Load group 1)

In the time domain, the displacement of case 1.1 and case 1.2 share a similar amplitude, implying that the change of the current speed does not influence the result very much. The wave height, on the other hand, has a large impact on the amplitude of displacement especially in z-direction, comparing case 1.2 with case 1.3. This is because the loading frequency of the wave is close to the natural frequency of the structure, which induced the resonance of the structure.

In the frequency domain, given that the displacement in y-direction and φ-direction has very similar path in time domain, the frequency contents of these two assumptions are also matching with each other as shown in Figure 8.11 (b) and Figure 8.13 (b). This coupling effect also exists in other load cases. Therefore, only frequency contents in y-direction is discussed hereinafter. The peaks at 0.5 Hz observed in y-direction indicate the loading frequency is 0.5Hz. The strong energy at 1 Hz is a result of the square of the relative

flow velocity on the right hand of Equation 6.7. Besides 0.5 Hz and 1 Hz, 1.5 Hz and 2 Hz are found to have large magnitude, being integer multiples of the loading frequency, which implies the geometrical nonlinearity assumption introduce higher loading frequencies into the system with the magnitude dependent on wave amplitude.

8.3. Oblique wave loading of the SFT

The second group focus on the influence of the wave attack angle. Three attack angle is considered, i.e. 90°, 60° and 45°. Among these cases, the wave height and the wave period is set unchanged which is H_w = 0.1m and T_w = 2s, respectively, whereas the current speed is set to V_c = 0. **Model A** (Equation 6.6) and **Model B** (Equation 6.7) were applied in this load group to study how the linear and nonlinear stiffness assumptions influence the results.

8.3.1. Load case 2.1

The wave attack angle is set to 90° in this case. The response is therefore similar to the load group 1, since the attack angle of these cases are the same. The displacement based on linear and nonlinear stiffness assumption match with each other very well in y-direction and φ-direction. The huge difference is in z-direction where the displacement of nonlinear case is almost 40 times bigger than the one of linear case. The transient state takes around 10s and then the system goes to steady state.

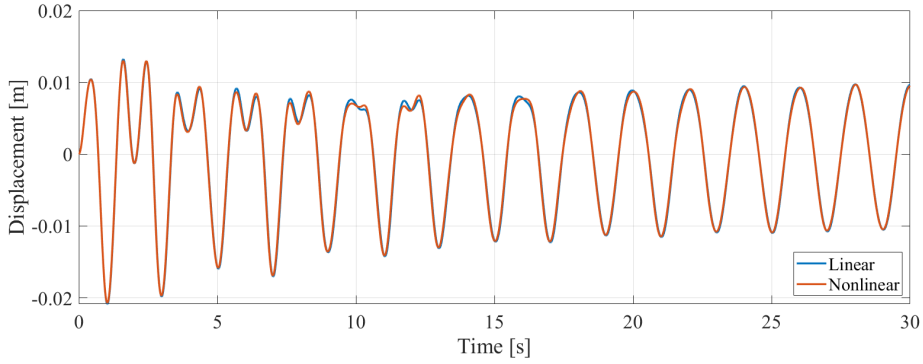

Figure 8.14: Displacement in y direction at midspan (Load case 2.1)

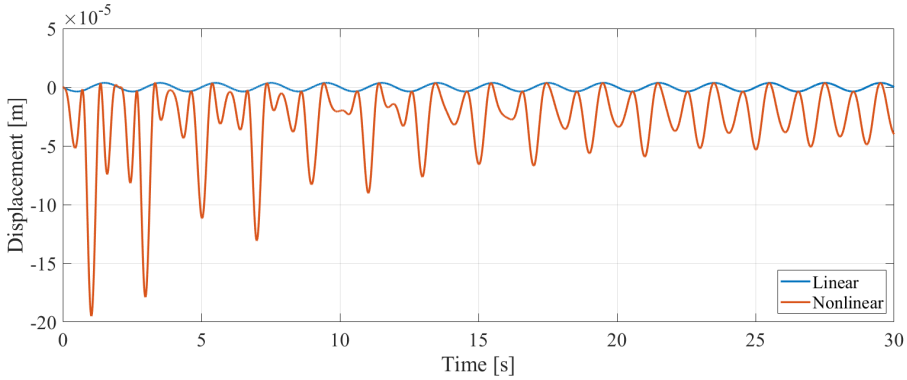

Figure 8.15: Displacement in z direction at midspan (Load case 2.1)

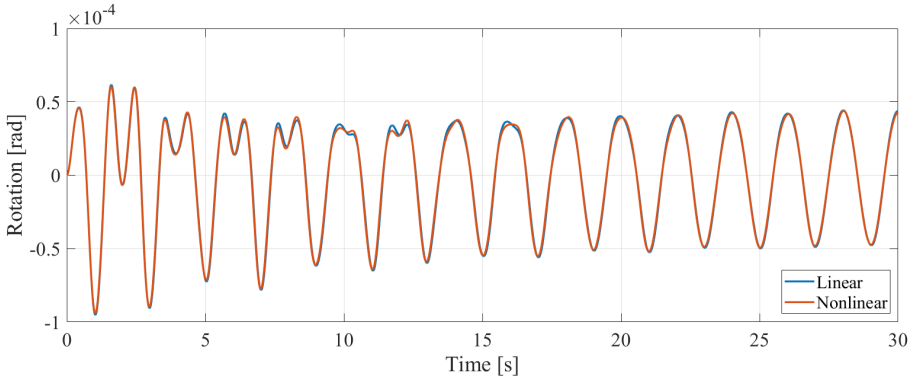

Figure 8.16: Rotation in φ direction at midspan (Load case 2.1)

8.3.2. Load case 2.2

The wave attack angle is set to 60° in this case. It can be observed in the figures that the wave takes time to propagate to the midspan of the tunnel. However, it hardly takes time for the system to go to the steady state. The displacements in z-direction aroused from linear and nonlinear stiffness assumption have similar amplitude, but the equilibrium point of the linear case is 0 while the one of the nonlinear case is negative.

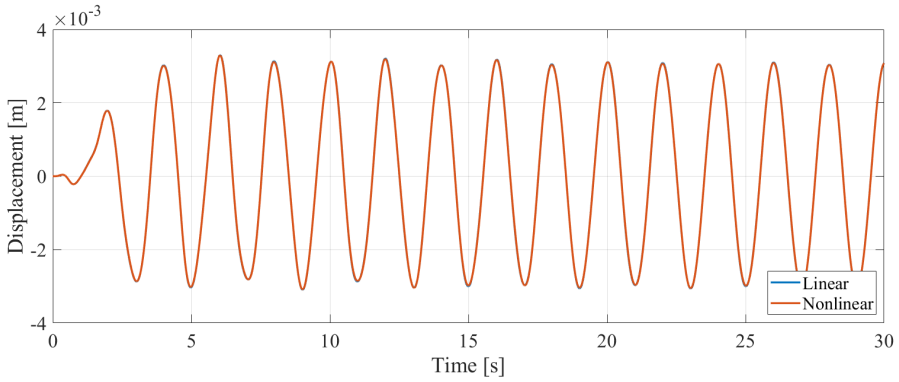

Figure 8.17: Displacement in y direction at midspan (Load case 2.2)

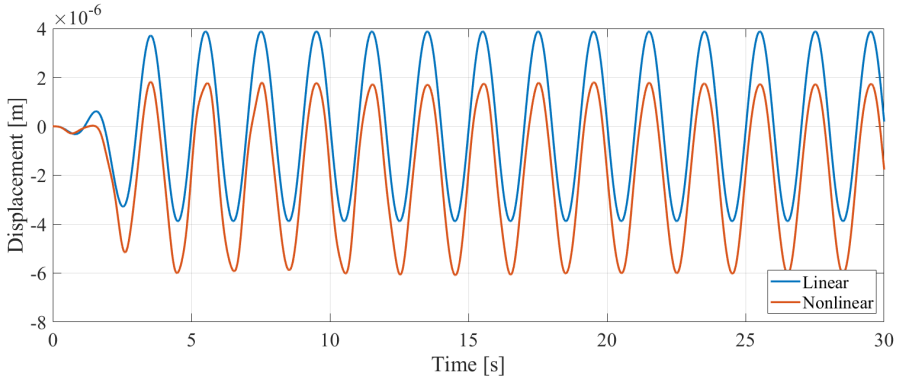

Figure 8.18: Displacement in z direction at midspan (Load case 2.2)

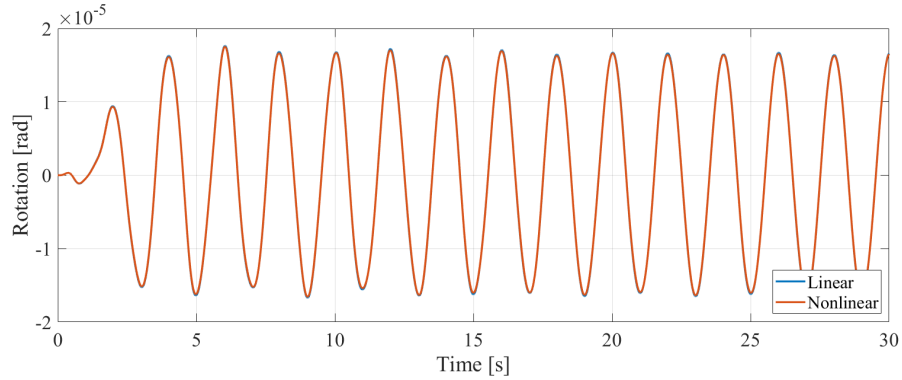

Figure 8.19: Rotation in φ direction at midspan (Load case 2.2)

8.3.3. Load case 2.3

The wave attack angle is set to 45° in this case. Both linear and nonlinear cases give similar results in three directions. When the wave propagate to the midspan of the tunnel, the system takes time very short time to go to the steady state.

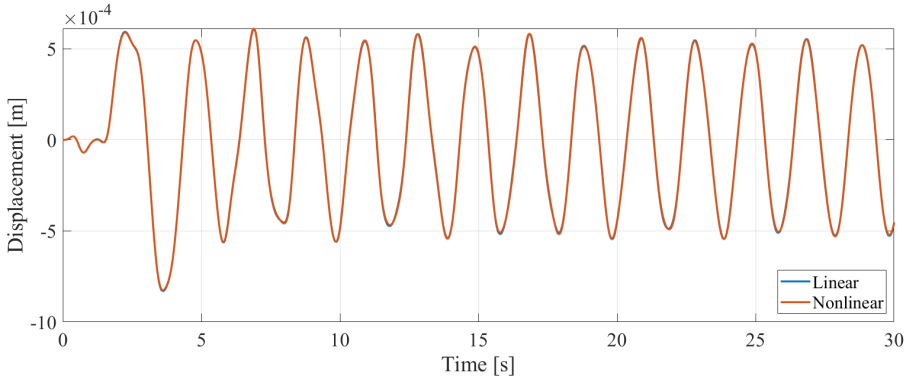

Figure 8.20: Displacement in y direction at midspan (Load case 2.3)

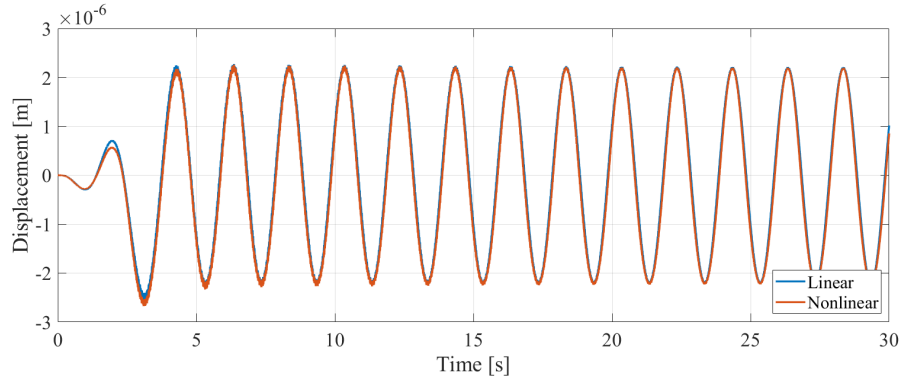

Figure 8.21: Displacement in z direction at midspan (Load case 2.3)

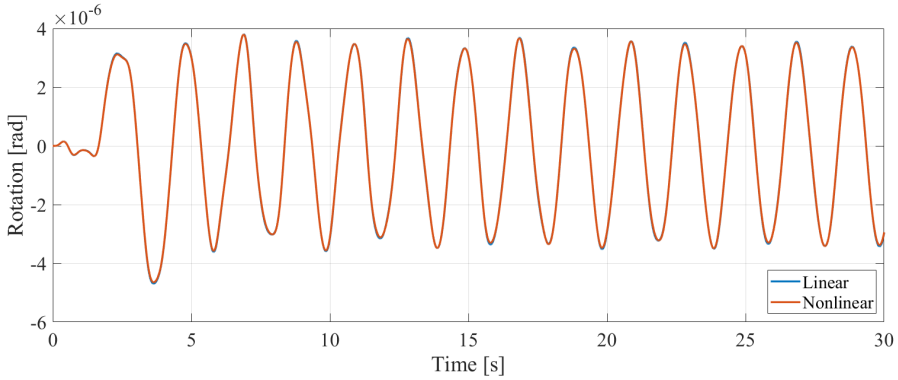

Figure 8.22: Rotation in φ direction at midspan (Load case 2.3)

8.3.4. Discussion about Oblique wave loading

The results of the displacement based on **Model B** (Equation 6.7) of load group 2 are plotted together as shown in Figure 8.23, Figure 8.24 and Figure 8.25. To study the frequency content in the steady state, the Fourier transform is applied for the segments of the time signals from 15 s to 30 s.

In the time domain, the maximum of the response decrease as the increase of the attack angle. This is because the tunnel is only subjected to the component of the hydraulic force when it is loaded in a oblique manner. The change of value also makes the system go to the steady state faster.

In the frequency domain, it can be observed that as a result of increasing of the attack angle, the energy of the frequencies, being integer multiple of the loading frequency, decrease significantly. This leads to a smoother curve as shown in the time domain.

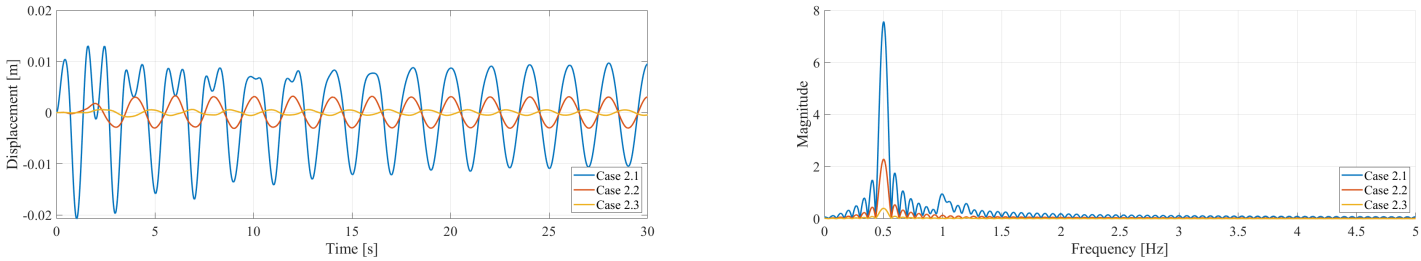

(a) Time domain (b) Frequency domain

Figure 8.23: Displacement in y direction at midspan (Load group 2)

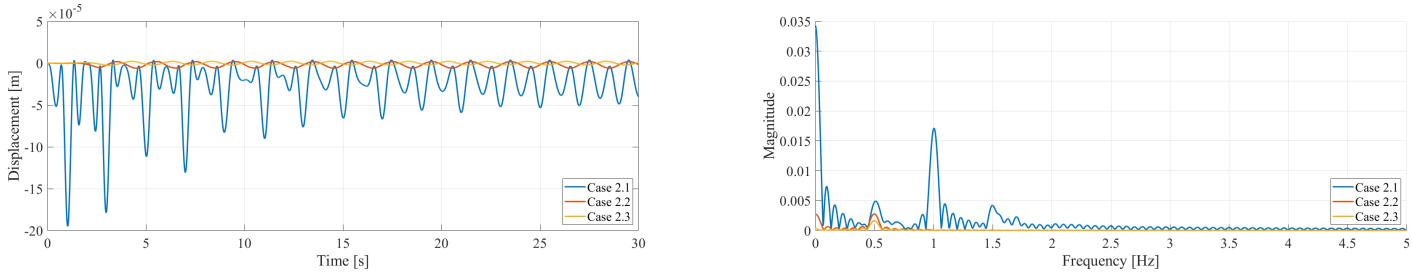

(a) Time domain (b) Frequency domain

Figure 8.24: Displacement in z direction at midspan (Load group 2)

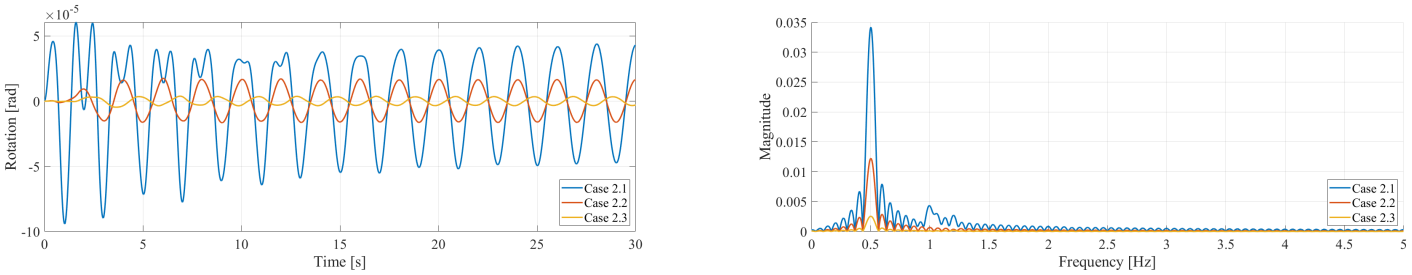

(a) Time domain (b) Frequency domain

Figure 8.25: Rotation in φ direction at midspan (Load group 2)

8.4. Linear and nonlinear stiffness model

To understand the effect of the linear and nonlinear stiffness assumption on the results, i.e., the difference between **Model A** (Equation 6.6) and **Model B** (Equation 6.7), the frequency components of the time domain signals are investigated. Load case 2.1 considering only wave loading is chosen to be discussed in this section because the loading frequency of pure wave loading is easy to recognize from the frequency domain representations. The wavelet transform is applied to the signal to capture the frequency content changing over time and the results are shown in Figure 8.26, Figure 8.27 and Figure 8.28.

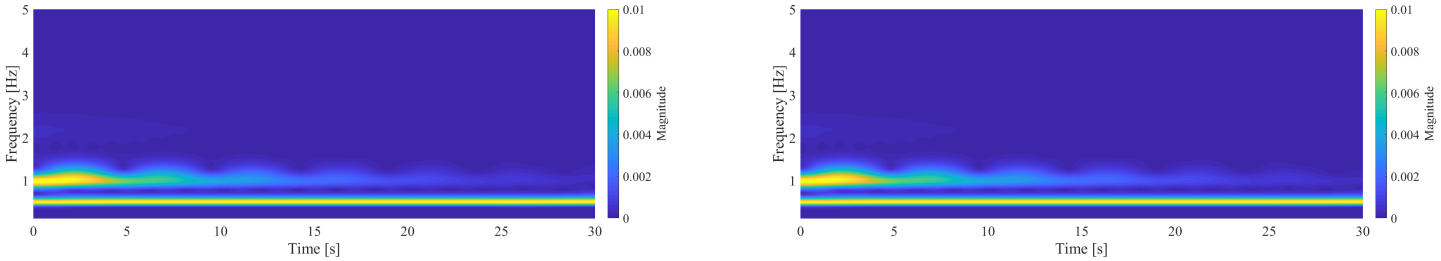

(a) Linear stiffness model (b) Nonlinear stiffness model

Figure 8.26: Wavelet transform of the displacement in y direction at midspan (Load case 2.1)

As shown in Figure 8.26, the frequency content is same for both assumption. The magnitude at 0.5Hz is the strongest and does not decay over time indicating the loading frequency is 0.5Hz, which conforms to the condition in load case 2.1 where the wave period is 2s. Another strong peak is observed at 1Hz, which is the first natural frequency in y direction. It declines to a considerable small level due to the presence of hydrodynamic damping. Some other natural frequencies can also be observed at around 1.2Hz and 2.2Hz corresponding to the 3rd mode and the 5th mode. Only mode shape of the odd order can be observed because the system is subjected to symmetric loading.

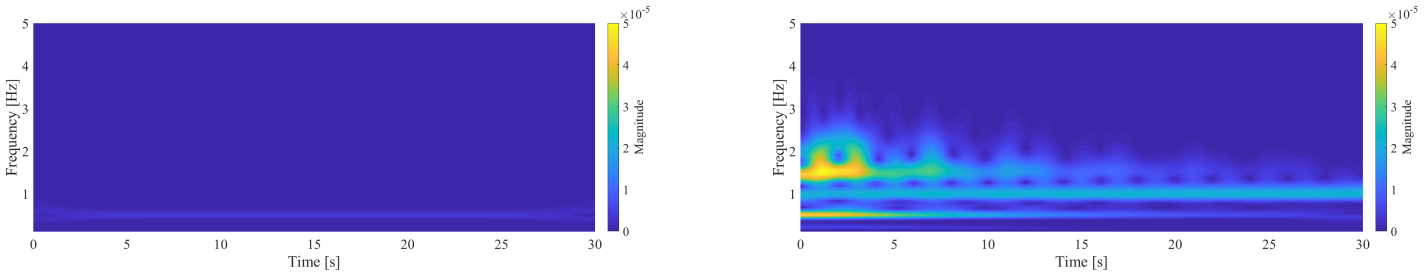

(a) Linear stiffness model (b) Nonlinear stiffness model

Figure 8.27: Wavelet transform of the displacement in z direction at midspan (Load case 2.1)

Interestingly, the frequency content in z-direction as shown in Figure 8.27 has a huge difference based on

linear and nonlinear stiffness assumption, which conforms with the observation the in Fourier transform as mentioned previously. There is only one frequency at 0.5Hz in the results of **Model A** indicating the loading frequency of the linear case of which the magnitude is very small. On the contrary, the frequency content of the nonlinear case is very complicated with a larger magnitude. In Figure 8.27 (b), the magnitude of the loading frequency of 0.5Hz declines in the first 15s, and ends up at the value similar to the linear case. However, there is no attenuation observed in the frequency of 1Hz. In fact, this is also the loading frequency, which comes from the second order of the flow velocity $\dot{y}$ and $\dot{z}$ on the right hand side of Equation 6.7. This second order doubles the value of the load frequency leading to the constant magnitude at 1 Hz. The magnitude around 1.3Hz and 2.2 Hz is gradually damped out, indicating the value of the 3rd natural frequency and the 5th natural frequency of the y-direction, respectively. These imprinted natural frequencies are the result of the coupled motion in three directions, which is bigger than the natural frequencies of the uncoupled motion in y-direction and smaller than the ones in z-direction.

As discussed in this section, the results based on the nonlinear stiffness assumption provide more complete information about the dynamic response. It gives more insight to understand the dynamic behaviour especially in z-direction. Therefore, for further interpretation of the results, only the analysis based on the nonlinear stiffness assumption is considered.

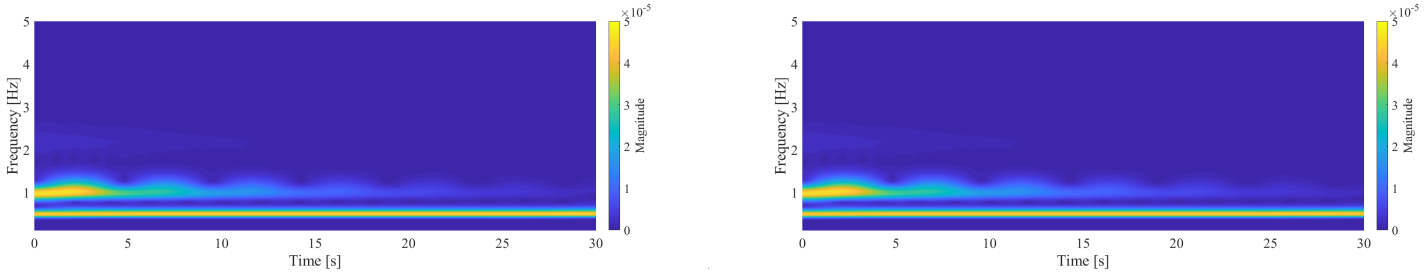

(a) Linear stiffness model

(b) Nonlinear stiffness model

Figure 8.28: Wavelet transform of the displacement in φ direction at midspan (Load case 2.1)

8.5. Global dynamic behaviour of the SFT

The global dynamic analysis based on **Model B** (Equation 6.7) with different boundary conditions were investigated to understand the its effect on the results. Meanwhile, a 2D cross-sectional dynamic analysis was carried out for comparison. This dynamic analysis simplifies the BOEF model as a rigid body with a boundary condition of both ends free. The longitudinal motions of the model are ignored by this simplification and the rigid tunnel only contains three DOFs, i.e. horizontal, vertical and rotational displacement. Load case 1.1 and Load case 2.2 are chosen to be discussed in this section, since they represent the combined wave and current loading group and the oblique wave loading group.

The results given by the global dynamic analysis and the 2D cross-sectional dynamic analysis are shown in Figure 8.29, Figure 8.30 and Figure 8.31. Basically, the 2D cross-sectional dynamic analysis provides similar results at midspan compared with the global dynamic analysis in load case 1.1. This is due to the fact that the boundary conditions do not influence the response at midspan very much because the distance between tunnel tips to the midspan is very large.

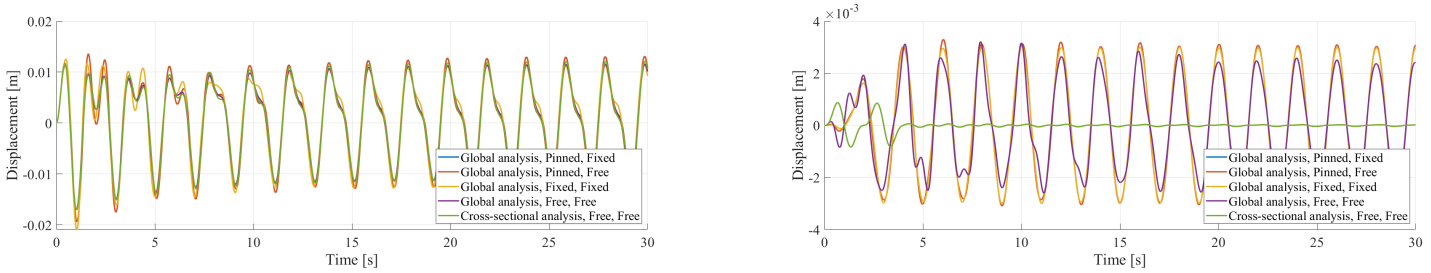

(a) Load case 1.1

(b) Load case 2.2

Figure 8.29: Displacement in y direction at midspan (with different boundary conditions)

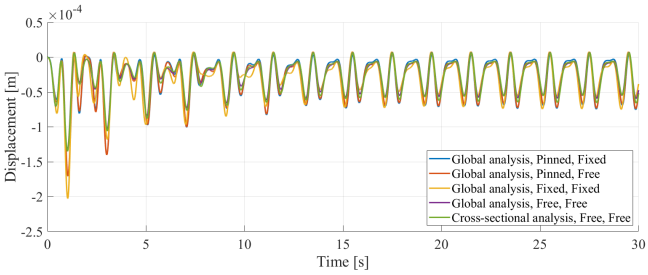

(a) Load case 1.1

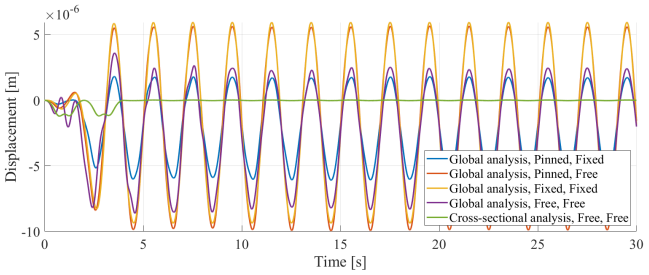

(b) Load case 2.2

Figure 8.30: Displacement in z direction at midspan (with different boundary conditions)

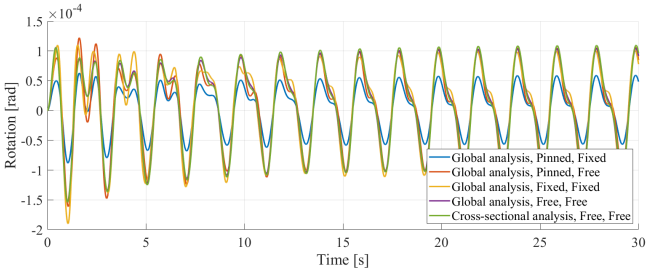

(a) Load case 1.1

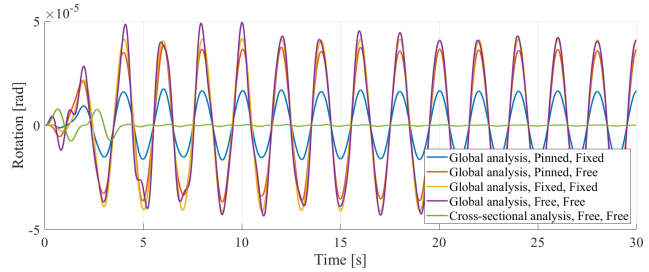

(b) Load case 2.2

Figure 8.31: Rotation in φ direction at midspan (with different boundary conditions))

When it comes to load case 2.2, the drawbacks of the cross-sectional analysis are revealed as the path of the results yielded from the cross-sectional analysis does not comply with any of the global analysis. The maximum value of the response given by the cross-sectional analysis is significantly smaller than all the other cases. This is because that the cross-sectional analysis is not capable to capture the flexible deformation in the tunnel, which place a important role when the tunnel is subjected to oblique wave loading.

8.6. Vortex induced vibration of the SFT

The third group only contains current loading to study the vortex induced vibration. **Model C** (Equation 6.8) and **Model D** (Equation 6.9) were applied in this group. At first glance, the possibility of vortex induced vibration is considerably small since the natural frequency of the vertical motion is very high, which requires an unreasonable high current speed. However, a closer inspection reveals that the frequencies of the horizontal motion is imprinted in vertical motion because of the coupled motions in the nonlinear stiffness assumption. This makes the first natural frequency in vertical direction significantly low and is assumed to make vortex induced vibration easy to happen.

As discussed in subsection 2.4.4, the lock-in phenomenon of the vortex induced vibration takes place when the reduced velocity V_n is larger than 5. Given that the first natural frequency in vertical direction is 1.000Hz and the diameter of the tunnel cross section is 0.25m, the flow velocity is determined by:

$$V_c > V_n f_n D = 5 \times 1 \times 0.25 = 1.25\text{m}\cdot\text{s}^{-1}. \tag{8.3}$$

To make the lock-in phenomenon clear to observe, the current speed is set to $V_c = 1.5\text{m}\cdot\text{s}^{-1}$ for load case 3.1. For comparison, the current speed is set to $V_c = 1.0\text{m}\cdot\text{s}^{-1}$ for load case 3.2. It is worth noting that 1.5 $\text{m}\cdot\text{s}^{-1}$ and 1.0 $\text{m}\cdot\text{s}^{-1}$ are theoretical value, as in full scale being 10.6 $\text{m}\cdot\text{s}^{-1}$ and 7.1 $\text{m}\cdot\text{s}^{-1}$. The parameters used for Equation 4.10 and Equation 4.11 are determined as suggested by Ogink and Metrikine (2010):

$$\begin{aligned} C_{D0} = 1.1856,\ C_{L0} = 0.3842, \\ St = 0.1932,\ A = 12.0,\ \epsilon = 0.7. \end{aligned} \tag{8.4}$$

8.6.1. Load case 3.1

The results produced by both simplified wake oscillator model and non-simplified wake oscillator model are plotted together for comparison in Figure 8.32, Figure 8.33 and Figure 8.34. The path of the non-simplified wake oscillator indicate the magnitude of the VIV is very small and provide the equilibrium point. However, the curve of the simplified wake oscillator moves around that point and the maximum displacement of the wake oscillator is considerably large compared with the one of linear case especially in z-direction.

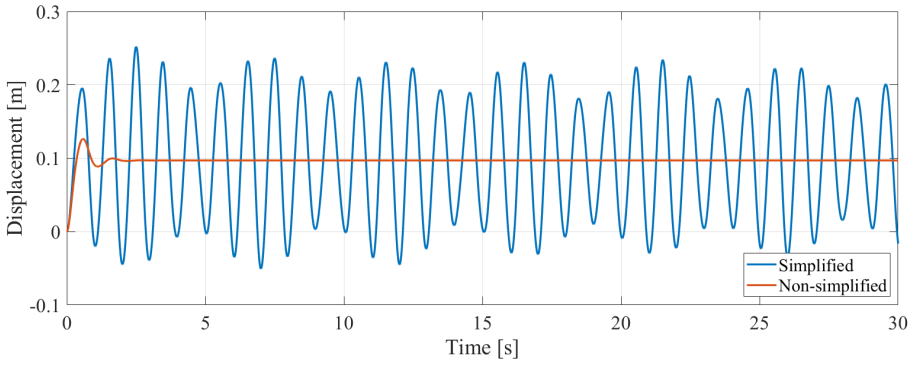

Figure 8.32: Displacement in y direction at midspan (Load case 3.1)

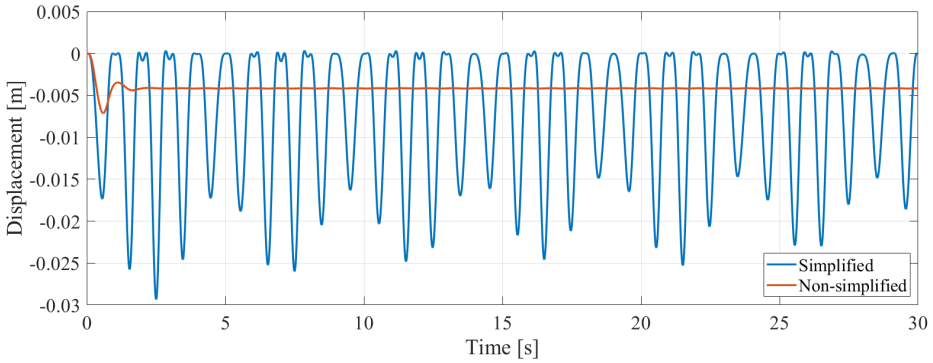

Figure 8.33: Displacement in z direction at midspan (Load case 3.1)

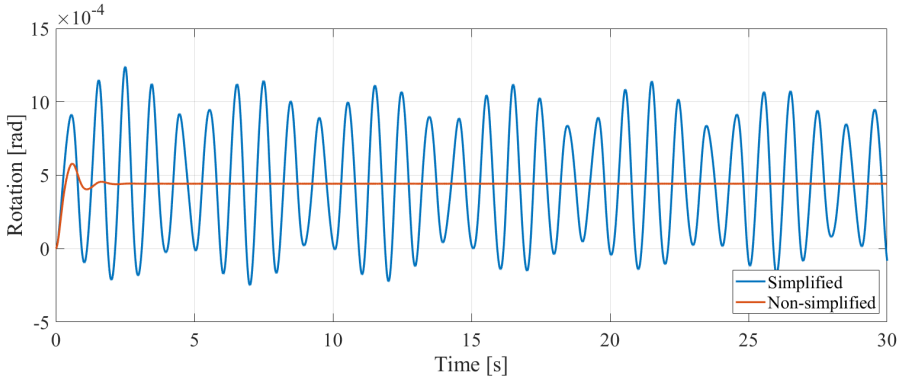

Figure 8.34: Rotation in φ direction at midspan (Load case 3.1)

8.6.2. Load case 3.2

The results of load case 3.2 are shown in Figure 8.35, Figure 8.36 and Figure 8.37. The results are similar with the previous section.

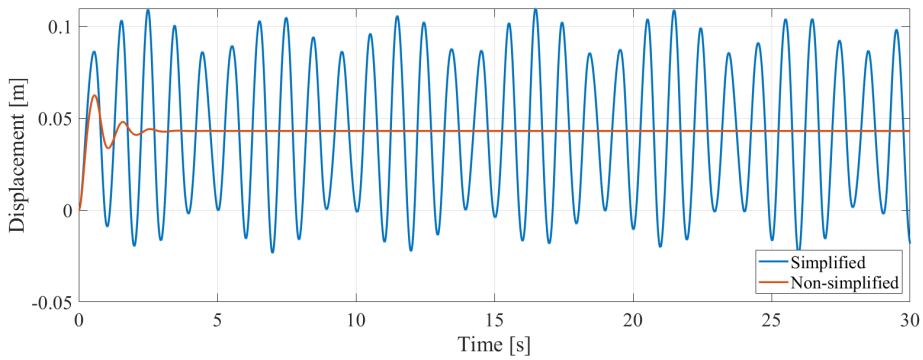

Figure 8.35: Displacement in y direction at midspan (Load case 3.2)

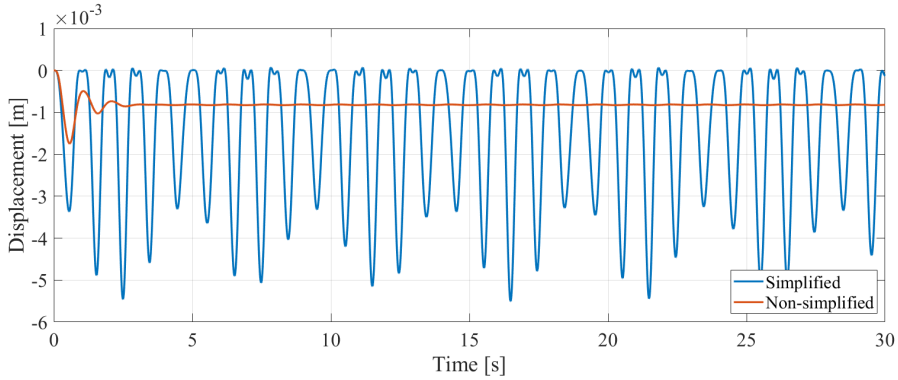

Figure 8.36: Displacement in z direction at midspan (Load case 3.2)

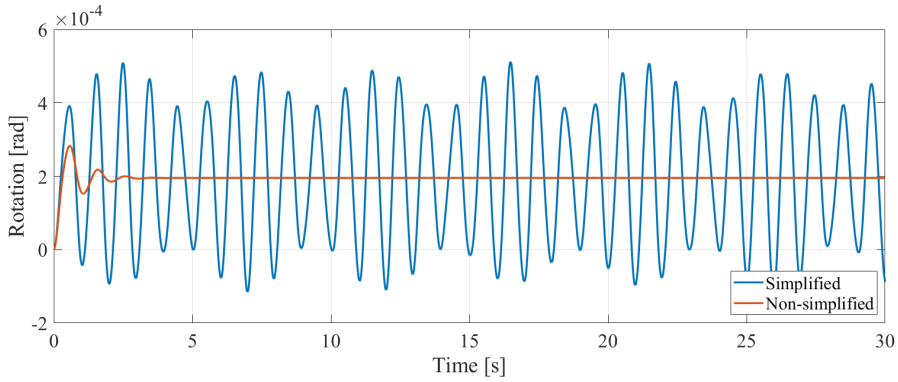

Figure 8.37: Rotation in φ direction at midspan (Load case 3.2)

8.6.3. Discussion about Vortex induced vibration

The results of **Model C** (Equation 6.8) and **Model D** (Equation 6.9) are plotted together for comparison. The Fourier transform is applied to the steady state of the time signals from 15 s to 30 s. When applying the simplified wake oscillator, VIVs with high amplitudes take place in both cases. The peak at 1Hz and 1.2Hz in all three directions, being the value of the 1st and 3rd natural frequencies in y-direction, indicates the occurrence of the lock-on phenomenon. However, the velocity of the structure is rather large in both load cases which conflicts with simplification assumption, in which the vertical velocity of the tunnel is considerably small compared with the current speed, therefore the simplified model is no longer suitable. In this case, **Model D** (Equation 6.9) would provide a more reliable results.

The results of **Model D** (Equation 6.9) indicate that the amplitudes of the VIVs are extremely small for both load cases. The path goes to constant after 2.5s and the increasing of the current speed only increase the

value of this constant but does not change the state of the motion. This implies that the imprinted frequencies noted in z-direction seem to have no connection with the occurrence of a severe VIV. This is due to the fact that the vertical stiffness is considerably large making natural frequencies in z-direction very high, so that the loading frequency is far away from the natural frequencies. Therefore, the lock-on phenomenon could hardly happen. However, as the free-span between two groups of anchoring cables increases or the stiffness in vertical direction decreases, the stiffness in z-direction becomes small, which would make the natural frequency close to the loading frequency. For this reason, the VIV is expected to have a large impact and further analysis is needed.

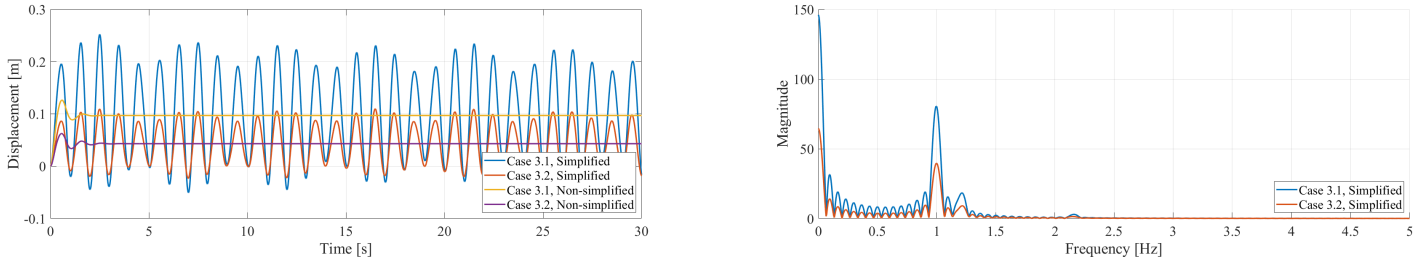

(a) Time domain (b) Frequency domain

Figure 8.38: Displacement in y direction at midspan (Load group 3)

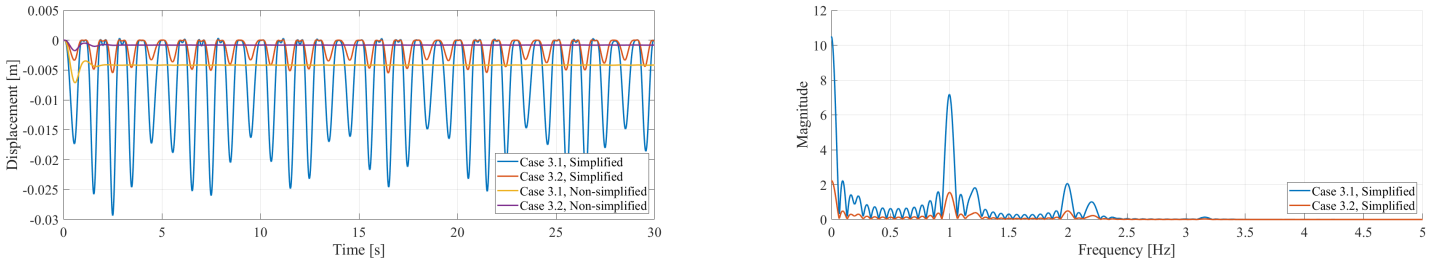

(a) Time domain (b) Frequency domain

Figure 8.39: Displacement in z direction at midspan (Load group 3)

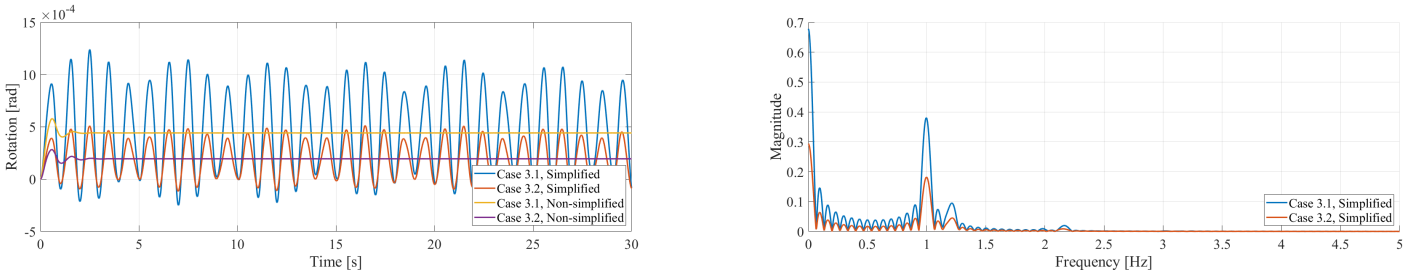

(a) Time domain (b) Frequency domain

Figure 8.40: Rotation in φ direction at midspan (Load group 3)

8.7. Discussion about the assumptions

Several assumptions have been made to construct the stiffness model and the submerged floating tunnel model. Some of these assumptions can be validated with modeling results to see if the model is consistent with itself. Other assumptions need further physical test or FE software to validate. The assumptions which are expected to have potential influence on the results of the model are validated if possible and otherwise, their effect is discussed.

Small angles of rotation

The order of magnitude of the maximum amplitude of the rotational angle is -5 with unit of rad. This means that the assumption of small rotational angles for **Model A** is a reasonable assumption.

Small structure velocity

The maximum velocity observed in load group 3 when applying **Model C** is 0.9 m/s. It conflicts with the assumption that the velocity of the structure should be considerably small compared with the current velocity. **Model C**, therefore, is not applicable for laod group 3.

Corss-section

When the tunnel structure is subjected to symmetric loading, the response is also symmetric in space, which indicates that the cross section of the tunnel is uniform in axial direction.

8.8. Conclusion

The conclusions contributed to the understanding of

- The geometrical nonlinearity of the stiffness mainly affects the results in vertical direction and inducing the pendulum phenomenon. The vertical displacement results from a nonlinear stiffness model could be 5 times bigger than the one from a linear stiffness model. This difference decreases as the attack angle change from 90° to 45°.
- The geometrical nonlinearity of the stiffness could imprints natural frequencies of horizontal direction to vertical direction. However, this imprinted natural frequencies does not related the VIV in vertical direction.
- The 2D cross-sectional analysis is able to simulate the response at the midspan of SFT when the attack angle is 90°. When the SFT is subjected to the oblique wave loading, the discrepancy between the 2D cross-sectional analysis and the global analysis is significant, implying the drawback of the 2D cross-sectional analysis is not capable to capture the longitudinal behaviour of the response. On the other hand, the global analysis performs well in any load cases.
- The SFT is more sensitive to the wave loading than the current loading, since the wave loading frequencies is possible to be close to the natural frequencies of the structure and induce severe resonance.
- As the attack angle change from 90° to 45°, the maximum responses in three directions decrease.
- Base on this scaled model, as long as the vortex shedding frequency is not close to the vertical natural frequencies, regardless of the horizontal natural frequencies. The impact of the VIV can be ignored.

9

Parametric study

The influence of the design parameters on the dynamic response is investigated in this chapter. The parametric study uses the input parameters and the response of Load case 2.1 as a reference, where the system is only subjected to wave loading. **Model B** (Equation 6.7) is applied for this study. Aiming to gain insight for the impact of the parameters, only the maximum response at steady state of the tunnel is of interest. The location and the time of the maximum response is therefore not specified.

9.1. Influence of the buoyancy weight ratio

The buoyancy weight ratio (BWR) is defined as the ratio between the buoyancy acting on the tunnel and the sum of the permanent weights and live loads. In this case, the BWR is determined by the ratio between buoyancy and the weight of the tunnel as shown in Equation 9.1.

$$BWR = \frac{F_B}{W} = \frac{\rho_w g d_t}{\rho_t g d_t} = \frac{\rho_w}{\rho_t}. \tag{9.1}$$

The water density remains the same, so increasing the BWR means a decreas of the density of the tunnel. The net buoyancy per unit length is defined by virtue of Equation 9.2. Decreasing the density of the tunnel results in an increase of net buoyancy, which subsequently increases the pretension in the anchoring cables. Therefore, the study of the BWR is also the study of the pretension in the anchoring cables.

$$F_{NB} = F_B - W = (\rho_w - \rho_t) g d_t. \tag{9.2}$$

It is worth noting that the diameter of the tunnel cross-section also makes a difference to the net buoyancy. However, it is not related to the BWR. This implies that a same BWR may lead to different input parameters without clarification of the diameter. This is the drawback of the study of the BWR and deserves close consideration. In this study, the diameter is specified unchanged as $d_t = 0.25$m. The range of the BWR of interest is set as 1.2-2.1. The results of the maximum response in three directions are shown in Figure 9.1. Clearly, maximum responses of the system in three directions reduce gradually as the BWR increase. Therefore, the upper boundary of the BWR is limited by the financial aspect, not the structural aspect.

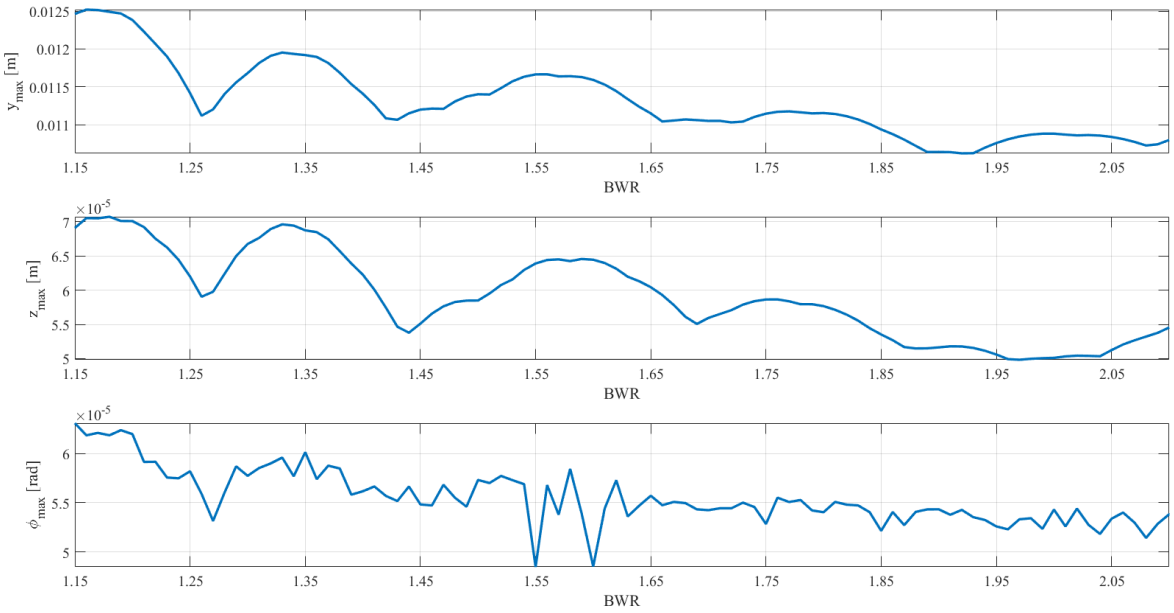

Figure 9.1: Influence of the BWR

9.2. Influence of the length of the tunnel

The length of the tunnel is defined as the distance between the tunnel bow and the tunnel stern. It has a strong influence on the mass and the stiffness of the tunnel. However, in this continues system, it is the mass per unit length that is taken into account. Therefore, the length of the tunnel only make a difference to the stiffness of the tunnel and consequently influence the natural frequency of the system.

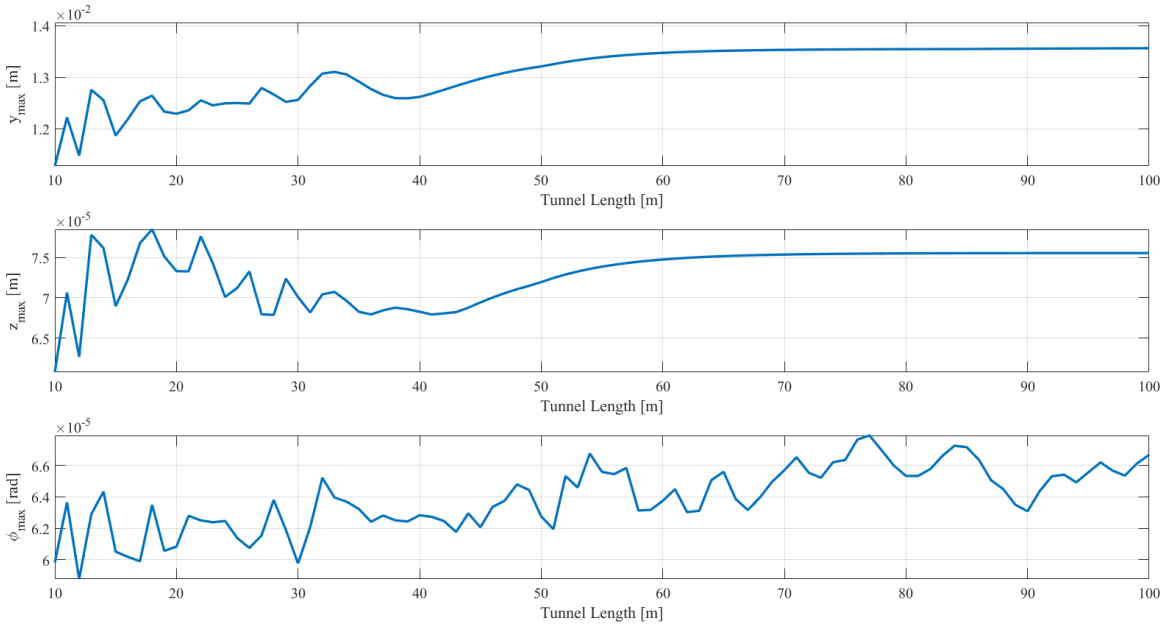

Figure 9.2: Influence of the length of the tunnel

The results of the parametric study of the length of the tunnel are shown in Figure 9.2. The range of tunnel length for the study is 10m−100m. Some peaks can be observed in y-direction and z-direction, which is due

to the occurrence of the resonance when the decreasing natural frequencies meet the loading frequencies. After the tunnel length reaching the value of 60m, the maximum of the response in y-direction and z-direction tends to become a constant. This phenomenon adds evidence to the fact that the SFT is a modular structure and is theoretically feasible to surpass spans of any length.

9.3. Influence of the stiffness of the cables

The stiffness of the vertical and inclined cables plays a very important role in the dynamic behaviour of the system. These cables compose the constraint for the motions in horizontal, vertical and rotational direction. The inclined cables mainly control the motion in horizontal direction, while the vertical cables restrain the motion in vertical and rotational direction. The stiffness is also the dominant part of the natural frequency. Therefore, a suitable combination of vertical and inclined cables can avoid the resonance and limit the response in a very small magnitude. Conversely, an improper set of vertical and inclined cables may lead to high response of the tunnel, sometimes even instability. The results of the parametric study of the combination of the vertical and inclined cables are shown in the following figures. The range of the stiffness of vertical and inclined cable is both set as 0.1×10^{-6}N/m -10×10^{-6}N/m.

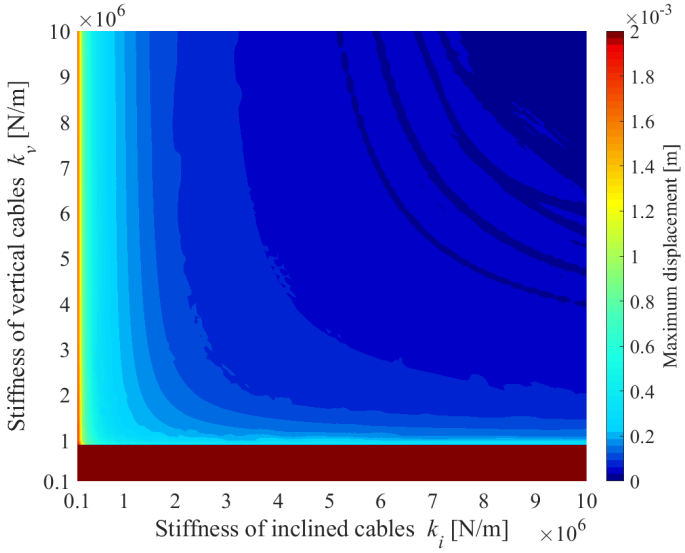

Figure 9.3: Influence of the stiffness for y_{max}

As shown in Figure 9.3, the maximum displacement in y-direction is mainly influenced by the stiffness of the inclined cable. It is worth noting that the stiffness of the vertical cables should be larger than 1×10^6N/m to avoid the instability in the system, which leads to an extremely large value of y_{max}. This extremely large value is denoted by dark red as shown in Figure 9.3. Some dark blue lines are observed at the top right corner of the figure, indicating that a certain combination of the vertical cables and the inclined cables provides a strong constraint. This gives the insight for the design of the anchoring system, which suggests choosing the value of the stiffness on the dark blue lines rather than simply increasing the value.

The result of the influence of the stiffness on the maximum displacement in z-direction is shown in Figure 9.4. The maximum displacement in z-direction is more sensitive to the stiffness of the vertical cables than to the stiffness of the inclined cables. As discussed previously, the stiffness of the vertical cables should be larger than 1×10^6N/m to avoid the instability in the system.

Figure 9.5 showing the influence of the stiffness on the maximum displacement in φ-direction has similar properties with Figure 9.5, which gives the evidence to the fact that the coupled motion between y-direction and φ-direction. Some dark blue lines are observed at the top right corner of the figure as well, which can be referred to for further application in design. Furthermore, the condition for the stiffness of the vertical cables larger than 1×10^6N/m to avoid instability is also applied in this direction.

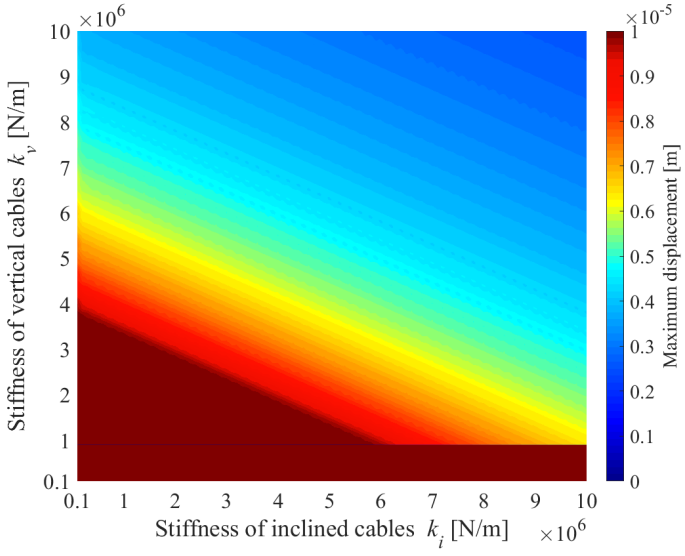

Figure 9.4: Influence of the stiffness for z_{max}

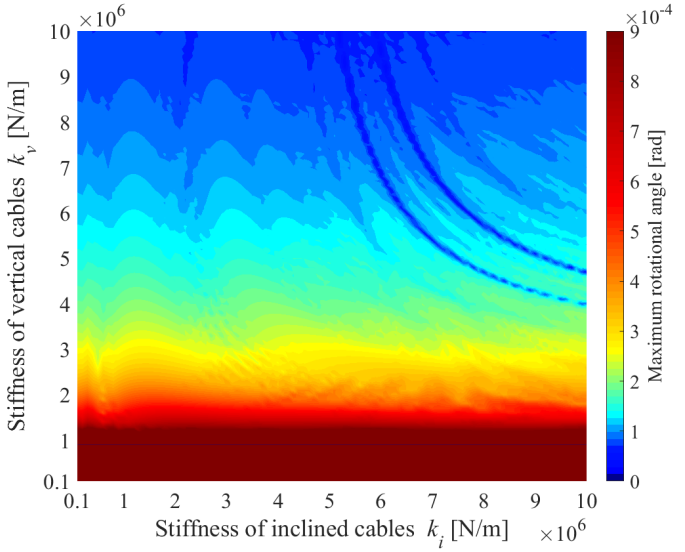

Figure 9.5: Influence of the stiffness for φ_{max}

9.4. Influence of the inclination of the cables

The parametric study of the influence of the inclination of the cables is presented in this section. Only the change of the inclination of the inclined cables is considered and the vertical cables remain vertical. The inclination angle of interest is from 15° to 75°. With the increase of the inclination angle, the length of the inclined cable also increase and subsequently decrease the stiffness of the cables if the material remains unchanged. Therefore, the study is divided into two parts. The first part assumed that the stiffness of the cables remains the same when the inclination angle is changed by theoretically change the material properties. This part aims to find out the optimal angle to applied a certain stiffness. The second part is of practical interest, assuming that the material of the cables remains the same. This part aims to find out the optimal angle to apply anchoring inclined cables.

The results of these two parametric studies in Figure 9.6 shows that with the increase of the inclination angle, the value of the maximum response in three directions with same material assumption rise gradually, meanwhile the one with same stiffness assumption share the similar path and reach to a peak when the angle is 70°. It is worth noting that the maximum response in y-direction based on the same material assumption is

found to decrease at first when the angle is increased from 15° to 35°. This is due to the fact that the stiffness of the cables is increased significantly at the same time. Based on the results of these two parametric studies, it is suggested that the optimal angle to applied a certain stiffness is the smaller the better and the optimal angle to apply anchoring inclined cables is 35° to 45°.

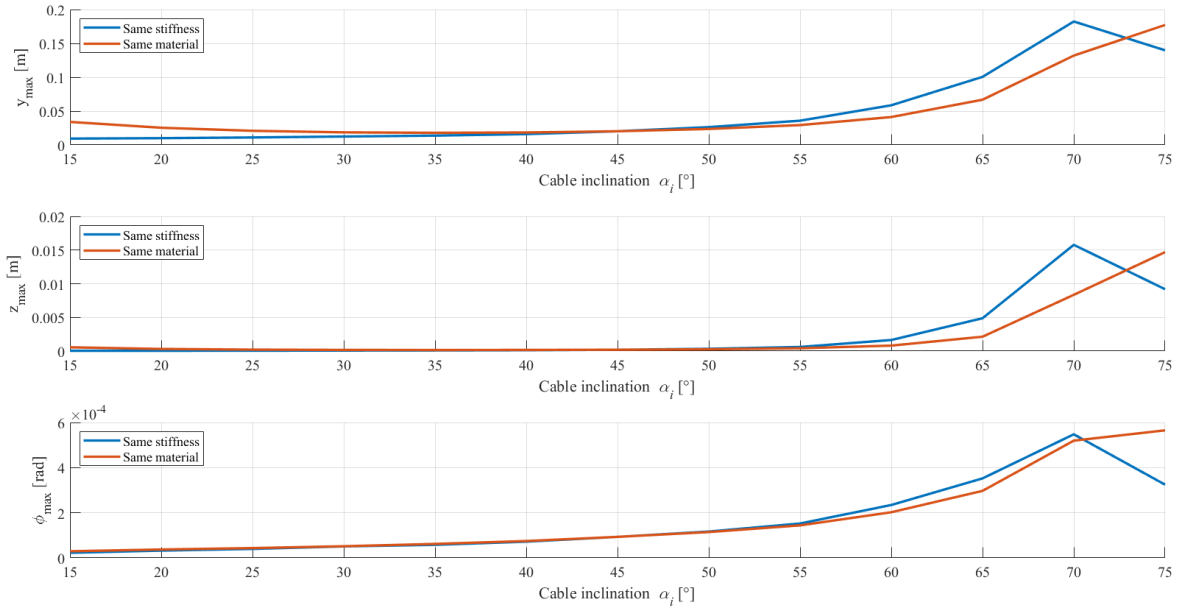

Figure 9.6: Influence of the inclination of the cables

9.5. Influence of the distribution of pretension

The distribution of pretension in cables is defined by a pretension distribution coefficient γ, which is related to the initial static tension forces in the cables by virtue of Equation 9.3. Note that the coefficient γ describes how much amount of the net buoyancy is assigned for each cable and has a range from 0 to 0.5. $\gamma = 0$ means all the net buoyancy force is allocated to the inclined cables and $\gamma = 0.5$ means all the net buoyancy force is assigned to the vertical cables. The results of the parametric study on the influence of the distribution of pretension is shown in Figure 9.7 with pretension distribution coefficient γ range from 0.1 to 0.4.

$$
\begin{aligned}
T_v &= F_{NB} s_v \gamma \\
T_i &= \frac{F_{NB} s_i (0.5 - \gamma)}{\sin \alpha_i}
\end{aligned}
\tag{9.3}
$$

The maximum responses in three directions is gradually increased as the increase of pretension distribution coefficient γ. Therefore, the more net buoyancy force is distributed in inclined cables, the better the responses of the system is controlled.

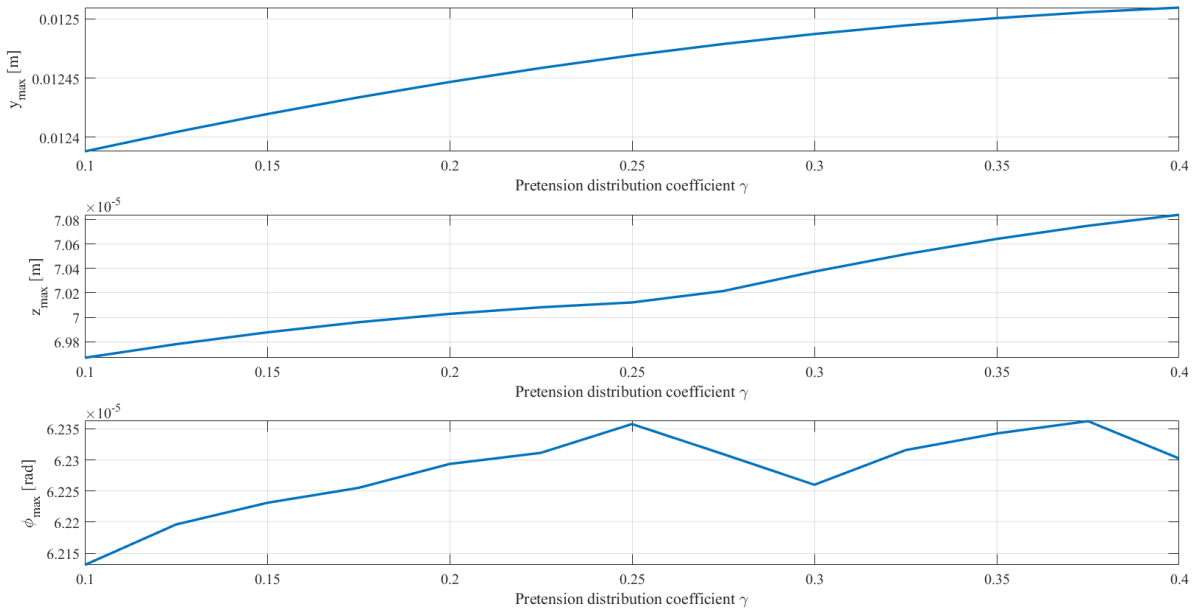

Figure 9.7: Influence of the distribution of pretension

9.6. Influence of the boundary conditions of the tunnel

The boundary conditions of the tunnel are simplified from the configuration of the connections of a SFT with the shores. It is one of the most relevant issues in the design for a SFT. In this parametric study, Model B (Equation 6.7) with respect to four kinds of boundary conditions is considered, which represents the both end pinned beam & both end fixed torsion rod model (denoted as Pinned, Fixed), the both end pinned beam & both end free torsion rod model (denoted as Pinned, Free), the both end fixed beam & both end fixed torsion rod model (denoted as Fixed, Fixed) and the both end free beam & both end free torsion rod model (denoted as Free, Free). Load case 1.1 and load case 2.2 are chosen as the loading conditions in this study, the results of the response at midspan of the tunnel and at 1.5 m from tunnel bow are shown from Figure 9.8 to Figure 9.13.

The response of different boundary conditions at the midspan are similar with each other. This is because that the distance between the midspan and both ends of the tunnel is long enough so that the influence of the boundary conditions is very small.

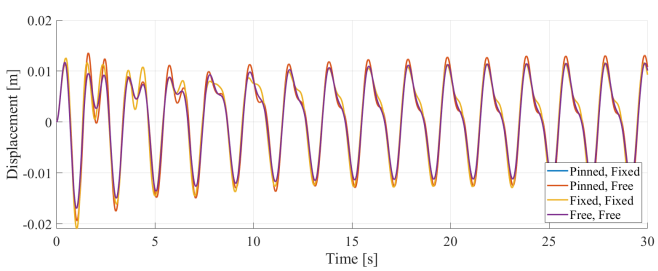

(a) Load case 1.1

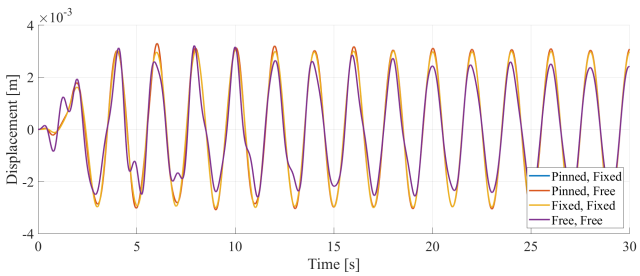

(b) Load case 2.2

Figure 9.8: Influence of the boundary conditions in y direction at midspan

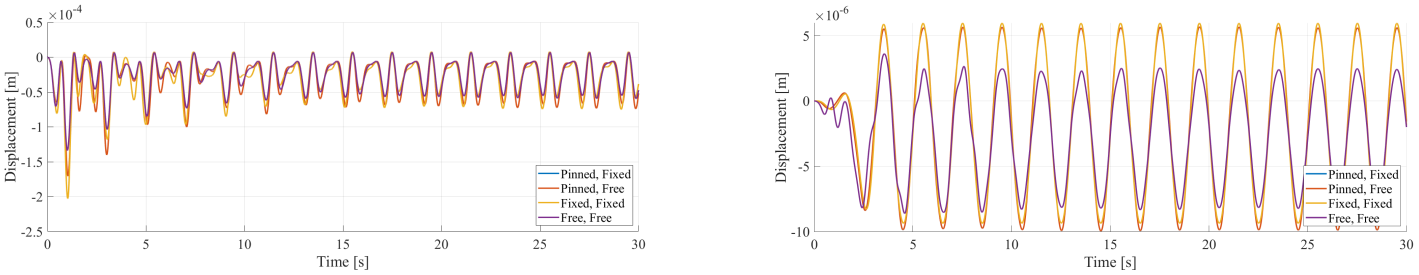

(a) Load case 1.1 (b) Load case 2.2

Figure 9.9: Influence of the boundary conditions in z direction at midspan

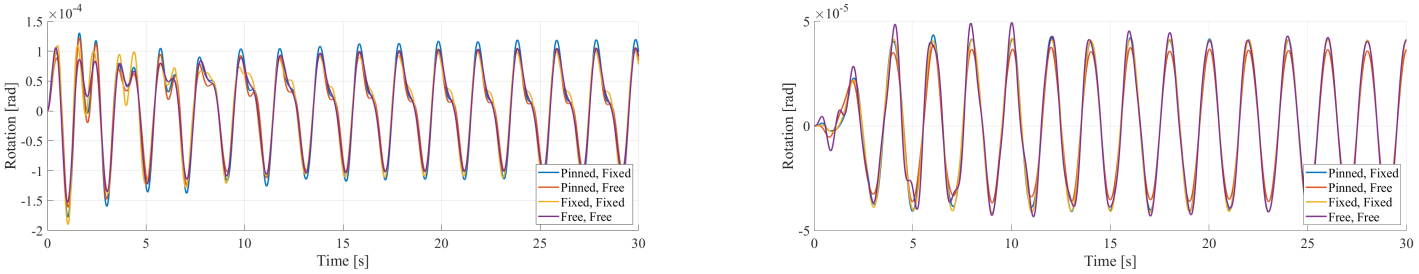

(a) Load case 1.1 (b) Load case 2.2

Figure 9.10: Influence of the boundary conditions in φ direction at midspan

As the location of interest approaches to the endpoint of the tunnel, the influence of different the boundary conditions becomes stronger. This can be observed in Figure 9.11, Figure 9.12 and Figure 9.13, where the models based on different boundary conditions give different results. The both end free beam & both end free torsion rod model (denoted as Free, Free) gives the weakest boundary conditions. The absolute maximum response of this boundary conditions is generally two to three times bigger than the other. On the contrary, the displacement results from the both end fixed beam & both end fixed torsion rod model (denoted as Fixed, Fixed) is limited to a relatively small value. It is worth noting that the change of the boundary condition regarding to rotational angle does not influence the displacement in horizontal and vertical direction, which can be seen in Figure 9.11 and Figure 9.12 where the blue path and the red path coincides almost exactly with each other.

For a global view of results of the influence of the boundary conditions of the tunnel, refer to Appendix C.

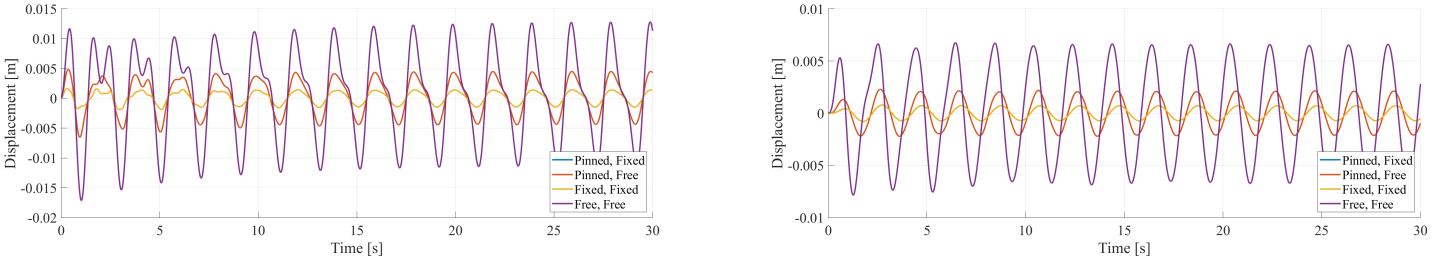

(a) Load case 1.1 (b) Load case 2.2

Figure 9.11: Influence of the boundary conditions in y direction at 1.5 m from the tunnel bow

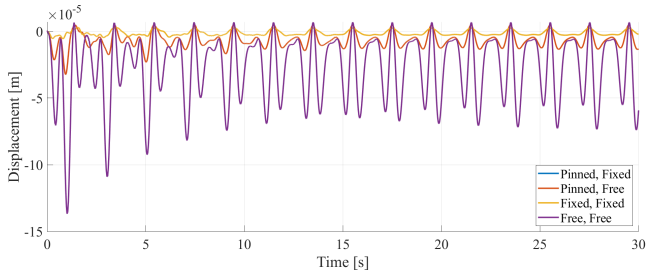

(a) Load case 1.1

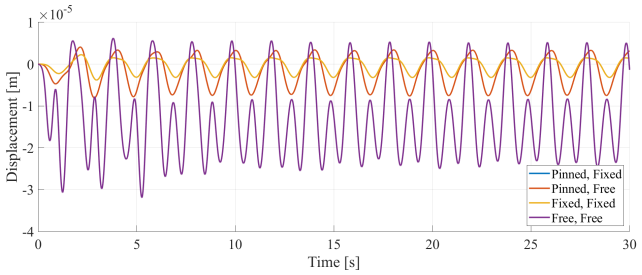

(b) Load case 2.2

Figure 9.12: Influence of the boundary conditions in z direction at 1.5 m from the tunnel bow

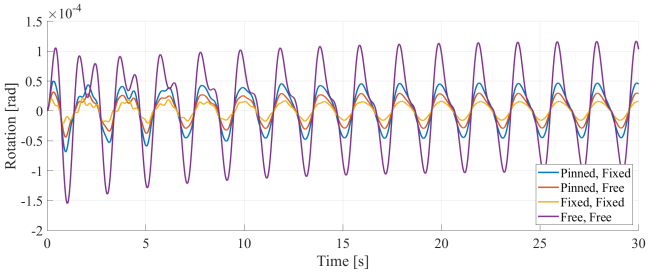

(a) Load case 1.1

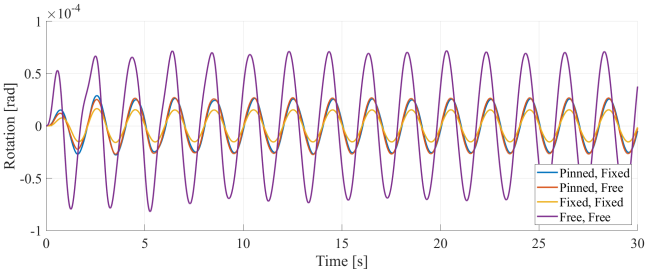

(b) Load case 2.2

Figure 9.13: Influence of the boundary conditions in φ direction at 1.5 m from the tunnel bow

9.7. Conclusion

Some conclusions are drawn based on the results of the parametric study. These conclusions provide a further understanding of the dynamic behaviour of the SFT. It is worth noting that these conclusions are based on the certain structural and geometrical parameters of the scaled model. It is possible to get the similar conclusions when the model is scaled to full scale dimensions. However, the conclusion may change when other sets of parameters are applied, since some of the relations between the parameters and the response of the tunnel are not linear.

In brief, following methods can be applied to reduce the maximum response of the SFT:

- Increase or decrease the buoyancy weight ratio in order to make the value of the maximum response move to the troughs of the curves as shown in Figure 9.1 .
- Choose a certain length of the tunnel so that the natural frequencies of the structure are away from the expected loading frequencies. In full scale, if the tunnel is longer than 3000m, the length of the tunnel makes no more difference to the response.
- Choose the value at troughs of Figure 9.3 or Figure 9.5 for the stiffness of vertical and inclined cables.
- Apply the inclined cables with an inclination of 35° to 45°.
- Assign more net buoyancy force to the inclined cables.
- For long SFTs, the boundary conditions do not influence much to the response at the midspan. Given that the maximum response usually takes place at midspan, The boundary conditions do not influence much to the maximum response of the tunnel.

IV

Conclusion

10

Conclusion and recommendations

The conclusions and the recommendations for the complete research are presented in this chapter. The research questions are answered in section 10.1 and the recommendations for further research are discussed in section 10.2.

10.1. Conclusion

The research questions are introduced in chapter 1. These questions must be answered to fulfill the research objective: to gain insight on the global dynamic fluid-structure interaction response of a submerged floating tunnel under wave and current loading to enhance a design of a SFT. The research questions are broken down into sub-questions in order to specify them. First, the sub-questions are discussed to answer the research questions in the end.

10.1.1. Sub-questions

1. *How can the global dynamic fluid-structure interaction response of a SFT with a discrete anchoring system be modeled?*

   The following concepts are used to model the dynamic response of a SFT with a discrete anchoring system:

   - A SFT can be schematized with :
     - Euler-Bernoulli beam
     - Beam on elastic foundation assumption

     This model is suitable to access the response of the tunnel subjected to a uniform current and/or long-period perpendicular or oblique waves.
   - The anchoring system can be taken into account by:
     - Geometrically linear assumption
     - Geometrically nonlinear assumption

     A linear analysis is suitable when only horizontal and rotational directions are of interest. A geometrically nonlinear assumption will be necessary for accurate analysis in vertical direction if the second order effect is considered. Also, a nonlinear assumption is needed if one wants to include the influence of the BWR in the analysis.
   - The fluid-structure interaction is considered in the governing equation by:
     - Morison equation
     - Wake oscillator model

     It is suggested that Morison equations can be used as long as the diameter of the tunnel is much smaller than the wavelength. Wake oscillator model is suitable when the reduced velocity is larger than 5.

- The dynamic response is calculated with a modal domain approach in which:
  - The partial differential equations are transformed into ordinary differential equations by applying a modal analysis
  - The ordinary differential equations are solved by a Runge-Kutta method provided by MATLAB®

  This approach takes significantly less time than the finite element method. However, the convergence of the numerical solver needs to be treated carefully.

2. *How does the stiffness of the anchoring system considering geometrical nonlinearity influence the results?*

   The stiffness of the anchoring system considering geometrical nonlinearity is determined by the motions in three directions together and in return couples these motions by the restoring forces. It leads to the fact that the frequency content of the vertical motion becomes more complicated, since the frequencies of the motion in the horizontal and rotational direction are imprinted in the vertical direction. It also captures the pendulum phenomenon so that the vertical displacement results from a nonlinear stiffness model could be 5 times bigger than the one from a linear stiffness model. This difference decreases as the attack angle change from 90° to 45°.

3. *How does the global dynamic analysis influence the results?*

   The results of a global dynamic analysis is significantly different from a 2D cross-sectional analysis when the SFT is subjected to the oblique wave loading, since the 2D cross-sectional analysis is not capable to capture the longitudinal behaviour of the response. Therefore, when a SFT is expected to be subjected to oblique wave loadings, a global dynamic analysis is suggested.

4. *How do the geometrical and structural design parameters influence the dynamic response of a SFT?*

   Basically, increase of the BWR or increase of the stiffness in the cables can reduce the maximum response of the SFT. On the contrary, decrease of the tunnel length, decrease of the inclination of the inclined cables or decrease of the distribution of the net buoyancy leads to a lower magnitude of the maximum response. However, the relation between the design parameters and the maximum response is not monotonic. Therefore, these properties vary depending on specific circumstances.

10.1.2. Main questions

1. *What is the global dynamic fluid-structure interaction response of the SFT under wave and current loading?*

   The global dynamic response under wave and current can be divided into three categories:

   - Combined wave and current loading:
     - The wave loading have main impact on the dynamic response.
     - The current loading acts as an static loading on the system.
   - Pure wave loading to study the influence of oblique loading:
     - The most severe attack angle is 90°, i.e. the loading direction is perpendicular to the tunnel axis.
     - The transient state of the response is shorter when the tunnel is loaded in oblique manner.
   - Pure current loading to study the influence of vortex-induced vibration (VIV):
     - The imprinted natural frequencies generated from horizontal motion observed in vertical motion is not related to the VIV
     - Based on the scaled model, the VIV of the tunnel tube is negligible.

2. *Which parameters can be used to reduce the dynamic response of a SFT?*

   The most effective approach to reducing the dynamic response of a SFT is to avoid resonance and to keep the magnitude of maximum response as low as possible. The former can be achieved

by changing the stiffness of the cables or the value of the BWR. The latter can be accomplished by choosing a suitable inclination angle and pretension distribution coefficient at least four cables are applied.

10.2. Recommendations

Recommendations for future research are addressed in this section. These recommendations are divided into two parts. First, some recommendations are presented to validate and improve the performance and accuracy of the current model, which concerns the extension to investigate additional aspects of a SFT. Second, some recommendations are provided for future application of the model. Namely, by using the current model, further analysis to investigate additional relevant aspects of a SFT is suggested.

10.2.1. Recommendations to validate and improve the current model

- A validation is required to determine the accuracy of the model. The case study in this research is base on a scaled SFT physical model which can be used for further validation. The measurement data are not available at this time.
- This research simplifies the tunnel as an Euler-Bernoulli beam on elastic foundation which is not able to account for shear deformations and longitudinal deformations. It is advised to use Timoshenko beam combined with tensile bar for future simulations. Furthermore, the effect of the discrete anchoring system is neglected. This effect can be captured by upgrading the model with beam on elastic spring assumption.
- Structural damping is not included in the model, which can be considered to improve the model by assuming to be proportional to Rayleigh damping. However, this damping is expected to be relatively small compared to the hydrodynamics damping.
- It is suggested to introduce a more accurate model for anchoring system considering the slack of the cables at a certain state. With this model, the influence of the extreme loading conditions on the SFT can be investigated.

10.2.2. Recommendations for application of the model

- A complete irregular wave analysis would be of interest to compare with the regular wave analysis, which is based on the significant wave height and peak period.
- It is suggested to study the wave loading characterised by a higher frequency content, since a higher frequency content may fall in the same range of the system natural frequencies. Morison equation is not applicable in this case. The use of the diffraction hydrodynamic theory will be then necessary as the structure will become a large structure with respect to the wavelength of the sea state.
- The velocity and the acceleration responses of the SFT and the stress in the tunnel cross section and cables are also of practical interest. The current model is able to generate the velocity and the acceleration response data for further study. The stress in the tunnel cross section and cables can be derived based on the displacement of the tunnel.
- Based on the scaled model, the vortex induced vibration of the tunnel is proved unlikely to happen. However, as the free-span between two groups of anchoring cables increases or the stiffness in the vertical direction becomes decreases, the stiffness in z-direction becomes small, which would make the natural frequency close to the loading frequency. For this reason, the VIV is expected to take place and further analysis is needed. Additionally, the possibility of the VIV of the cables is relatively high. The VIV of the cables could have an impact on the tunnel, which causes an interaction between the cables and the tunnel. It would be interesting to upgrade the nonlinear stiffness model to capture this interaction.
- A local failure such as a broken cable may have impact on the global response. It would be interesting for future analysis to cover this aspect.

Bibliography

ABS (1999). *Guidance notes on the application of synthetic ropes for offshore mooring*. American Bureau of Shipping.

Achenbach, E. and Heinecke, E. (1981). On vortex shedding from smooth and rough cylinders in the range of reynolds numbers 6× 10 3 to 5× 10 6. *Journal of fluid mechanics*, 109:239–251.

API, R. (2002). 2A-WSD Recommended Practice for planning, designing and Constructing Fixed Offshore Platforms–Working Stress Design, December 2000. *Errata and supplement*, 1.

Barltrop, N. D. (1998). *Floating Structures: a guide for design and analysis*, volume 1. Oilfield Publications Incorporated.

Blevins, R. D. (1977). Flow-induced vibration. *New York, Van Nostrand Reinhold Co., 1977. 377 p.*

Brancaleoni, F., Castellani, A., and D'Asdia, P. (1989). The response of submerged tunnels to their environment. *Engineering Structures*.

Chaplin, J. R. (1984). Nonlinear forces on a horizontal cylinder beneath waves. *Journal of Fluid Mechanics*, 147:449–464.

Dormand, J. R. and Prince, P. J. (1980). A family of embedded runge-kutta formulae. *Journal of computational and applied mathematics*, 6(1):19–26.

Faggiano, B., Landolfo, R., and Mazzolani, F. (2005). The sft: an innovative solution for waterway strait crossings. In *IABSE Symposium Report*, volume 90, pages 36–42. International Association for Bridge and Structural Engineering.

Fang, H. and Duan, M. (2014). Chapter 1 - the environment and environmental load of offshore oil engineering. In Fang, H. and Duan, M., editors, *Offshore Operation Facilities*, pages 1 – 140. Gulf Professional Publishing, Boston.

FEHRL (Forum of European National Highway Research Laboratories) (1996). "Analysis of the submerged floating tunnel concept". *FEHRL report no. 1996/2a*.

Flory, J. F., Banfield, S. P., Petruska, D. J., et al. (2004). Defining, measuring, and calculating the properties of fiber rope deepwater mooring lines. In *Offshore Technology Conference*. Offshore Technology Conference.

Gabbai, R. and Benaroya, H. (2005). An overview of modeling and experiments of vortex-induced vibration of circular cylinders. *Journal of Sound and Vibration*, 282(3-5):575–616.

Grantz, W. C. (1997). Steel-shell immersed tunnels—forty years of experience. *Tunnelling and Underground Space Technology*, 12(1):23–31.

Grantz, W. C. (2003). A new concept for a steel shell submerged floating tunnel. In *Reclaiming the Underground Space (2 Volume Set): Proceedings of the ITA World Tunneling Congress, Amsterdam 2003.*, page 297. CRC Press.

Holthuijsen, L. H. (2010). *Waves in oceanic and coastal waters*. Cambridge university press.

Konda, N., Arimochi, K., Hirota, K., Watanabe, E., Tada, M., Kitada, H., Fukui, T., Yamamoto, M., Kho, Y., and Yajima, H. (2003). Development of structural steel with superior resistance against fatigue crack growth. In *ASME 2003 22nd International Conference on Offshore Mechanics and Arctic Engineering*, pages 35–44. American Society of Mechanical Engineers.

Kunisu, H., Mizuno, S., Mizuno, Y., Yamasita, T., and Saeki, H. (1994). Numerical analysis of wave force and dynamic response to the submerged floating tunnels. In *Proc 3rd Symp on Strait Crossings*, pages 637–44.

Laitone, E. (1962). Limiting conditions for cnoidal and stokes waves. *Journal of Geophysical Research*, 67(4):1555–1564.

Maeda, N., Morikawa, M., Ishikawa, K., and Kakuta, Y. (1994). Study on structural characteristics of support systems for submerged floating tunnel. In *Proc. of the 3rd Symposium on Strait Crossing*.

Martire, G. (2010). The Development of Submerged Floating Tunnels As an Innovative Solution for Waterway Crossings.

Nagai, Y., Fukami, H., Inoue, H., Nakashima, T., Kojima, A., Kajitani, T., Adachi, T., and Yoshida, Y. (2003). Production of high-strength and high-toughness steel for offshore structures. In *ASME 2003 22nd International Conference on Offshore Mechanics and Arctic Engineering*, pages 319–325. American Society of Mechanical Engineers.

Ogink, R. and Metrikine, A. (2010). A wake oscillator with frequency dependent coupling for the modeling of vortex-induced vibration. *Journal of Sound and Vibration*, 329(26):5452–5473.

Olhede, S. C. and Walden, A. T. (2002). Generalized morse wavelets. *IEEE Transactions on Signal Processing*, 50(11):2661–2670.

Patel, M. H. and Witz, J. A. (2013). *Compliant offshore structures*. Butterworth-Heinemann.

Peregrine, D. H. (1972). Equations for water waves and the approximations behind them. *Waves on beaches and resulting sediment transport*, pages 95–121.

Sarpkaya, T. (1976). Vortex shedding and resistance in harmonic flow about smooth and rough circular cylinders at high reynolds numbers. Technical report, NAVAL POSTGRADUATE SCHOOL MONTEREY CA.

Sarpkaya, T. (2010). *Wave forces on offshore structures*. Cambridge university press.

Sarpkaya, T. and Isaacson, M. (1981). Mechanics of wave forces on offshore structures.

Shampine, L. F. and Reichelt, M. W. (1997). The matlab ode suite. *SIAM journal on scientific computing*, 18(1):1–22.

Spijkers, J., Vrouwenvelder, A., and Klaver, E. (2006). *Dynamics of Structures Part 1 Vibration of Structures*. VSSD.

V

Appendices

A

Behaviour of the linear and nonlinear stiffness model

A.1. The restoring forces due to the horizontal displacement

To investigate the influence of the horizontal displacement, the vertical displacement and the rotational angle are set as $\Delta z = -1.6500 \cdot 10^{-4}$ m and $\Delta\varphi = -1.6500 \cdot 10^{-4}$ rad, respectively.

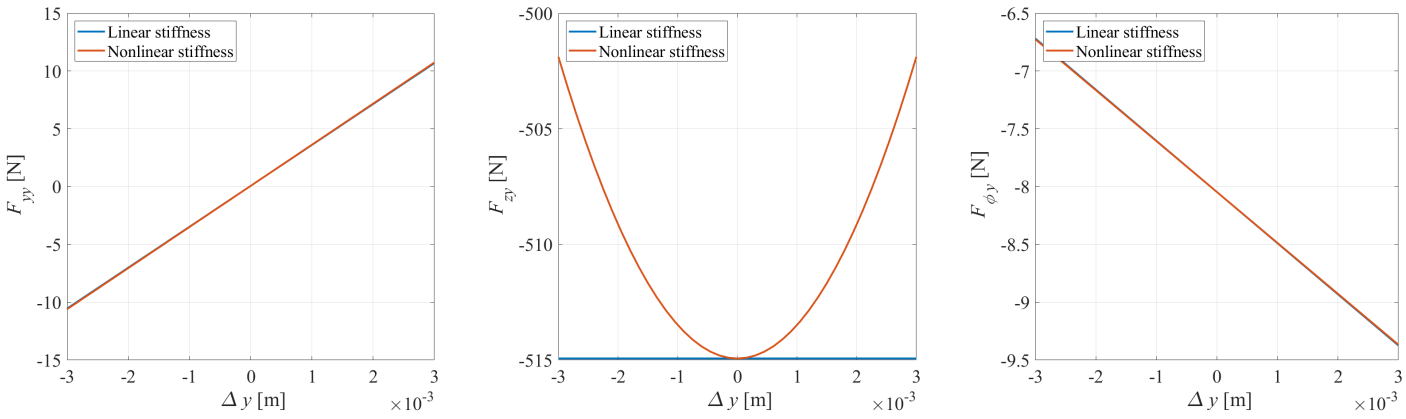

(a) y-direction (b) z-direction (c) φ-direction

Figure A.1: Restoring forces VS horizontal displacement

A.2. The restoring forces due to the vertical displacement

To investigate the influence of the vertical displacement, the horizontal displacement and the rotational angle are set as $\Delta y = -0.0017$ m and $\Delta\varphi = -1.6500 \cdot 10^{-4}$ rad, respectively

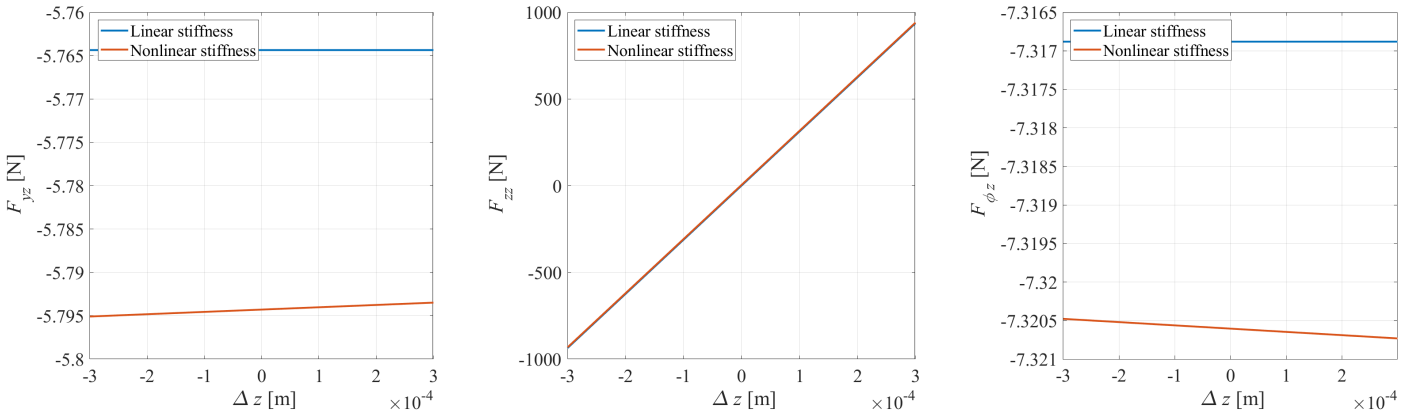

(a) y-direction (b) z-direction (c) φ-direction

Figure A.2: Restoring forces VS vertical displacement

A.3. The restoring forces due to the rotational angle

To investigate the influence of the rotational angle, the horizontal displacement and the vertical displacement are set as $\Delta y = -0.0017$ m and $\Delta z = -1.6500 \cdot 10^{-4}$ m, respectively

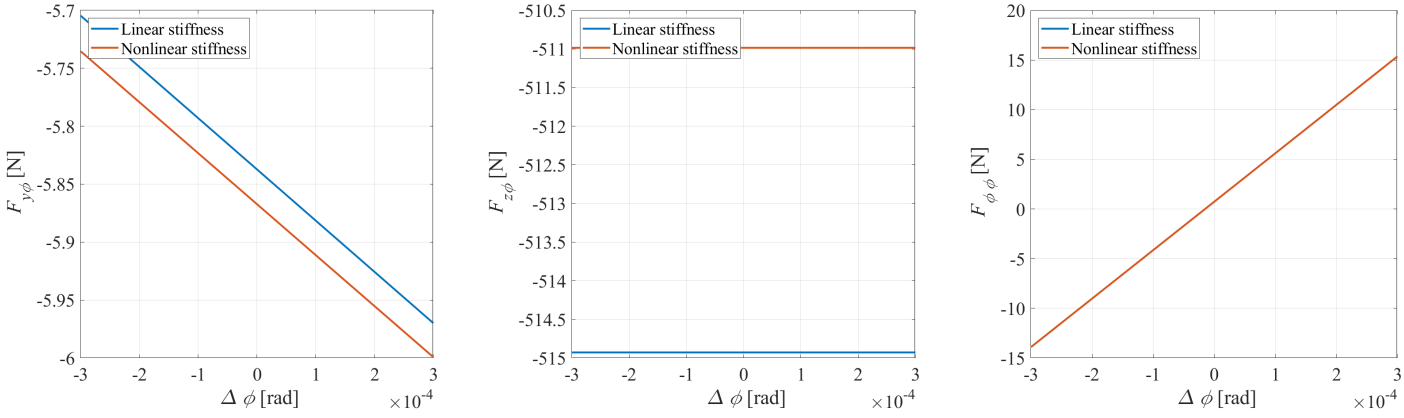

(a) y-direction (b) z-direction (c) φ-direction

Figure A.3: Restoring forces VS rotational angle

B

Results of load cases in 3D

B.1. Load group 1

These results are based on **Model A** (Equation 6.6) and **Model B**(Equation 6.7).

Load case 1.1

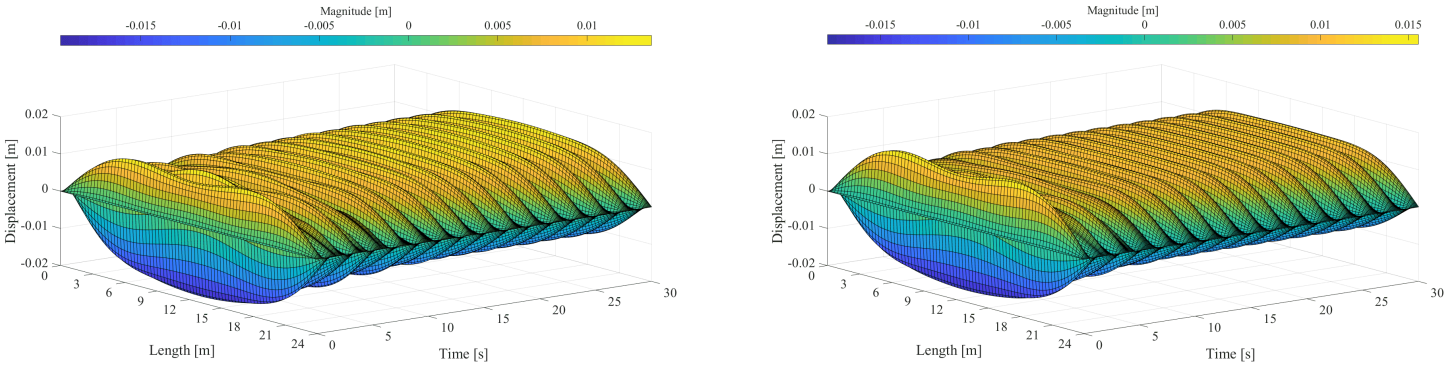

(a) Linear stiffness model

(b) Nonlinear stiffness model

Figure B.1: Displacement in y-direction (Load case 1.1)

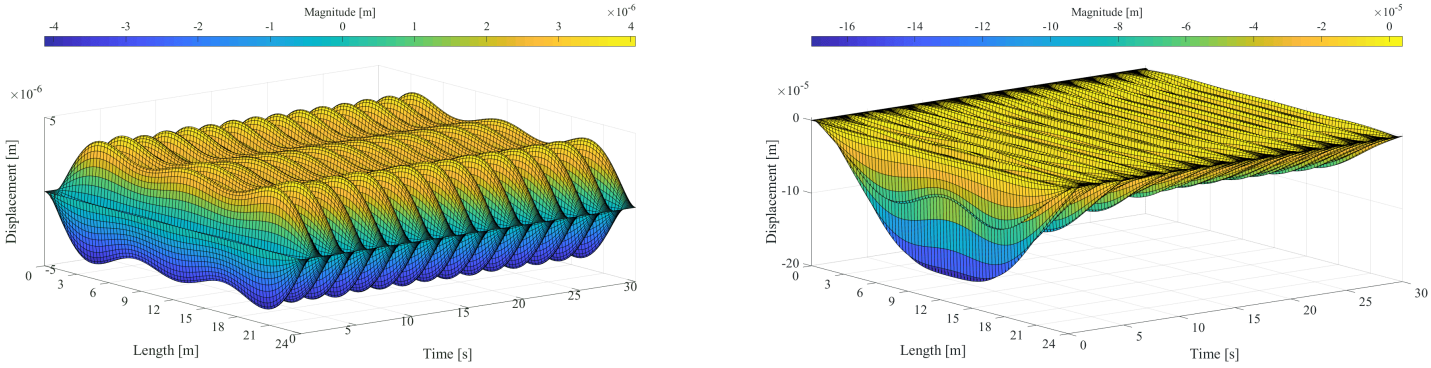

(a) Linear stiffness model

(b) Nonlinear stiffness model

Figure B.2: Displacement in z-direction (Load case 1.1)

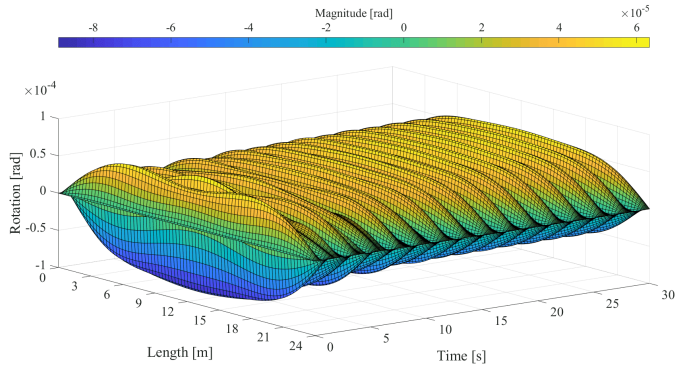

(a) Linear stiffness model

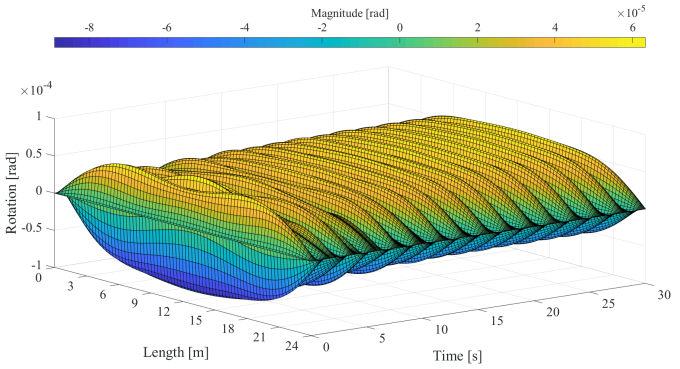

(b) Nonlinear stiffness model

Figure B.3: Rotation in φ-direction (Load case 1.1)

Load case 1.2

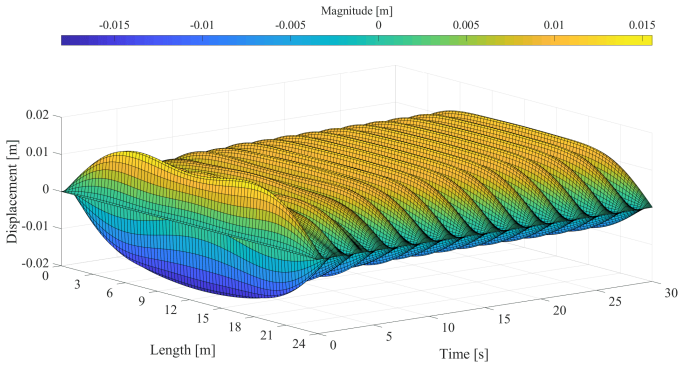

(a) Linear stiffness model

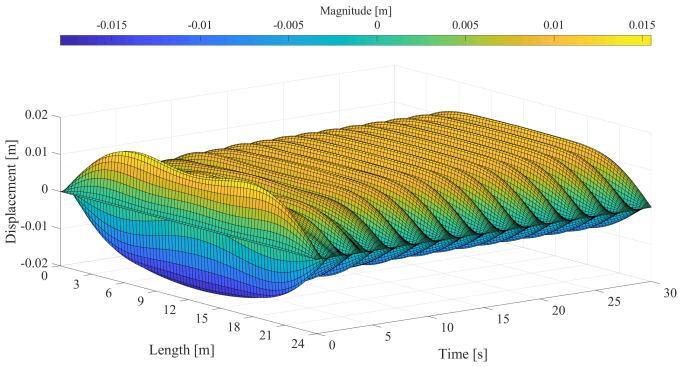

(b) Nonlinear stiffness model

Figure B.4: Displacement in y-direction (Load case 1.2)

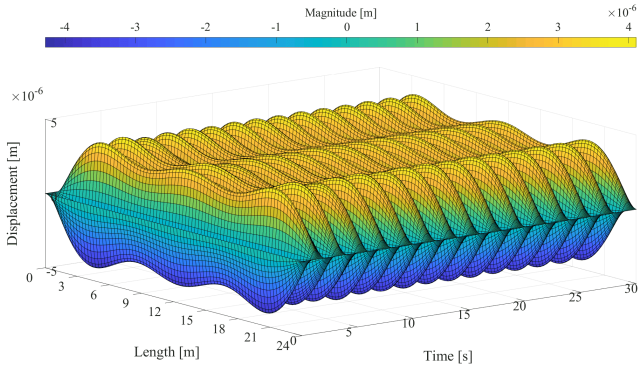

(a) Linear stiffness model

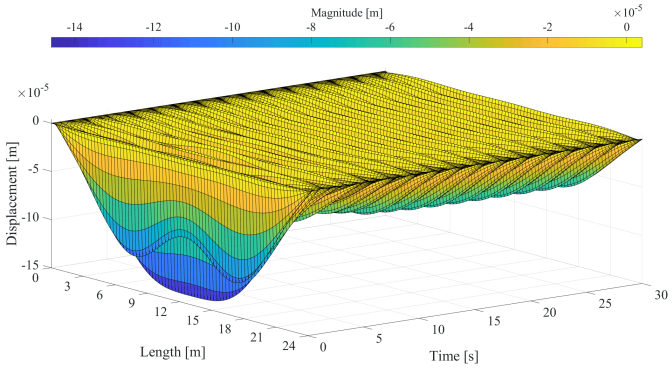

(b) Nonlinear stiffness model

Figure B.5: Displacement in z-direction (Load case 1.2)

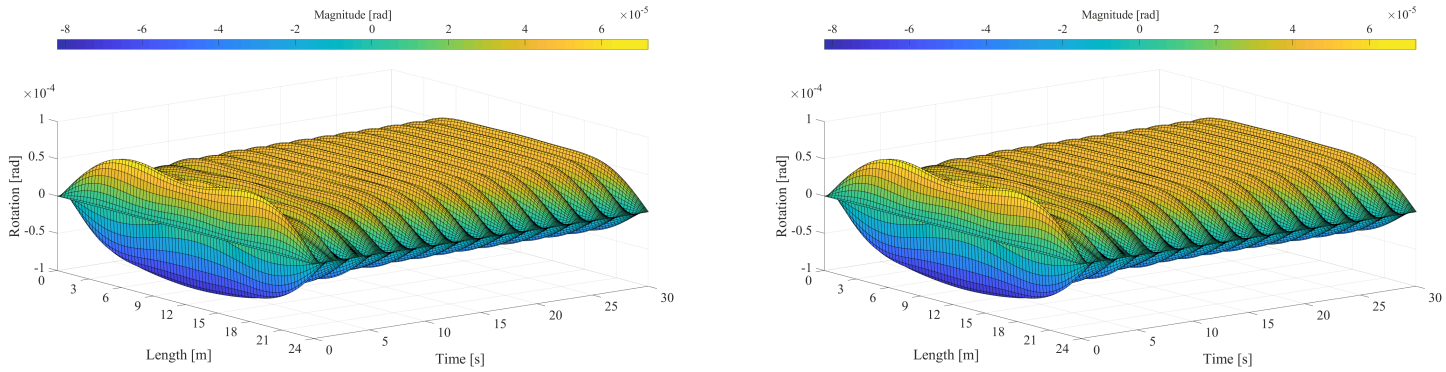

(a) Linear stiffness model

(b) Nonlinear stiffness model

Figure B.6: Rotation in φ-direction (Load case 1.2)

Load case 1.3

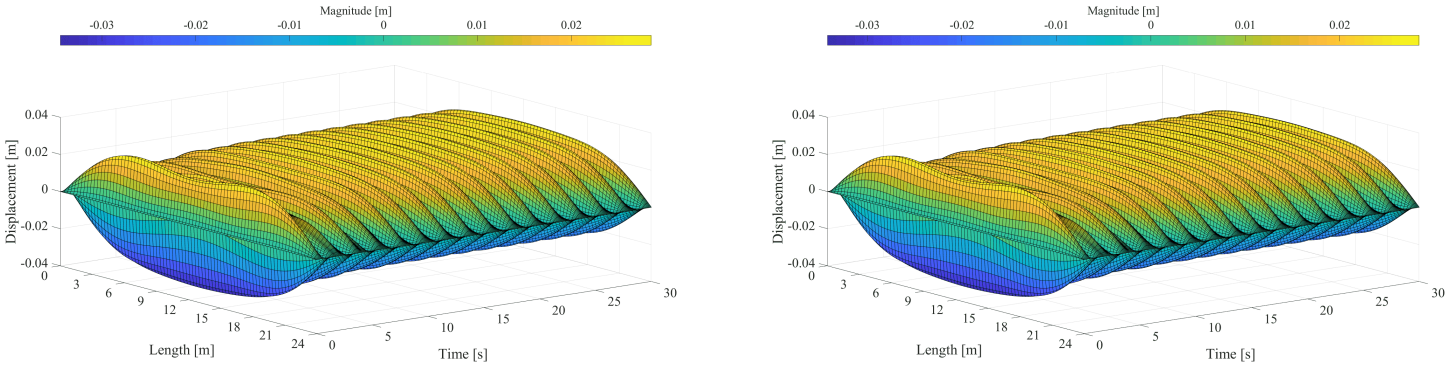

(a) Linear stiffness model

(b) Nonlinear stiffness model

Figure B.7: Displacement in y-direction (Load case 1.3)

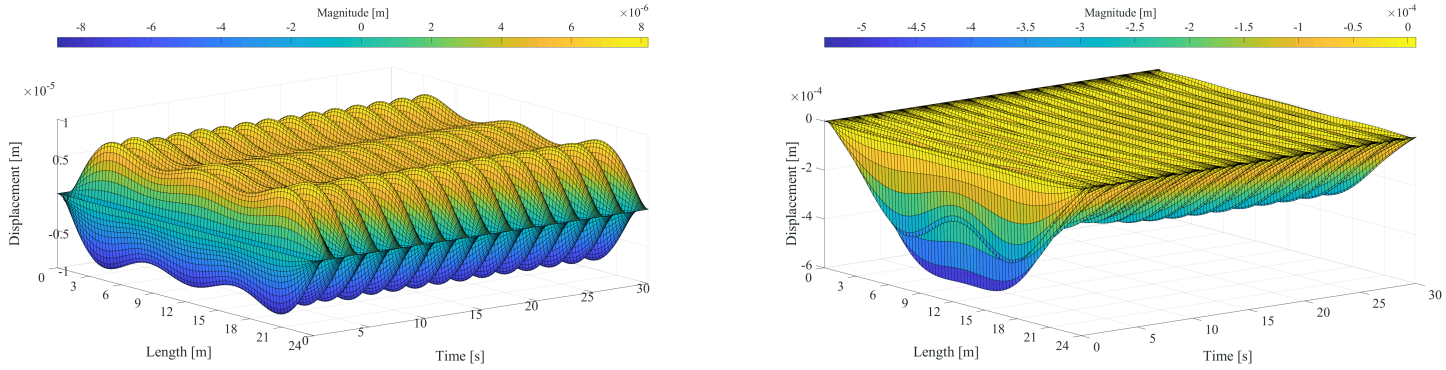

(a) Linear stiffness model

(b) Nonlinear stiffness model

Figure B.8: Displacement in z-direction (Load case 1.3)

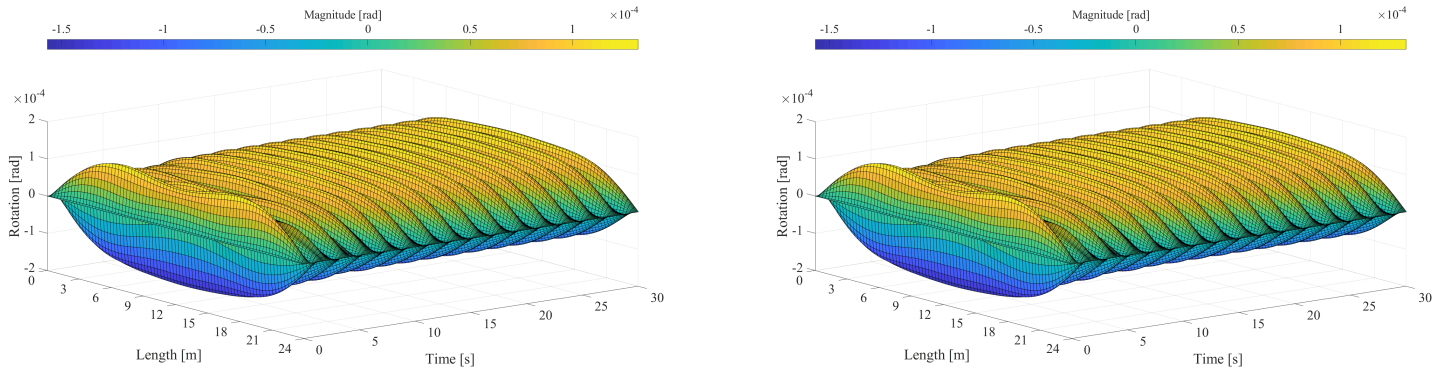

(a) Linear stiffness model (b) Nonlinear stiffness model

Figure B.9: Rotation in φ-direction (Load case 1.3)

B.2. Load group 2

These results are based on **Model A** (Equation 6.6) and **Model B**(Equation 6.7).

Load case 2.1

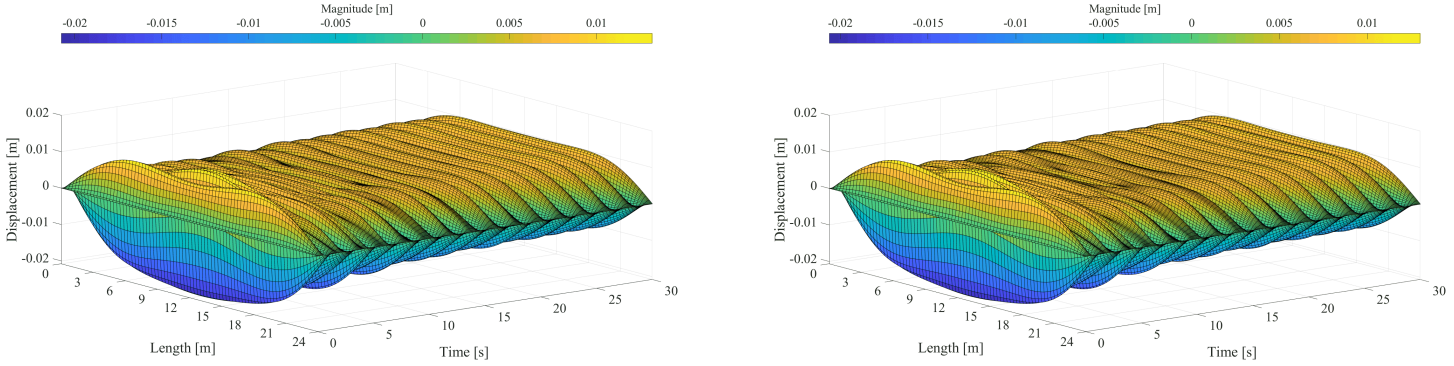

(a) Linear stiffness model (b) Nonlinear stiffness model

Figure B.10: Displacement in y-direction (Load case 2.1)

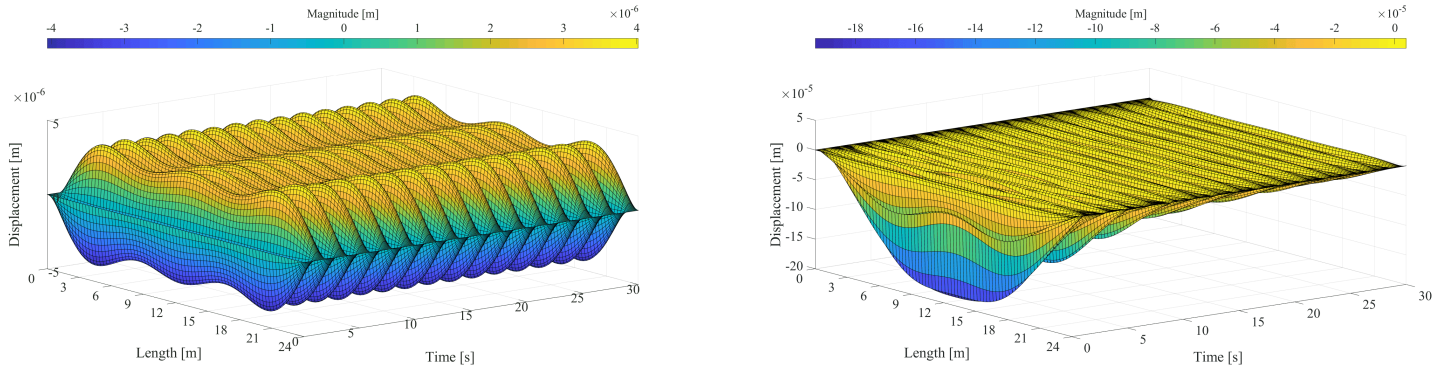

(a) Linear stiffness model (b) Nonlinear stiffness model

Figure B.11: Displacement in z-direction (Load case 2.1)

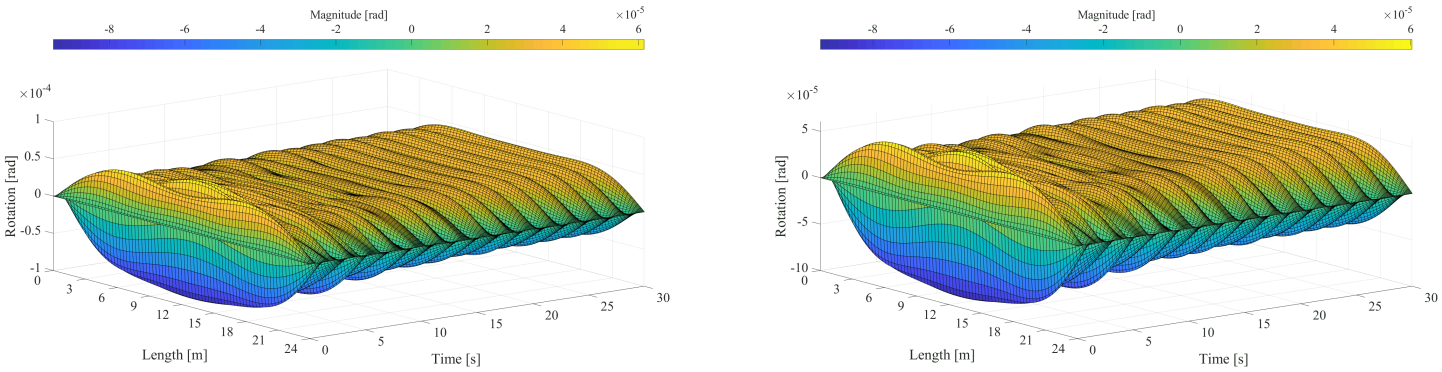

(a) Linear stiffness model

(b) Nonlinear stiffness model

Figure B.12: Rotation in φ-direction (Load case 2.1)

Load case 2.2

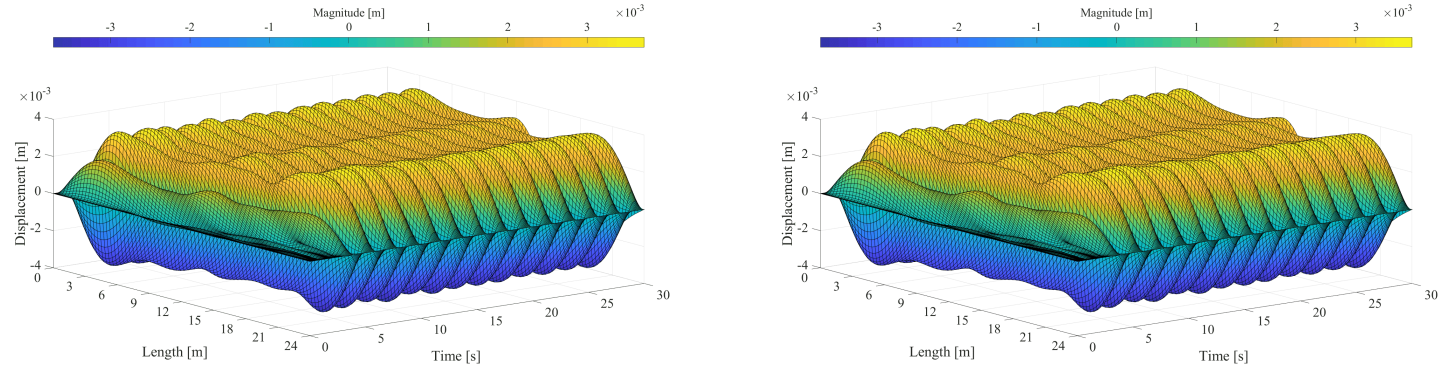

(a) Linear stiffness model

(b) Nonlinear stiffness model

Figure B.13: Displacement in y-direction (Load case 2.2)

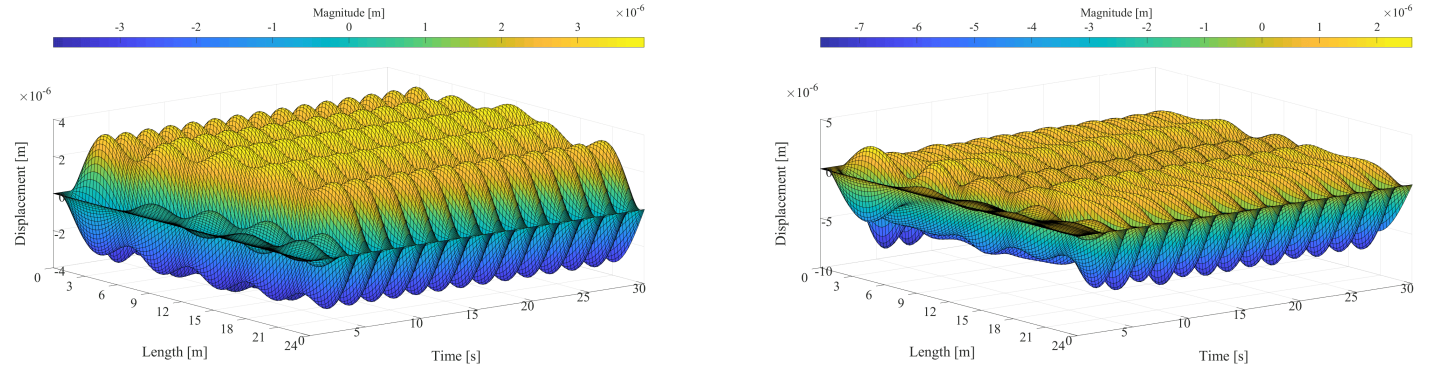

(a) Linear stiffness model

(b) Nonlinear stiffness model

Figure B.14: Displacement in z-direction (Load case 2.2)

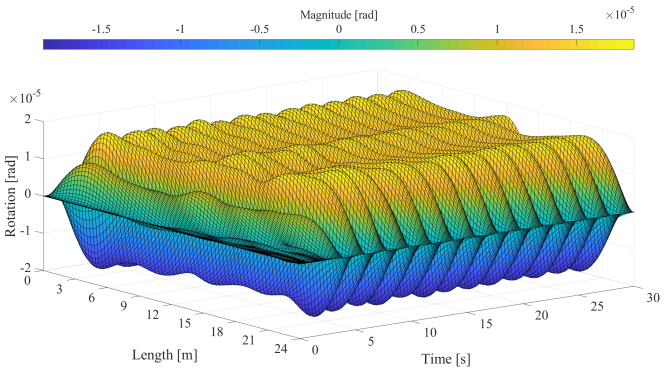

(a) Linear stiffness model

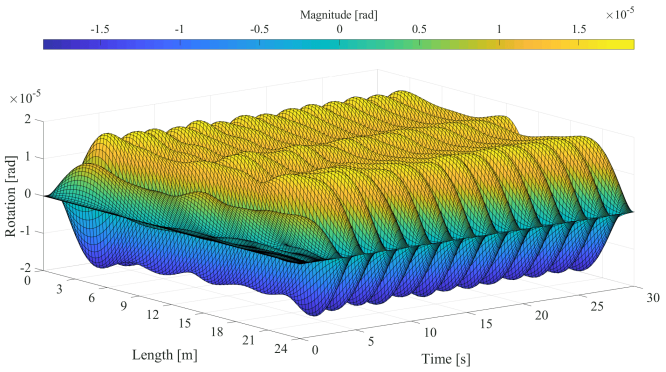

(b) Nonlinear stiffness model

Figure B.15: Rotation in φ-direction (Load case 2.2)

Load case 2.3

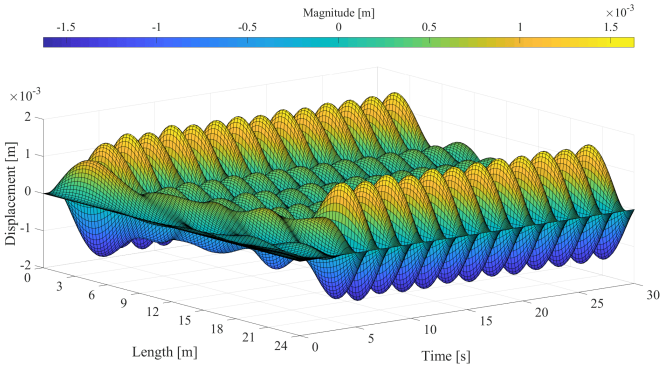

(a) Linear stiffness model

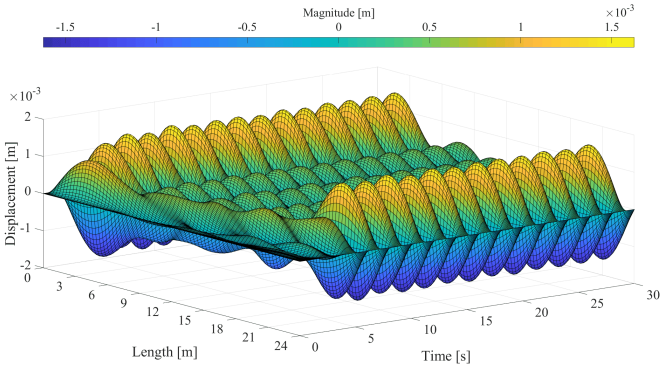

(b) Nonlinear stiffness model

Figure B.16: Displacement in y-direction (Load case 2.3)

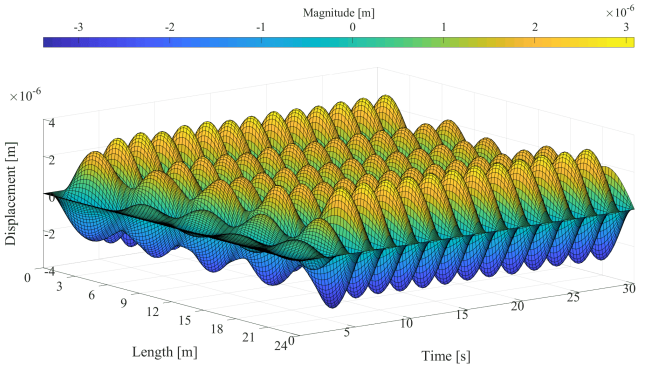

(a) Linear stiffness model

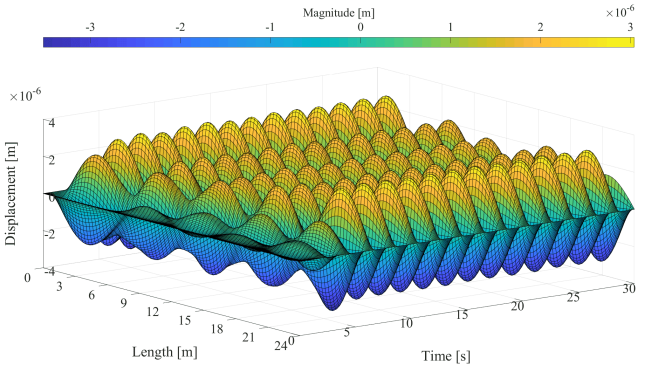

(b) Nonlinear stiffness model

Figure B.17: Displacement in z-direction (Load case 2.3)

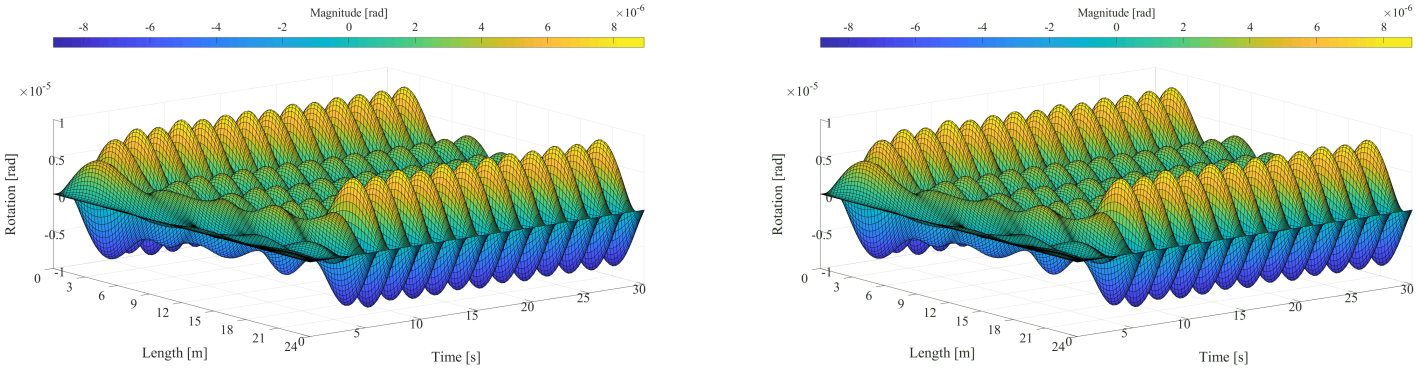

(a) Linear stiffness model

(b) Nonlinear stiffness model

Figure B.18: Rotation in φ-direction (Load case 2.3)

B.3. Load group 3

These results are based on **Model C** (Equation 6.8) and **Model D**(Equation 6.9).

Load case 3.1

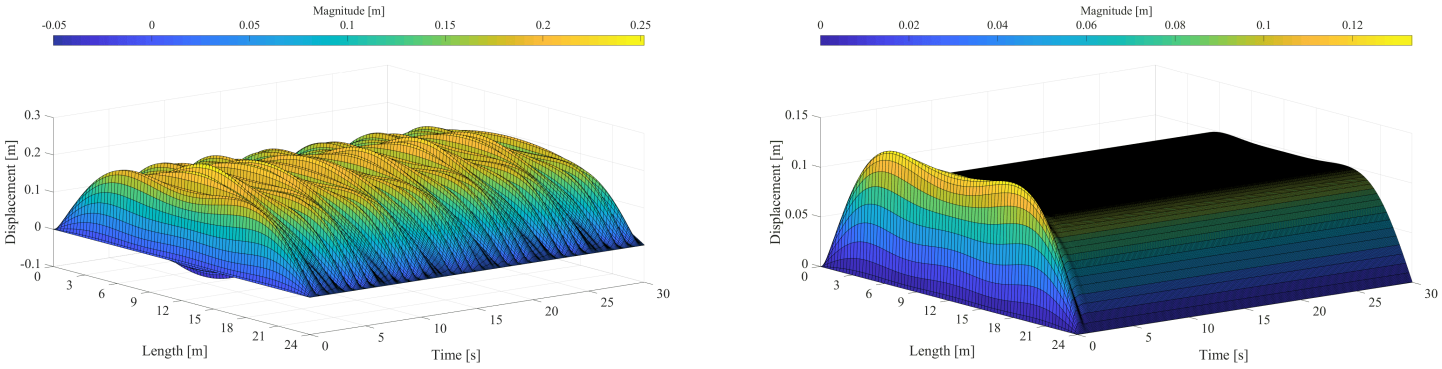

(a) With simplified wake oscillator

(b) With non-simplified wake oscillator

Figure B.19: Displacement in y-direction (Load case 3.1)

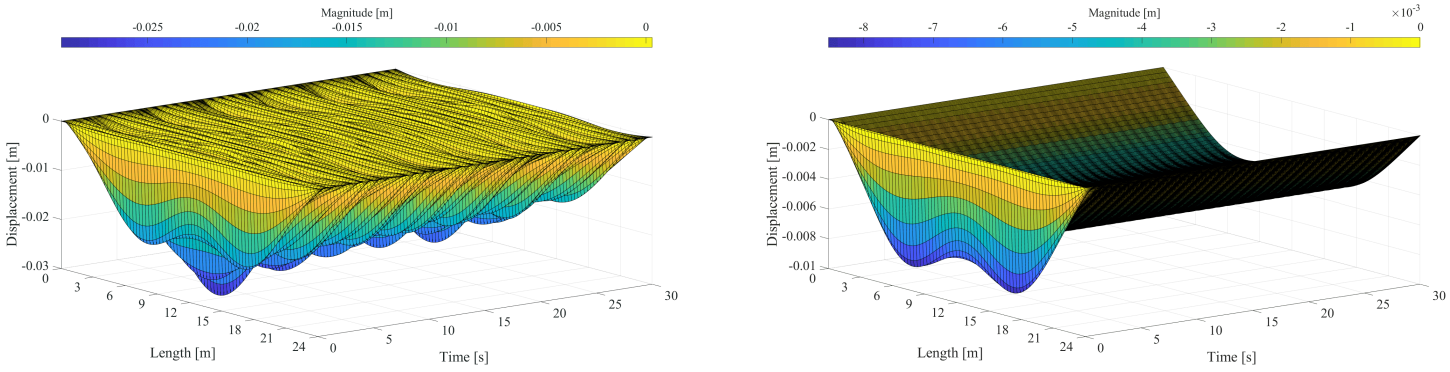

(a) With simplified wake oscillator

(b) With non-simplified wake oscillator

Figure B.20: Displacement in z-direction (Load case 3.1)

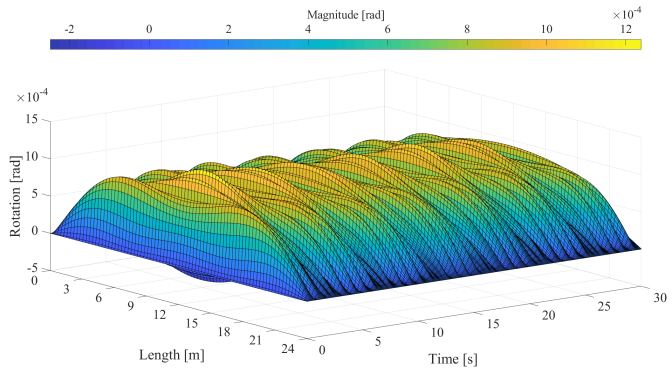

(a) With simplified wake oscillator

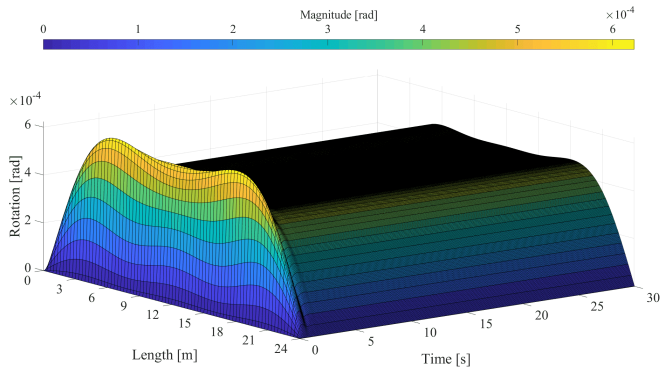

(b) With non-simplified wake oscillator

Figure B.21: Rotation in φ-direction (Load case 3.1)

Load case 3.2

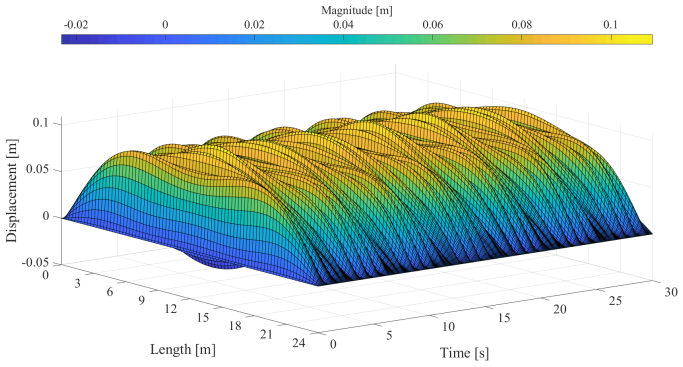

(a) With simplified wake oscillator

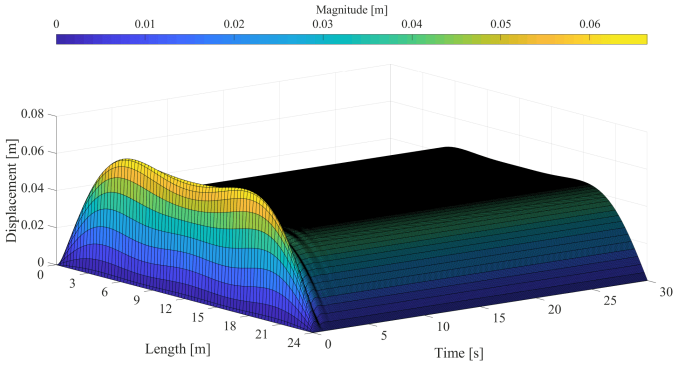

(b) With non-simplified wake oscillator

Figure B.22: Displacement in y-direction (Load case 3.2)

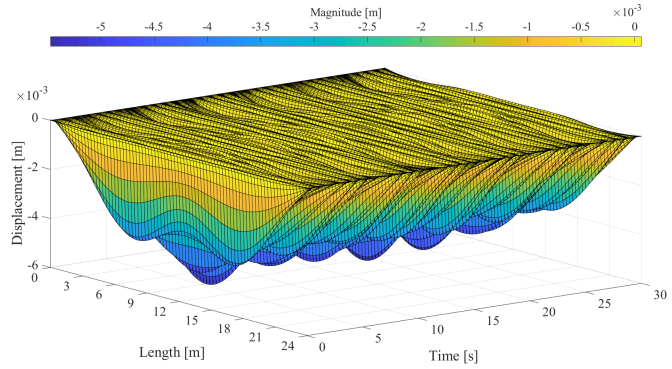

(a) With simplified wake oscillator

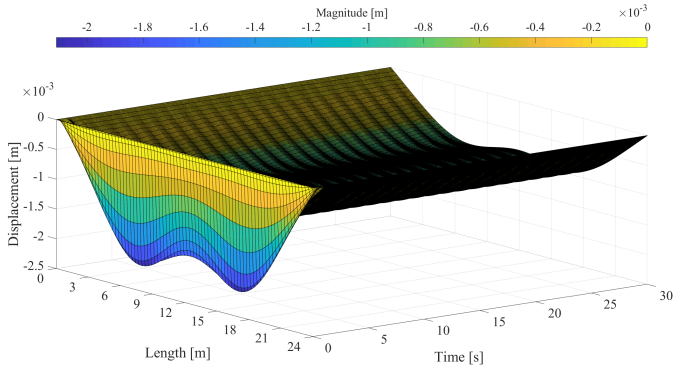

(b) With non-simplified wake oscillator

Figure B.23: Displacement in z-direction (Load case 3.2)

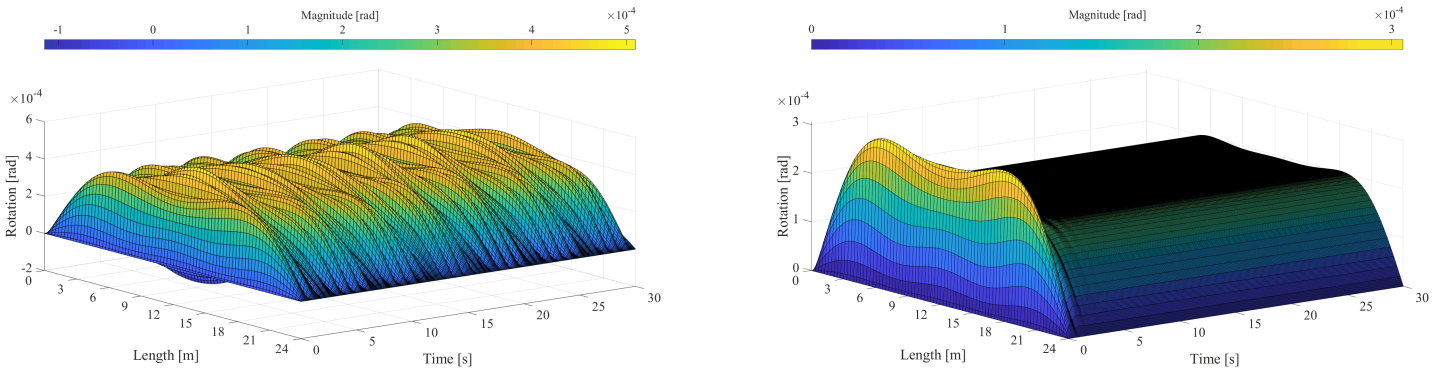

(a) With simplified wake oscillator

(b) With non-simplified wake oscillator

Figure B.24: Rotation in φ-direction (Load case 3.2)

C

Results of influence of the boundary conditions in 3D

These results are based on **Model B**(Equation 6.7).

C.1. Both end pinned beam & both end fixed torsion rod

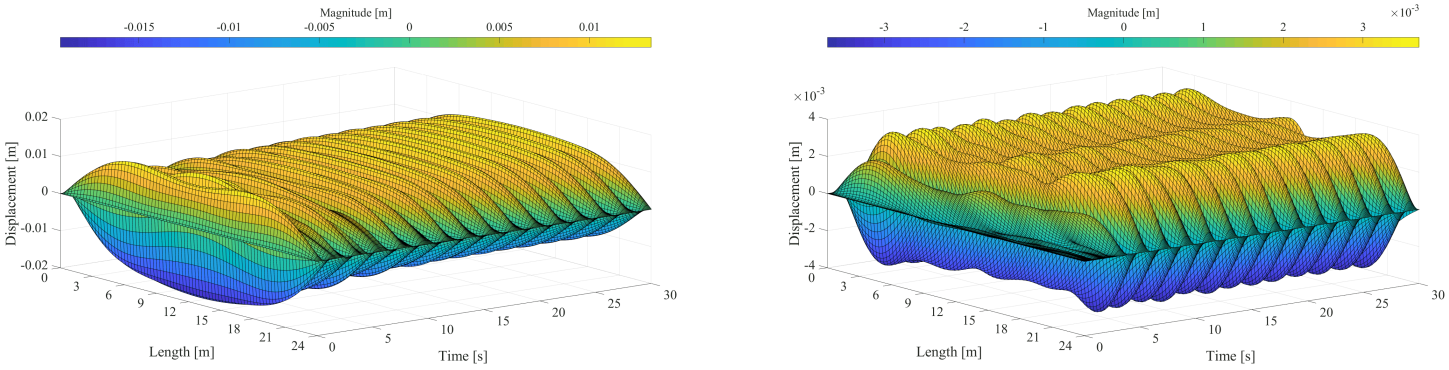

(a) Load case 1.1

(b) Load case 2.2

Figure C.1: Displacement in y-direction (Pinned, Fixed)

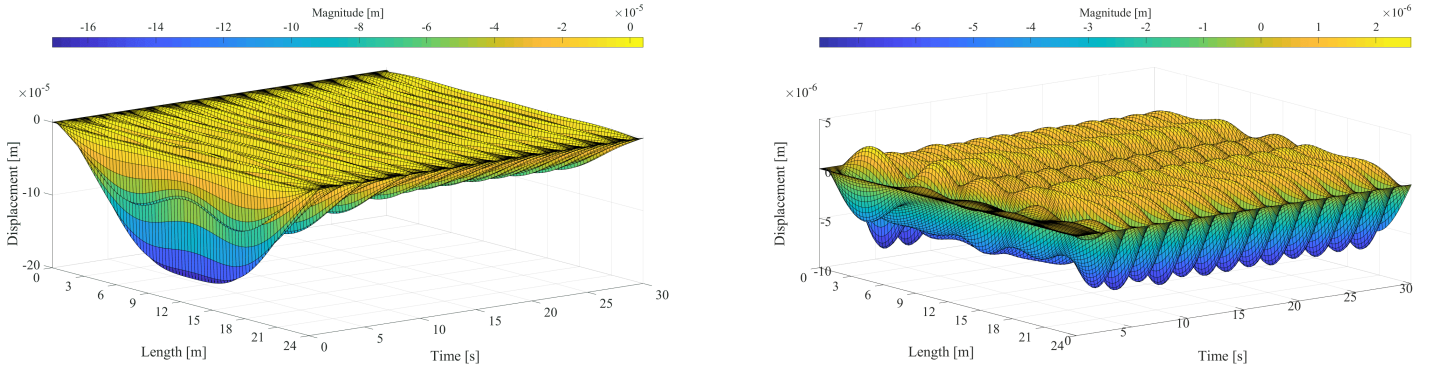

(a) Load case 1.1

(b) Load case 2.2

Figure C.2: Displacement in z-direction (Pinned, Fixed)

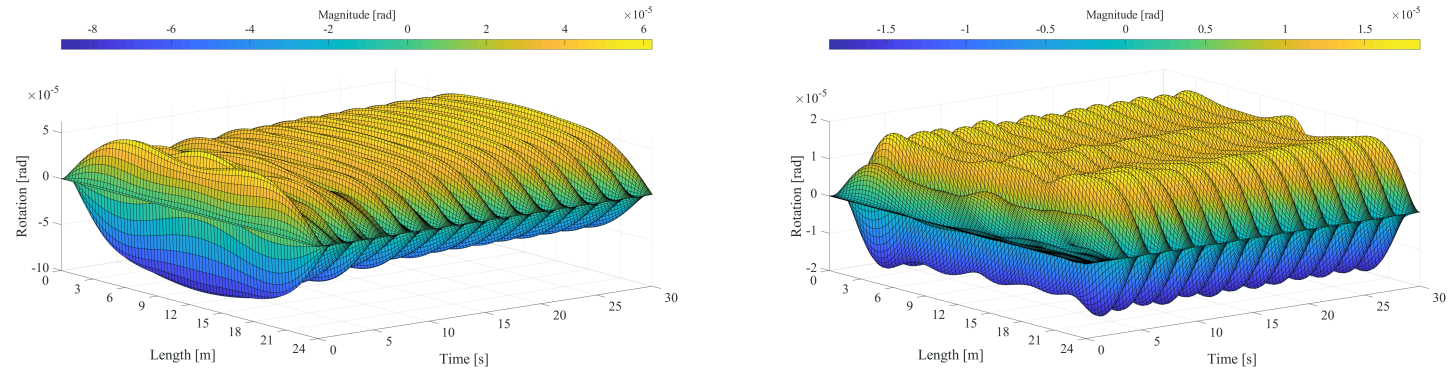

(a) Load case 1.1 (b) Load case 2.2

Figure C.3: Rotation in φ-direction (Pinned, Fixed)

C.2. Both end pinned beam & both end free torsion rod

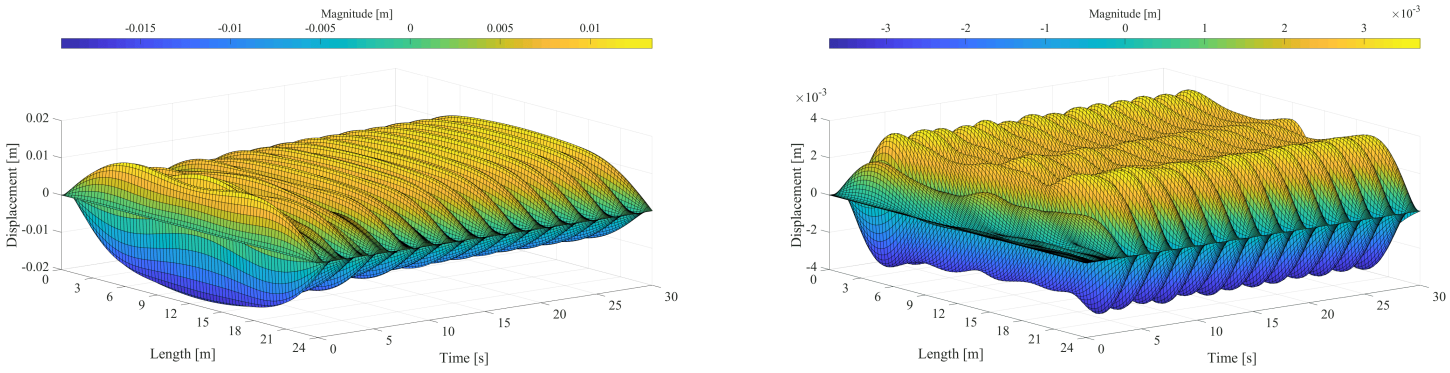

(a) Load case 1.1 (b) Load case 2.2

Figure C.4: Displacement in y-direction (Pinned, Free)

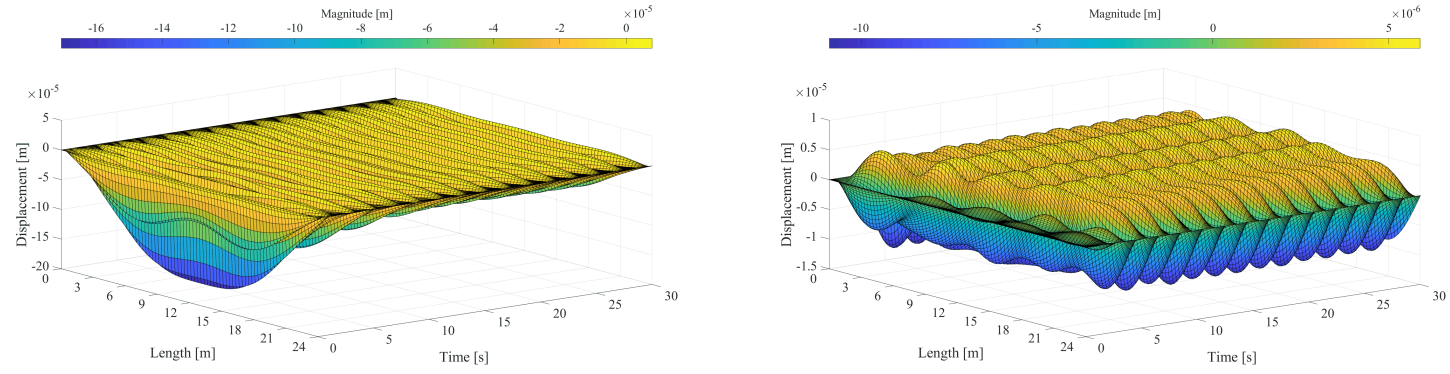

(a) Load case 1.1 (b) Load case 2.2

Figure C.5: Displacement in z-direction (Pinned, Free)

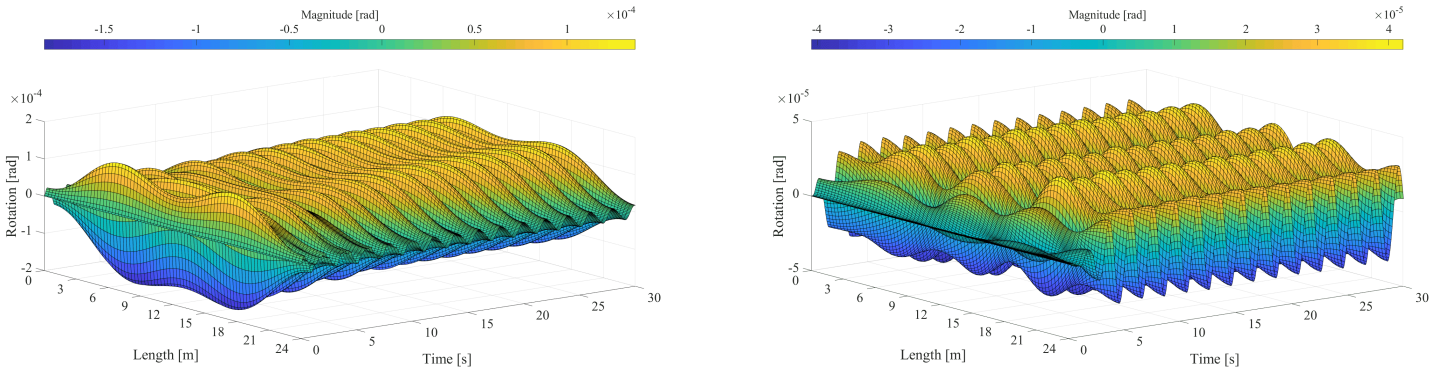

(a) Load case 1.1 (b) Load case 2.2

Figure C.6: Rotation in φ-direction (Pinned, Free)

C.3. Both end fixed beam & both end fixed torsion rod

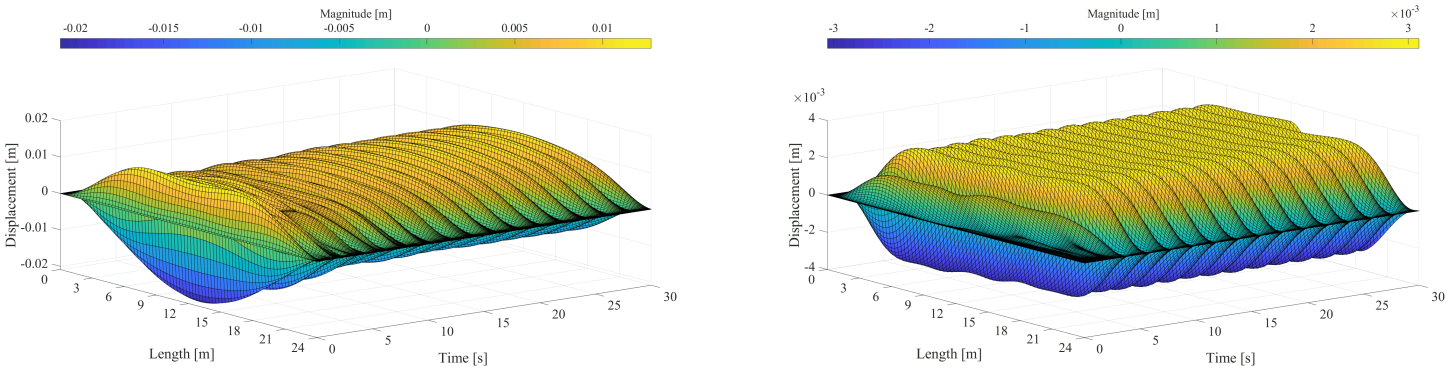

(a) Load case 1.1 (b) Load case 2.2

Figure C.7: Displacement in y-direction (Fixed, Fixed)

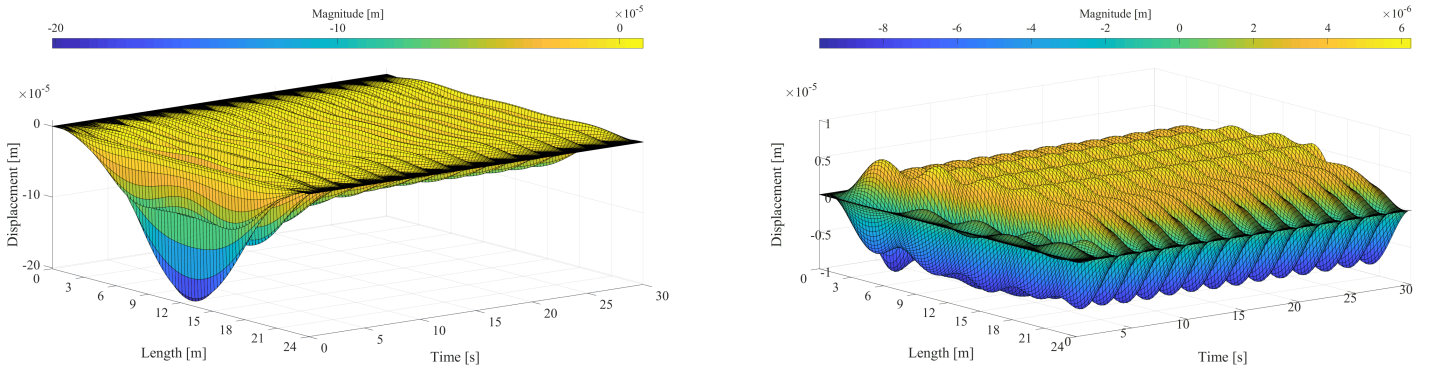

(a) Load case 1.1 (b) Load case 2.2

Figure C.8: Displacement in z-direction (Fixed, Fixed)

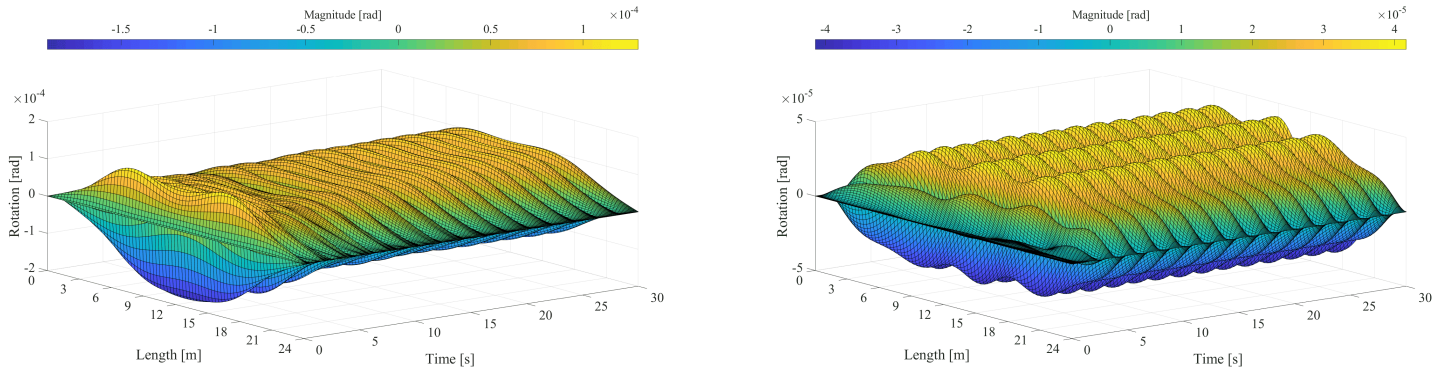

(a) Load case 1.1 (b) Load case 2.2

Figure C.9: Rotation in φ-direction (Fixed, Fixed)

C.4. Both end free beam & both end free torsion rod

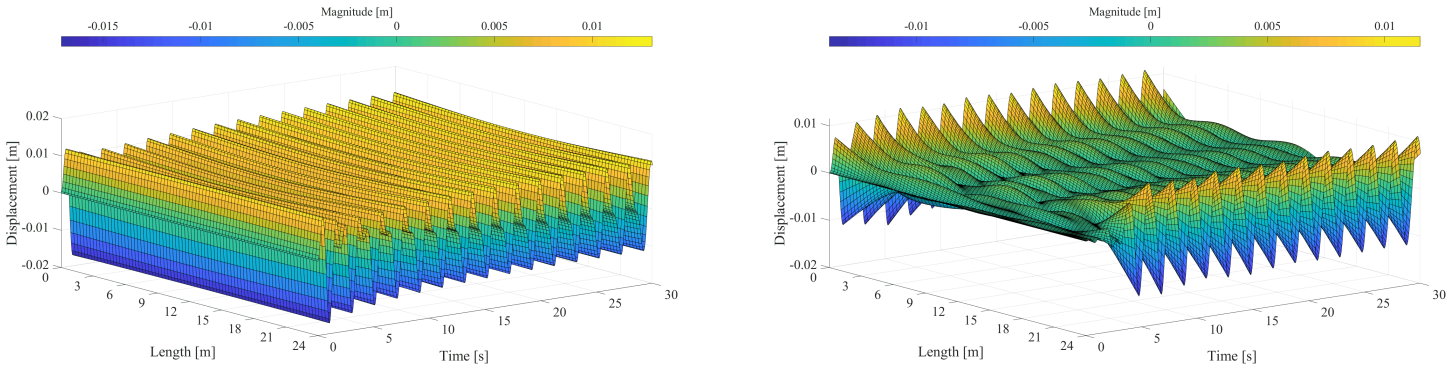

(a) Load case 1.1 (b) Load case 2.2

Figure C.10: Displacement in y-direction (Free, Free)

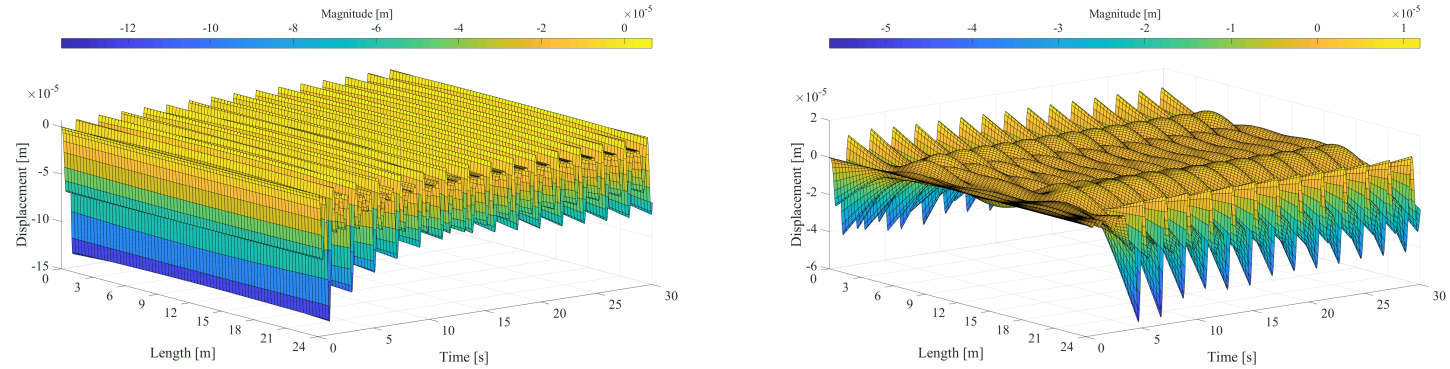

(a) Load case 1.1 (b) Load case 2.2

Figure C.11: Displacement in z-direction (Free, Free)

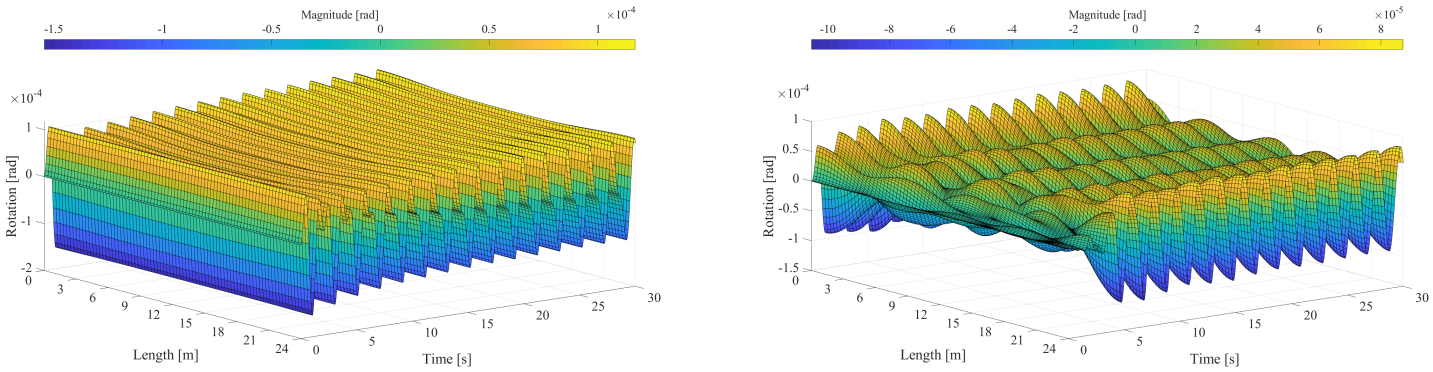

(a) Load case 1.1

(b) Load case 2.2

Figure C.12: Rotation in φ-direction (Free, Free)